Eulerian CFD Model of Direct Absorption Solar Collector with Nanofluid

by

Runa By Bårdsgård

Department of Physics and Technology
University of Bergen

A thesis in partial fulfulment of the requirements for the degree of *Master of Science* in the subject of Process Technology: Multiphase Systems

December 2019

Acknowledgements

First and foremost, I would like to offer my sincere gratitude to my supervisor Prof. Pawel Kosinski for his guidance and and helpful remarks through this whole master's degree, especially through the process of this master thesis. He has been very cooperative and provided useful material to complete this thesis. Furthermore, I would like to express my appreciation to co-supervisor Prof. Boris Balakin for his important contributions and expertise in the topic. A special thanks for sharing his knowledge in STAR-CCM+. These inputs have been crucial.

A sincere thanks to Dmitrii Kuzmenkov for sharing his research on volumetric absorption of nanofluids. Without his insights, the model would not have generated such great results.

I would like to express my gratitude to my family, friends and boyfriend for their endless love and support. Finally, a sincere thanks to my fellow students, especially to Lisbeth Espedal and Ragnhild Dybdal Øie for sharing my ups and downs these last five years.

Abstract

Solar energy is the most promising source of renewable energy. However, the solar energy harvesting process has relatively low efficiency, while the use of solar energy is challenging. Direct Absorption Solar Collectors (DASC) have been proved to be effective for a variety of applications, such as water heating. At the same time, a challenge with this technology is the collector efficiency limitation due to the absorption properties of typical working fluids. Nevertheless, mixing nanoparticles with a base fluid has shown dramatic effect on the fluids thermophysical properties. Moreover, nanoparticles also has the potential to improve radiative properties, thus increasing the efficiency of a direct absorption solar collector.

In this thesis, a numerical study of the inter-phase fluid-particle interactions and efficiency optimisation of a nanofluid direct absorption solar collector was performed using Computational Fluid Dynamics (CFD). A flat-plate DASC with incident light on the top surface was simulated using an Eulerian-Eulerian two-phase model. Theoretical calculations predicted the particle behaviour and magnitude of the applied forces. Validating the model against experimental results showed low discrepancies.

The first simulations were done with no momentum except for gravity working on the nanoparticles, and various volume fractions of nanoparticles ($\in [0, 1]$) were tested . Next, Brownian force and thermophoretic force were added to the model. After evaluating how these forces affected the flow, the drag force was updated to include the retardation factor, for both the thermophoretic and Brownian model. Later, the models were tested for an updated heat transfer coefficient. Investigation of the particle concentration showed that the optimum value for enhancing efficiency was obtained at 0.3 wt%. The highest efficiency (65%) was obtained for the model including Brownian motion and a corrected heat transfer coefficient. However, thermophoretic model with corrected heat transfer coefficient was in best correlation with the experimental results, so it was chosen as a base case for further study.

The base case simulation was developed, and has a qualitatively similar evolution of thermal efficiency, an optimal absorption of radiant heat and low discrepancy from experiments. This base case was used in a parametric analysis to optimise the performance of the collector. Collector height, nanofluid velocity and black surface absorbers were investigated. As the collector height was reduced, the outlet temperature increased. A maximum temperature of 49°C was observed for a 50 μm nanofluid film. The maximum efficiency (67%) was observed for collector height equal to 300 μm. Next, a high flow velocity of 3 cm/s gave a maximum efficiency of 88%. Nevertheless, this high velocity results in a high pressure loss through the collector.

Lastly, properties of the top and bottom surface were investigated. An efficiency of 67% was obtained for a water-filled collector with a black absorbing bottom. This efficiency is surprisingly high, and lead to a further investigation of these black absorbing bottom collectors. Using nanofluids, and adjusting the collector height resulted in better collector performance for lower collector heights.

Finally, design recommendations based on the performed theoretical and numerical analysis were presented.

Nomenclature

Abbreviations

CB   Carbon Black

CFD   Computational Fluid Dynamics

DASC   Direct Absorption Solar Collector

DEM   Discrete Element Method

DPM   Discrete Parcel Method

E-E   Eulerian-Eulerian

E-L   Eulerian-Lagrangian

NF   Nanofluid

NP   Nanoparticle

RANS   Reynolds-Averaged Navier Stokes

Greek Symbols

α	Stokes friction coefficient	
α_i	Volume fraction	[%]
β	Thermal expansion coefficient	[T^{-1}]
δ	Thickness of thermal boundary layer	[m]
$\delta_{i,j}$	Kroenecker delta	
ϵ	Emissivity	
η	Efficiency	[%]
λ	Molecular free path	[m]
λ	Wavelength	[m]
μ	Dynamic viscosity	[Pas]
ν	Kinematic viscosity	[m$^2/s$]
ρ	Density	[kg/m^3]

σ	Stefan-Boltzmann Constant (5.67×10^{-8})	[W/m$^2 K^4$]
σ_i	Extinction coefficient	[m^{-1}]
τ	Shear stress	[N/m^2]
ξ	Zero-mean and unit variance number	

Latin Letters

$\mathbf{e}_{i,j,k}$	Unit vector	
A	Area	[m^2]
C_c	Cunningham correction factor	
C_D	Drag coefficient	
C_p	Specific heat	[J/kgK]
C_s	Thermal slip coefficient = 1.17	
C_t	Momentum exchange coefficient = 1.14	
C_t	Thermal exchange coefficient = 2.18	
C_{ext}	Extinction cross-section	[m^2]
d_p	Particle diameter	[m]
e_i	Phase specific enthalpy	[J]
F	Force	[N]
f_{HR}	Retardation factor	
h	Heat transfer coefficient	[W/m$^2 K$]
k	Thermal conductivity	[W/mK]
k_B	Boltzmann constant (1.38×10^{-23})	[m^{2}kg/s^{2}K]
Kn	Knudsen number	
l	Optical path in the direction of thermal radiation	[m]
m	Complex refractive index	
m	Mass	[kg]
N	Number of particles	
n	Number density	[m^{-3}]
Nu	Nusselt number	
p	Static pressure field	[Pa]
Pr	Prandtl number	
Q	Volumetric flow	[m^3/s]

q	Heat generation	[W]
q_0	Solar radiation	[W/m^2]
R_i	Resistance	[Ω]
Re	Reynolds number	
S_0	Spectral intensity	
T	Temperature	[K]
t	Time	[s]
u	Fluid velocity	[m/s]
V	Volume	[m^3]
v	Particle velocity	[m/s]
$\mathbf{g}$	Gravitational constant	[m/s^2]
$\mathbf{v}$	Velocity vector	[m/s]
Gr	Grashofs number	

Subscripts

B	Brownian
c	Continuous phase
D	Drag
d	Dispersed phase
dep	Deposition
ext	Extinction
f	Base fluid
ij	Inter-phase
nf	Nanofluid
p	Nanoparticle
s	Surface
ss	Steady-state
T	Thermal
Th	Thermophoretic
V	Volumetric

Contents

Chapter 1

Introduction

Today's world energy balance is still strongly dependent on fossil fuels and coal. The global energy landscape has been through substantial changes over the past 25 years, with much larger changes in store for the future. Electricity and fossil fuel consumption increase every year, but the magnitude and direction of this growth is highly uncertain [53]. During 2015, the world consumed 146.000 TWh of primary energy, which is over 25 times more than in the 1800s [62]. Such a growing energy demand leads to a decrease in availability of energy sources. Figure 1.1 shows the increase in energy consumption from 1800 until 2017.
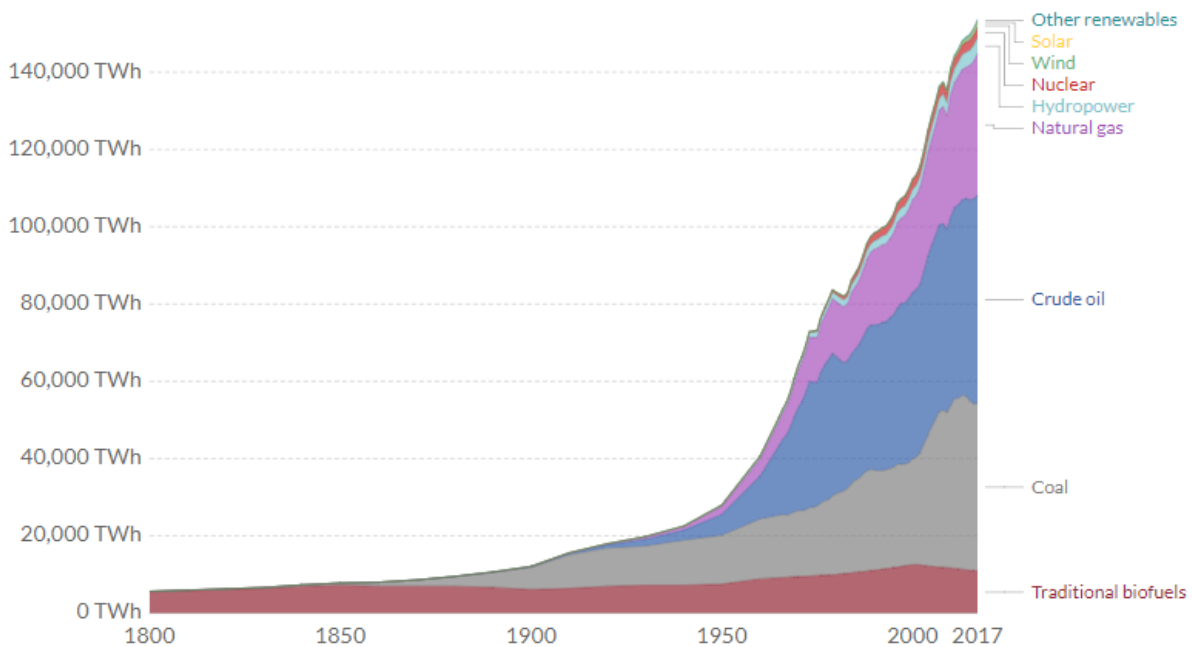

Figure 1.1: Global primary energy consumption [62].

To meet the energy demands, renewable energy sources are good alternatives. Solar energy has the greatest potential of all the sources of renewable energy, especially when other sources are depleted [64]. However, electricity generation from solar energy is not efficient enough to replace

fossil fuels and coal in northern countries, where the solar resources are insufficient. In this case, the solar thermal power becomes more interesting as over 65% of a household's electrical energy consumption is used to heat the premises [28]. Therefore, enhancing the heat transfer process in solar energy systems is essential to achieving better performance of these systems with compact designs. This enhancement is achieved by using working fluids with optimal thermophysical properties [19].

Solar collectors are types of heat exchangers where the heat exchange occurs between a distance source and a heat transfer fluid flowing in the collector. Solar radiation hits the plate of the collector, and the thermal energy is transferred to the fluid. Flat-plate collectors are the most common type of collectors, but also the most primitive [57]. These flat-plate collectors consist of a black flat-plate absorber and a heat transfer fluid (usually water). A simple illustration of the flat-plate collector is shown in Figure 1.2. The collectors harvest solar radiation and transform it into heat, which through conduction and convection, heats the fluid. This heat is usually used for household or industrial applications [10]. A considerable amount of research has been done on flat-plate collectors, and how to increase effectiveness.
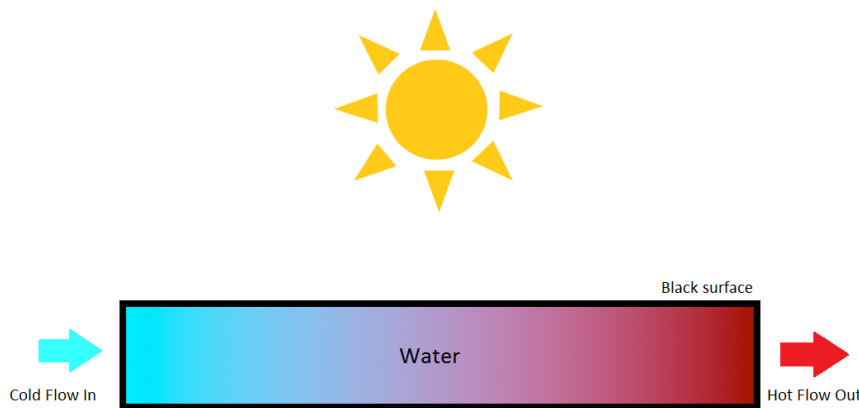
Figure 1.2: Schematic of a conventional flat-plate solar collector.

In 1975, Minardi and Chuang [50] introduced the concept of "black liquids" for the direct volumetric absorption of solar radiation. This led to the increased popularity of direct absorption solar collectors (DASCs). In direct absorption solar collectors, a heat transfer fluid volumetrically absorbs the incidental solar radiation, and this process has proven to be very effective [44]. These heat transfer fluids are suspensions of various nanosized particles in a base fluid. The interest in DASCs has been correlated to many reasons, such as a promising one-step solar-to-useful energy conversion, the potential of trapping thermal energy, scalability for low-flux and high-flux applications, development of nanofluid with excellent stability, and facility for integration with photovoltaic cells in multi-output collectors [31].

The main difference between a conventional flat-plate collector and a DASC is that the flat-plate collector utilises a surface absorber that transfers the heat to the working fluid, while the DASC uses volumetric absorption directly through the working fluid. This difference is illustrated in Figure 1.3. Efficiency enhancement of flat-plate collectors has been widely researched. Some studies have tried to use nanofluid directly in the flat-plate collector, enhancing efficiency by approximately 10% [10]. On the other hand, using a DASC with nanofluids enhance the efficiency

by 20% [51]. Other advantages of using DASCs instead of conventional flat-plate collectors include less thermal leaks, larger absorption area, increased thermal conductivity, and no clogging due to particle agglomeration. There is also a difference in resistances affecting the heat transfer; see Figure 1.3. Here, $R_0 < R_1 + R_2$, so that the DASC has higher thermal efficiency because of the lower thermal resistance.
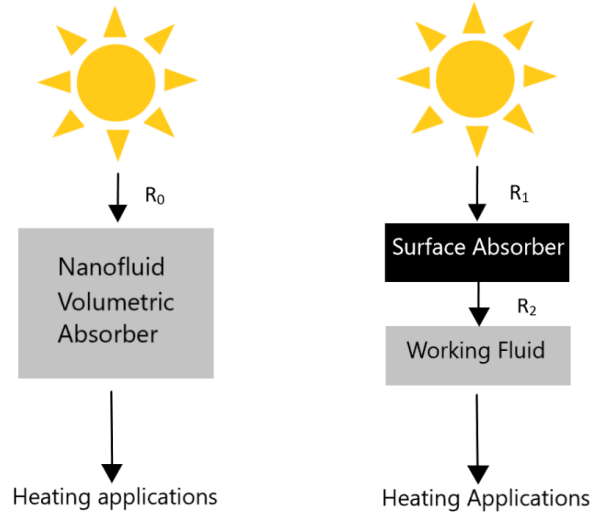
Figure 1.3: Comparison between NF volumetric absorber and conventional flat-plate collector. R_i represents thermal resistances corresponding to each step.

After reviewing different literature on nanofluid direct absorption solar collectors, it is clear that the research is promising. Due to the nanofluid abnormal enhancement of thermal conductivity, they showed optimal results for collector efficiency [2]. Nanofluids also have significant economic advantages, since a small amount of nanomaterial is necessary for making stable and effective suspensions [46]. There has been done a considerable amount of research, both numerical and experimental, on nanofluid efficiency. However, there is still a lot to be done before this technology can be used on a larger scale. One challenge with this technology is the thermal stability of the nanofluid because of particle agglomeration when the fluid is subjected to a temperature gradient. Another challenge is the lack of a reliable routine of the utilization of waste nanofluid.

Chapter 2

General Theory

This chapter provides an introduction to the physics, numerical methods, and thermodynamics used in this thesis. More detailed descriptions of the model are presented in chapter 4. This study utilises *nanofluid* as a heat transfer medium for a flat plate solar collector. In a nanofluid, a minimum of two phases coexists, thus it is defined as a multiphase system. Crowe et al. [16] define multiphase systems as a mixture of materials with different states of matter, for example, liquid, solid, or gas. This thesis focuses on nanofluids consisting of solid particles dispersed in a liquid "base fluid." The continuous phase is the phase that is connected, and properties vary continuously through the phase. The liquid is often referred to as the continuous phase. The dispersed phase is not materially connected, e.g. solid particles.

2.1   Computational Fluid Dynamics

Computational fluid dynamics (CFD) is the simulation of fluid flow systems, by using modeling, mathematical and physical problem formulation, and numerical methods. Several numerical methods can be applied, such as discretisation methods, solvers, process parameters, grid generation. These numerical simulations are an alternative to physical experiments and can be very valuable in situations where experiments can be difficult to execute in practice. The CFD software used in this thesis was the STAR-CCM+ version 13.02.013-R8 and 13.06.012 from Siemens. This software provides its user with multiple tools for modeling complex geometries, generate a mesh, and make use of models that account for different physical phenomena [71]. CFD is based on the three fundamental equations of fluid dynamics: continuity, momentum, and energy. These equations are based on three physical principles:

1. Mass is conserved

2. Newton's second law: force = mass x acceleration

3. Energy is conserved

These fundamental principles can be expressed as basic equations in their most general form (integrals or differential equations). CFD is the art of substituting the general form of these equations with discretised algebraic forms, which in turn are solved to attain numbers for the flow field values at discrete points in time/space [3]. The output from a CFD calculation is a

collection of numbers, versus a closed-form analytical solution. One advantage of CFD is that it can process repetitive manipulation of many thousands (even millions) of numbers, a task that would be impossible for the human mind alone. The term CFD refers to a broad spectrum of numerical methods used for solving the complex three-dimensional and time-dependent flow problems. This scientific field originally developed from new approaches to solving the Navier-Stokes equation numerically. Solving this equation remains one of the most challenging problems in numerical physics even today [60].

2.1.1   Governing Equations

As mentioned in the last section, CFD is based on the three fundamental principles: conservation of mass, Newton's second law, and conservation of energy. Before going further into the theory behind the governing equations, it is necessary to establish a notation that has an important physical meaning, the *substantial derivative*, $\frac{D}{Dt}$. The substantial derivative has a significant physical meaning and distinguishes from the more familiar $\frac{d}{dt}$. The physical definition of $\frac{D}{Dt}$ is the time rate of change following a moving fluid element. It is relevant when studying elements moving with the fluid flow, as illustrated in Figure 2.1. The substantial derivative applies to any flow-field variable, and can, for example, be defined as [3, 86]:

$$\frac{DT}{Dt} = \frac{\partial T}{\partial t} + \nabla \mathbf{v},$$

(2.1)

where $\frac{\partial T}{\partial t}$ is the local derivative, time rate of change at a fixed point, and $\nabla \mathbf{v}$ is the convective derivative, time rate of change due to the movement of the fluid from one location to another in the flow field where the flow properties are spatially different [3, 86].
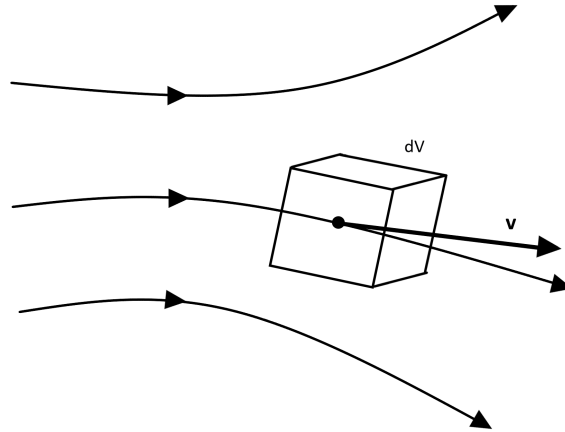
Figure 2.1: Illustration of infinitesimally small fluid element moving along a streamline with the velocity $\mathbf{v}$ equal to the local flow velocity at each point [3].

The continuity equation can be derived in several ways, obtaining a different form of the equation directly. Consider the flow model in Figure 2.1, an infinitesimally small element moving with the fluid flow. The fluid element has a fixed mass, but in general, its shape and volume change as it moves downstream. Since the mass is conserved, the rate of change of mass is zero as the element moves with the flow. Using the theory of the substantial derivative, this can be

expressed as $\frac{Dm}{Dt} = 0$. A final definition of the continuity equation is on nonconservation form (since the element is moving with the flow) [3, 67]:

$$\frac{D\rho}{Dt} + \nabla(\rho\mathbf{v}) = 0. \tag{2.2}$$

The momentum equation (Navier-Stokes equations) comes from applying Newton's second law ($\mathbf{F} = m\mathbf{a}$) to a model of flow. The same model used for the continuity equation illustrated in Figure 2.1, is used here. Newton's second law, when applied to a moving fluid element, says that the net force on the fluid element equals mass times the acceleration of the element. This force is expressed as a vector relation and divides into three scalar relations along x, y, and z-axis. In each direction there are only two sources of forces moving the fluid [3, 67]:

1. *Body forces*, which act directly on the volumetric mass of the fluid element. These forces "act at a distance," e.g. gravitational, electric, and magnetic forces.

2. *Surface forces*, which act directly on the surface of the fluid element. They are due to only two sources:

    (a) the pressure distribution acting on the surface

    (b) the shear and normal stress distributions acting on the surface

The momentum increment of the fluid flow per unit time equals the sum of the body force and the surface force acting on the fluid. A short and general definition of the momentum equation is [67]:

$$\frac{D(\rho\mathbf{v})}{Dt} = \rho\mathbf{F} + \nabla[\tau] + \rho\mathbf{g}, \tag{2.3}$$

where $\mathbf{F}$ represents the body forces acting on the element, and $[\tau]$ is the shear force tensor.

The energy equation is based on the energy conservation principle. The physical principle is based on the first law of thermodynamics, and when applied to the flow model of a fluid element moving with the flow, the first law states that: rate of change of energy inside fluid element equals net influx of heat into element plus rate of work done on element due to body and surface forces [3, 67]. In short terms, the rate of change of energy must equal the total energy transfer to or from surrounding elements. The energy equation on conservation form is:

$$\frac{\partial(\rho e)}{\partial t} + \nabla(\rho e\mathbf{v}) = \nabla(k\nabla T), \tag{2.4}$$

where e is the enthalpy of the element.

2.1.2 Physical Boundary and Initial Conditions

The equations described in the previous subsection govern the flow of a fluid. They are the same equations for any object. Flow fields can be different, even if the governing equations are equal. When solving these equations for one specific case, boundary conditions need to be introduced. The boundary conditions, and sometimes initial conditions, dictate the particular solutions to be obtained from the governing equations. In CFD, the boundary conditions have particular relevance: any numerical solution of the governing flow equations must be made to see if there is a strong and compelling numerical representation of the proper boundary conditions [3]. In this case, the boundary condition on a surface assumes zero relative velocity between a surface and a fluid. This boundary condition is called a no-slip condition. If the surface is stationary and the flow is moving past it, then flow at the surface (for viscous flow) is:

$$u = v = w = 0, \tag{2.5}$$

where u, v, and w are velocity components in x, y, and z-direction. Additionally, there is an analogous "no-slip" condition associated with the temperature at the surface. If the material temperature is denoted by T_{wall} (wall temperature), then the temperature of the fluid layer in immediate contact with the surface has equal temperature:

$$T = T_{wall}. \tag{2.6}$$

If the wall temperature is unknown, e.g. it is changing as a function of time to or from the surface, then the Fourier law of heat conduction provides the boundary condition at the surface. This general unsteady transfer introduces a temperature gradient and must be solved by treating the viscous flow and the thermal response of the wall material simultaneously. A boundary condition like this, as far as the flow is concerned, is a boundary condition on the temperature gradient at the wall, in contrast to stipulating the wall temperature itself as the boundary condition. Thus, the temperature gradient is defined as:

$$\left(\frac{\partial T}{\partial n} \right)_{wall} = -\frac{q_{wall}}{k_{wall}}. \tag{2.7}$$

Here n denotes the direction normal to the wall, q_{wall} the heat transfer to the wall, and k_{wall} is the thermal conductivity of the wall. When there is no heat transfer at the surface (an adiabatic wall) the heat transfer to the wall $q_{wall} = 0$, and this can be inserted to the equation above.

The conditions discussed here are physical boundaries set by nature. These boundary conditions are applied in each time step. Also, there is a wide range of boundary condition types that permits flow to enter and exit the model domain. Inlet and outlet boundaries control parameters that enter and exit the computational domain. The most common here is velocity inlet and pressure outlet. Boundary conditions can also be useful for saving computational time. Symmetry boundaries allow one to take benefit of physical flow symmetry, to reduce the size of the computation domain, and periodic boundaries allow for the account of periodically repeating nature of the flow in the simulation and thus save memory and time.

Initial conditions are values that define flow field variables at the starting point ($t = 0$), and the most common physical parameters to account for here are velocity, pressure, and temperature. These values should be set as close as possible to what is expected for a steady-state solution. For steady-state computations, the initial conditions does not usually influence the converged solution, but setting initial conditions to non-physical values or values far away from the final solution can affect the path to final convergence, and the effort required to reach convergence.

2.1.3   Discretisation and Solution

All the governing equations above are described as partial differential equations. Analytical solutions of partial differential equations involve closed-form expressions that give values for the dependent variables continuously through the domain. In contrast, numerical solutions give answers at discrete points in the domain, called grid points [3]. The majority of CFD applications involve numerical solutions on a grid that contains uniform spacing in each direction, which simplifies the programming of the solution, saves storage space, and increases accuracy. Note, recent CFD has also focused on unstructured grids, where gridpoints placements are in very unstructured fashion [3]. Thus, there is a distinction between structured and unstructured grids.

Depending on the mathematical model, STAR-CCM+ discretises the continuous equations from either the finite volume or the finite element method [3]. For solving the incompressible Navier-Stokes equations, a staggered grid, like the one shown in Figure 2.2 is used. The process of discretising a model follows the procedure:

1. Divide the continuous domain into a finite number of subdomains (collection of elements or cells altogether, making up the mesh).

2. Store the unknowns at specific locations of the mesh, like vertices, cell centroids, face centroids, or edges.

3. The integral or differential equations are employed for discretisation in space and time.

After this discretisation procedure, the result is a coupled system of algebraic equations that need to be solved for each time step. Also, there are different ways to generate a mesh, resulting in varying shapes and sizes of the subdomains. Mesh types chosen for a flow can determine the accuracy of the numerical solution.
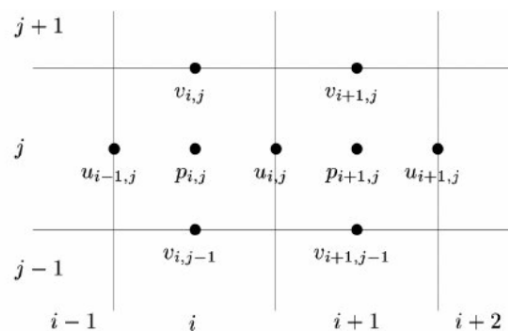

Figure 2.2: Staggered grid discretisation [66].

STAR-CCM+ utilises the finite difference method. The purpose of the finite difference method is to replace a partial derivative with an algebraic difference quotient. The method is commonly based on the Taylor series expansion. The resulting linear equations are solved with an algebraic multigrid solver. For solving the incompressible Navier-Stokes equations, a staggered grid is used [3].

Also, there are two techniques for solving the resulting algebraic equations:

1. *The explicit approaches*, where each equation contains only one unknown and can be solved in a straight forward manner.

2. *The implicit approaches*, where each equation has more than one unknown and the equations need to be solved simultaneously.

The implicit approach is used in this thesis. The advantage of using this approach is that stability can be maintained over a much more significant time step, than the explicit approach, resulting in a shorter computational time.

2.1.4   Mesh

The discrete points through the domain, described in the last subsection, were defined as a grid or mesh. When executing a numerical analysis, the solution domain is divided into multiple sub-domains, called cells. A mesh can be viewed as several smaller cells that overlay the entire geometry domain, making a discretised representation of the geometric domain [82]. When obtaining reliable solutions, mesh generation is crucial. A quality mesh improves numerical stability and increases the validity of the solution.

The fundamental equations that represent the flow are applied to each cell. These equations calculate the changes in each cell within the entire geometry. Afterward, they are solved to obtain the corresponding discrete values of the flow-field variables (velocity, pressure, temperature) [3]. The only possibility for solving the mathematical model is to assume linearity. Consequently, all the variables the expressions are to be solved for, are linear within the cells. Some areas are highly critical to the simulation results and need a finer mesh to assure high accuracy. Failures encountered in simulations are often related to errors in mesh structures; e.g. too coarse mesh that does not cover all the effects in a single element, but covers multiple effects [82]. Most errors can be removed by applying a finer mesh.

Mesh types can be either structured or unstructured. The unstructured mesh is used with complex geometries that do not fit in the Cartesian coordinate system. An unstructured mesh could be constructed to fill the interior curvilinear geometries, and the lack of structure of the cells makes it highly suitable for the complex 3D structures. In STAR-CCM+, several meshing models can be chosen to generate a grid suitable for various geometries and applications [82].

2.2   Properties of Dispersed Phase Flows

Dispersed phase flows are flows where one phase, the dispersed phase, is not materially connected. Example of dispersed phase flows are: gas-droplet, gas-particle, and liquid-particle flows, where the particles constitute the dispersed phase. Bubbles in a bubbly flow also represent the dispersed phase [16].

To define properties of the dispersed phase flows, consider the elements of the dispersed phase that are enclosed by the volume. This volume contains a sufficient number of dispersed phase elements to ensure insignificant variations, and provide a continuous change in properties from point to point. This volume can be defined as ΔV_{mo}, and the *number density* can be found by using ΔN as the number of particles:

$$n \simeq \frac{\Delta N}{\Delta V} = \lim_{\Delta V \to \Delta V_{mo}} \frac{\Delta N}{\Delta V}. \tag{2.8}$$

The *volume fraction* of the dispersed phase can be defined as:

$$\alpha_d = \lim_{\Delta V \to \Delta V_{mo}} \frac{\Delta V_d}{\Delta V}, \tag{2.9}$$

where V_d is the volume occupied by the dispersed phase. An equivalent expression describes the continuous phase. By definition, the sum of the volume fractions must be unity ($\alpha_d + \alpha_c = 1$).

Particle flow can be sorted into two main categories; *dilute* and *dense* flows. A dilute dispersed phase flow is flow where the motion of the particles is controlled by the fluid forces (e.g. drag and lift). A dense flow is a flow where particle motion is controlled by collisions or continuous contact between particles [16].

2.3   Numerical Modeling of Multiphase Flows

An ideal numerical model for the particle phase resolves the dynamics and thermal properties of each of the particles in the system. However, many millions of particles in a typical industrial application makes such an approach currently almost impossible [16]. Instead of tracking each particle alone, the particle cloud approach is used, where bulk properties are interpreted in terms of mixing, chemical reactions, and other processes. There are two main approaches when modeling multiphase systems, Eulerian-Lagrangian and Eulerian - Eulerian. The main difference between the two is how they treat the dispersed phase. The continuous phase in both cases is described by the Eulerian approach, which means that the model solves the Navies-Stokes equations for the viscous fluid flow, and the governing equations are modified to take the presence of the dispersed phase into account. Figure 2.3 illustrates the two main approaches. The open circles in the figure represents discrete elements in the cloud.
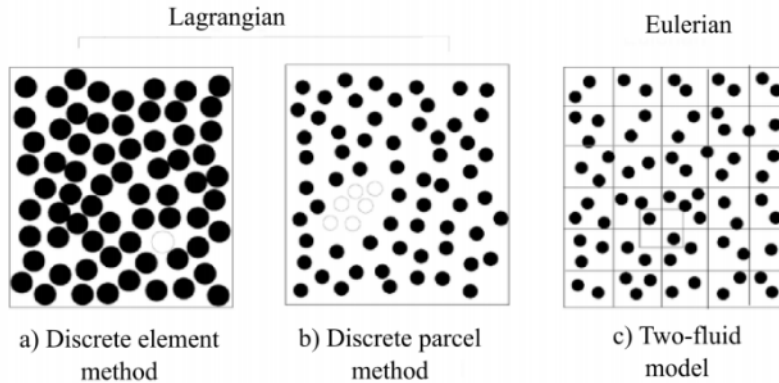
Figure 2.3: different approaches for modeling particle and droplet clouds [16].

2.3.1   Eulerian - Lagrangian Approach

The three methods from Figure 2.3 are categorised into Lagrangian tracking or Eulerian modeling approaches. With the discrete element and the discrete parcel methods (Lagrangian), individual particles or parcels are tracked through the field, and the local properties of the cloud are found from the properties of the particle or parcel as they pass the point in the field [16]. The dense or dilute flow characteristics described in section 2.2 are fundamental for determining the approach to be used for modeling the dispersed phase.

The Discrete Element Method (DEM) has found numerous applications in granular flows and fluidized beds. It is particularly applicable for contact-dominated flows [16]. With this model, the particle flow is resolved down to the particle level. DEM has an advantage that the numerical model provides a detailed description of the cloud. The problem is that a considerable number of discrete elements are needed to model efficient systems. [16]

The Discrete Parcel Method (DPM) involves identifying a group (parcel) of particles and then tracking the parcel through the flow field. All the particles that are in the parcel are assumed to have the same properties (e.g. size, velocity), so the group is represented by one computational particle.

2.3.2   Eulerian - Eulerian Approach

The two-fluid model from Figure 2.3 is an Eulerian approach, where a set of algebraic conservation equations are solved simultaneously for each node in the field. The Eulerian approach works for dense flows, where particle collisions allow information to travel in all directions, and the particle clouds can be modelled as a continuous fluid. For a dispersed/continuous flow, the continuous phase is always modelled with an Eulerian approach. Usually, equations are developed for the conservation of mass, momentum, and energy at a point in the cloud. The Eulerian approach also discretised the equation into algebraic equations at the computational nodes in the field and solved using the same procedures as used for the conveying fluid.

2.3.3 Turbulence

Turbulent flows contain eddying motions of all sizes, and a significant part of the mechanical energy goes into the formation of these eddies. Transition to turbulence can occur over a range of Reynolds numbers, depending on many factors, such as surface roughness, heat transfer, vibration, noise, and other disturbances [80]. The Reynolds number has traditionally been used to characterise the transition from deterministic flow to chaotic flow [16]. The transition zone from laminar to turbulent flow occurs at $Re = 2300$. It is possible to simulate turbulent flow directly from solving the Navier Stokes equations, but it requires considerable computer resources. Therefore, STAR-CCM+ solves these equations for averaged quantities by the Reynold-Averaged Navier Stokes (RANS) equations and approximates the impacts of small fluctuating structures [71]. This model aims to describe the flow statistically. Time averaging is employed in Reynolds-Averaged modeling to reduce the range of scales present in turbulent flows. The averaging time is much larger than the largest timescale of the turbulent fluctuations, and as a result, one ends up with conservation equations that describe the evolution of the mean flow quantities only [63]. Commonly used for RANS turbulence is the $K - \epsilon$ model. It is a two-equation model that includes two other transport equations to represent the turbulent properties of the flow. These alterations allow a two-equation model to account for history effects like convection and diffusion of turbulent energy [83].

2.4 Heat Transfer

When there is contact between two objects of various temperatures, heat flows from the object with a higher temperature to the object with lower temperature, following the second law of thermodynamics [15]. The net flow of heat is always in the direction of temperature decrease. There are three mechanisms by which heat may flow: conduction, convection, and radiation [49].

2.4.1 Conduction

The transfer of energy from the more energetic particles of a substance to the adjacent, less energetic ones as a result of interactions between the particles is known as conduction. Conduction can occur in solids, liquids, and gases [15]. Fourier's law states that the heat flux is proportional to the negative temperature gradient. For one-dimensional heat flow, it is defined as [49]:

$$\frac{dq}{dA} = -k\frac{dT}{dx},\qquad(2.10)$$

where q is the rate of heat flow in the direction normal to the surface, A is the surface area, T is the temperature, x is the distance normal to the surface, and k is a proportionality constant. The proportionality constant k is a physical property of the fluid called the *thermal conductivity*, a measure of the ability a material to conduct heat [15].

2.4.2   Convection

Convection refers to the energy transfer between a solid surface and a liquid or gas in motion and involves the combined effects of conduction and fluid motion [15]. The main types are forced and natural convection. Forced convection is used for optimising heat transfer processes, for example, in a heat exchanger. The convective flux is usually proportional to the difference between the surface temperature and the fluid temperature, and expressed by Newton's law of cooling [49]:

$$\frac{q}{A} = h(T_s - T_f),\tag{2.11}$$

where T_s is the surface temperature, T_f is the bulk temperature of the fluid, and h is the *heat transfer coefficient*. Unlike thermal conductivity, the heat transfer coefficient is not a property of the fluid. It is an experimentally determined parameter, and its value depends on all the variables that influence the convection, e.g. surface geometry, properties of the fluid, and bulk fluid velocity [15]. Due to the movement of the fluid, a thermal boundary layer occurs. If $T_S > T_f$, the fluid temperature behaves asymptotically within the boundary layer. The boundary layer reaches to the point where the temperature is within 1% of the free-stream temperature (T_f) [77]. Calculating the thickness of the boundary layer, δ, includes using dimensionless groups, such as the Prandtl number and Grashof number. A thermal boundary layer is illustrated in Figure 2.4.
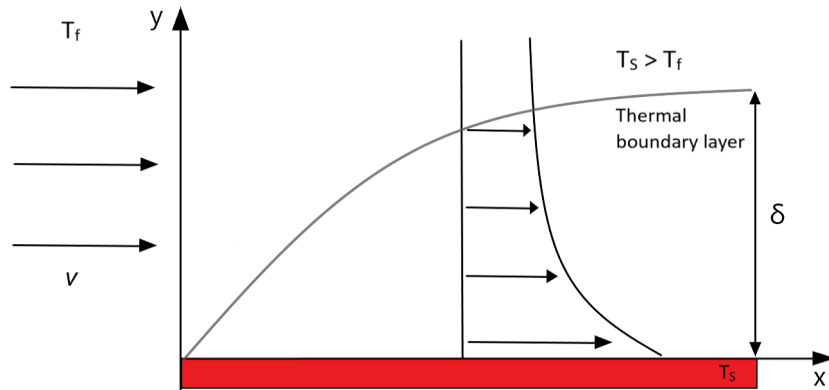

Figure 2.4: Thermal boundary layer from flow past a flat surface.

The Prandtl number is defined as:

$$Pr = \frac{C_p \mu_f}{k_f},\tag{2.12}$$

where C_p is the specific heat of the nanoparticles.

This case is described as flow past a flat plate, where the thermal boundary layer is defined by Lienhard [43] and Graebel [24] as:

$$\delta = 3.936x \left(\frac{0.952 + Pr}{Pr^2} \right)^{\frac{1}{4}} Gr_x^{-\frac{1}{4}}, \tag{2.13}$$

where x is the position on the plate, Pr is the Prandtl number, and Gr_x is the position dependant Grashof number. The Grashof number is calculated from [24]:

$$Gr_x = \frac{g\beta(T_s - T_f)x^3}{\nu^2}, \tag{2.14}$$

where g is the gravitational acceleration, β is the coefficient of thermal expansion, T_s and T_f is the temperature of the surface and fluid, x is the position, and ν is the kinematic viscosity. The coefficient of thermal expansion is defined by McCabe [49] as:

$$\beta = \frac{\rho_1 - \rho_2}{\bar{\rho}_{avg}(T_2 - T_1)}, \tag{2.15}$$

where ρ_{avg} is the average value taken from ρ_1 and ρ_2. ρ_1 and ρ_2 are densities at temperatures T_1 and T_2.

2.4.3   Radiation

Radiation is the energy emitted by matter in the form of electromagnetic waves, or photons, as a result of the changes in the electronic configurations of the atoms or molecules [15]. Unlike conduction and convection, radiation does not require the presence of an intervening medium and can travel through a vacuum or any transparent solid or fluid. Radiation is not heat but is transformed to heat upon absorption. The fraction of radiation falling on a body depends on the body's reflectivity, absorbtivity, and transmissivity. The sum of these fractions must be unity, $absorbtivity + reflectivity + transmissivity = 1$ [49]. Stefan-Boltzmann's law [15] defines the thermal radiation emitted by a body:

$$\frac{q_{emit}}{A} = \epsilon \sigma T_s^4, \tag{2.16}$$

where T_s is the temperature of the surface A, ϵ is the emissivity of the surface, and σ is the Stefan-Boltzmann constant. Emissivity represents how close a surface approximates a blackbody, and have value $0 \leq \epsilon \leq 1$. For maximum solar energy utilisation, a body must have excellent absorptivity properties, which means it does not transmit or reflect the radiation. A body that absorbs all incident radiation is called a *blackbody* [15, 49].

When solving problems of radiation heat transfer in light scattering medium, Mie theory is used. Mie theory is a theory of absorption and scattering of plane electromagnetic waves by uniform isotropic particles of the simplest form (e.g. spheres) which are in a uniform, isotropic medium [72]. The basic aim of this theory is to calculate efficiency coefficients for absorption, scattering and extinction.

2.5   Nanofluids

Nanofluids are defined as colloidal suspensions of fine nanomaterials in size range of 1 - 100 nm
in carrier fluids [8, 58, 64]. Nanofluids can be used for a wide variety of industries, ranging from
transportation to energy production to biotechnology [64]. Through the last decade, research
on nanofluids has been popular due to their enhanced thermal properties and heat transfer
applications. For solar heating purposes, some NPs have been studied more than others due to
their high photothermal response. Many of the conventional heat transfer fluids have very low
thermal conductivity, which is a serious limitation when the main goal is to improve performance.
Because NPs have significantly higher thermal conductivity than these fluids, it was proven that
fluids containing suspended solid particles have an increased thermal conductivity compared
to the bulk fluids [19]. The most frequently studied carbon-based NPs for heat transfer fluids
are CB, graphene, graphitised carbon, and carbon nanotubes. Frequently researched metallic
NPs are e.g. copper (Cu), gold (Au), aluminium (Al) and silver (Ag). Frequently researched
non-metallic NPs include aluminium oxide (Al_2O_3), IO(Fe_3O_4) and titanium oxide (TiO_2) [8,
58]. Multiple authors concluded that it is beneficial to use nanofluids in high-temperature
applications [22, 42, 54, 58].

The thermal conductivity of nanofluids is the most attractive characteristic of the applications
related to this thesis. Considerable research has been done on this topic. Improvements in
thermal conductivity up to 150% compared to the base fluid has been discovered [64]. Thermal
conductivity increases with particle volume fraction but decreases with time. Also, the increase
in thermal conductivity is related to the NP material [54, 79], pH level, and addition of sur-
factants to keep the dispersion stable [42]. Carbon black nanofluids have excellent solar energy
absorption properties. These properties relate to the fact that CB nanoparticles are one of the
few substances that maintain similar absorption characteristics as a black body. These results
come from Han et al. [30], that studied the whole solar spectrum for CB nanofluids. This study
investigates graphite/aqueous nanofluids. Graphite consists of pure carbon, in its most stable
form under standard temperature and pressure.

Previous research has shown promising behaviour and properties of nanofluids. However, there
are challenges related to this research, as well. The development of nanofluid technology is
hindered by [8, 64]:

1. lack of agreement in results obtained by different studies

2. poor characterisation of suspensions

3. lack of theoretical understanding of the mechanisms causing changes in NF properties

4. long term stability of nanoparticle dispersion due to Van der Waals interactions

5. performance in turbulent flow and fully developed region

Issues such as thermal conductivity, Brownian motion of particles, particle mitigation, and
thermophysical properties changing with temperature must be carefully considered to obtain
accurate results within the research.

Chapter 3

Literature Review

Studies of nanofluids has become a popular research topic in the last decade. This section provides an overview of some relevant studies done on the efficiency of nanofluids, the effects of Brownian- and thermophoretic force, and direct absorption solar collectors.

Solar flat-plate collectors have been studied and used for many years. Recently, it has been an increased interest in improving the efficiency of these solar collectors. Pandey and Chaurasiya [57] wrote a review of advances in these studies. They gave a brief insight into different techniques used to enhance thermal efficiency. When nanofluid was considered as a heat transfer fluid, a 10% increase in thermal efficiency was observed. Additionally, advantages like cost-effectiveness and sustainability were mentioned. Mirzaei et al. [51] compared flat-plate collectors and direct absorption solar collectors experimentally and presented a collector efficiency increase of 23.6% for nanoparticle volume fractions of 0.1%. Comparison is shown in Figure 3.1, where the nanofluid used was 20 nm Al_2O_3 particles dispersed in water.
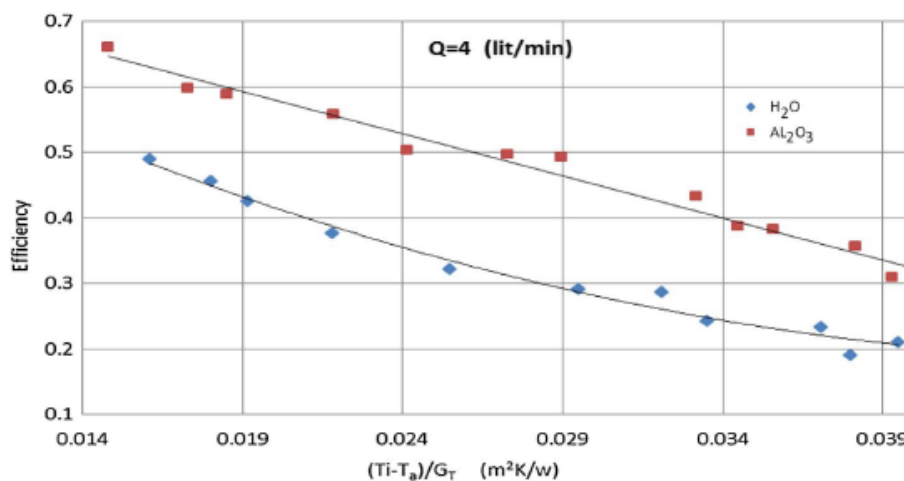

Figure 3.1: The efficiency of the flat-plate solar collector with Al_2O_3 nanofluids and water [51].

One of the first detailed descriptions of the effective heat generation by nanoparticles was obtained by Neumann et al. [52]. They studied the absorption of nanoparticles dispersed in water and demonstrated an efficient steam generation using solar illumination. The solar illumina-

tion was approximately 1 kW/m^2 [22, 54]. Silica and gold nanoparticles were used to develop nanoshell particles. The experiments were performed to show boiling by illumination and generated steam temperatures of up to 150 °C. The steam generated could be sufficient enough to drive a turbine [52] and generate electricity. Their thermodynamic analysis showed that 80% of the absorbed sunlight was converted into water vapour, and only 20% of the absorbed light energy was converted into heating of the surrounding liquid. As 80% efficiency is considerably high, results from numerous studies were compared to confirm the high efficiency of this process [35, 52]. Ni et al. [54] studied the effect of various nanofluids on the receiver efficiency by performing solar vapour generation experiments on a custom-built lab-scale receiver. In their study, for low concentration sunlight (10 suns), the efficiency was also very high (69%). There were better performances in transient situations for graphitised CB and graphene nanofluids than for CB nanofluids. Finally, the study by Ghasemi et al. [22] shows a solar thermal efficiency of up to 85% at low concentration sunlight.

Wang et al. [79] systematically studied thermal conductivity and rheological properties of colloidal graphite/oil nanofluids. The enhancement of thermal conductivity in nanofluids depend strongly on the volume fraction (%) [37] of graphite and increase nonlinearly with increasing particle loading but have a weak relationship with temperature [56, 79]. The rheological measurements were conducted to demonstrate the microstructure and fluid behaviours of the colloidal graphite/oil NFs. Comparing the NFs with the Newtonian fluid behaviours of base liquids and other nanofluids, the apparent shear thinning, significant viscosity increase and slight viscoelasticity enhancement for a typical NF sample containing 1.35% graphite with dispersant can be created, offering the evidence for the formation of percolating aggregate structures [79]. Even though there have been numerous experimental and theoretical studies, it is still unclear whether the thermal conductivity enhancement in nanofluids is anomalous or within predictions of theory [58]. Philip and Shima [58] provided an overview of advances in the NF field, with a particular focus on the material properties that affect the thermal properties of NFs and approaches to achieve extremely high thermal conductivities. Bellos et al. [8] mention recent advances in nanofluid technology. New types of nanofluids have been tested to find more efficient nanoparticles for increasing the performance of solar thermal systems. The ultimate performance was achieved by using NiO nanoparticles dispersed in a typical heat transfer fluid. Research on magnetic fields and combining nanofluids with other thermal enhancement methods is also promising [8].

In addition to experiments, there have been numerical studies of nanofluids. Kamyar et al. [37] performed a study of conventional numerical methods for NFs. Their computational simulations are in acceptance with the results from experiments. In most early numerical studies, single-phase modeling has been preferred due to the ultra-small size of the particles [37]. Here, NP and base fluid are assumed to be in thermal equilibrium with the fluid phase, and they have a zero relative velocity between the phases [36, 37]. Ding and Wen [17] proved that this is not always true for nanofluids, by investigating particle mitigation in a nanofluid for pipe flow. Fard et al. [21] compared the single-phase model against the two-phase model and showed that the two-phase model had increased accuracy. There have also been some newer numerical studies considering the NF as two-phase flow. Comparing the results with the homogenous models from single-phase modeling, more accurate results were acquired for the two-phase model [36, 37, 44, 54]. Two-phase modeling results show higher heat transfer enhancement, compared to the homogenous single-phase model [36].

Although there have not been many computational studies of nanofluid flow in DASCs, a number of papers consider flow and heat transfer of nanofluids in thermal systems of other type. Yin et al. [84] investigated how aerosol nanoparticles were affected by forces. The main forces acting are drag-, Brownian- and thermophoretic forces. A discrete phase model was used to investigate the particle motion. The simulation results included the efficiency and deposition patterns at various temperature gradients. Haddad et al. [27] observed that thermophoresis and Brownian motion increased heat transfer in the nanofluid. The enhancements were higher at lower volume fractions. Another study, by Burelbach et al. [14], investigated the behaviour of colloids under the impact of a thermophoretic force. They discovered that the thermophoretic force varies linearly with the temperature gradient, supporting the linear-response assumption of the theory of non-equilibrium thermodynamics. They also discovered that surface functionality plays an intricate role in thermophoresis that cannot be explained by considerations of surface potential only. Abarham et al. [1] performed a CFD analysis of particle transport in axisymmetric tube flows under the influence of thermophoretic force. They developed two computational frameworks (1D and axisymmetric model) to study transport an deposition of non-isothermal tube flow, with a good description of the thermophoretic force. Their study showed that the axisymmetric model was in better agreement with experimental results.

Taking Brownian motion into consideration, models described by Balakin et al. [5] are relevant for the nanofluid investigation. They have also correlated it for use with direct absorption solar collectors. Balakin et al. based their research on the new model for Brownian motion, in nanofluid flow, made by Dong et al. [5, 18]. Dong et al. [18] presented a new solution to the Langevin equation. The model was developed by simulating (E-L) Brownian force based on experimental measurement results of Brownian motion that follows a white Gaussian noise process. Their simulation results show that the distribution of nanoparticles inside the channel is unsteady and nonuniform. Yin et al. [84] discovered that the Brownian force takes the particles in the opposite direction of the particle concentration gradient, in an attempt to make the particle more homogeneous. The diffusivity was investigated to determine the primary mechanism of particle mitigation. The resulting conclusion was that the Brownian force has a more significant impact on nanoparticle deposition with smaller particles and lower air temperatures. In comparison, the thermophoretic force is higher with a high temperature gradient [1, 14, 84].

Liu et al. [44] systematically investigated graphene/[HMIM]BF$_4$ based solar thermal collectors. Their research provided an important angle on how to efficiently utilise graphene/ionic liquid as DASC under concentrated solar incident radiation. It was discovered that the radiative properties of graphene/ [HMIM]BF$_4$ were tuned by adjusting the graphene concentration. One example is that nanoparticles can be modified to get increased dispersion stability in the NF mixture. A numerical model was used to predict temperature profiles based on direct absorption by graphene. Convective heat transfer loss and thermal emission at high-temperature profiles of 0.0005 wt.% and 0.001 wt.% of graphene in [HMIM]BF$_4$ for corresponding fluid height 7.5cm and 3.8cm, the experimental results show in good agreement with numerical results. The model shows that the receiver efficiency increases with increasing solar concentration and receiver height, but conversely with the graphene concentration under concentrated incident solar intensity. Additionally, Liu et al. investigates agglomeration in the unmodified graphene for high temperatures, and shows how important dispersion stability is when using NF with DASC.

A comprehensive numerical analysis of a microsized DASC with nanofluid was performed by Sharaf et al. [69] who modelled the collector using an E-L approach. They discovered that

the Reynolds number has a strong effect on the local NP distribution in the flow of a nanofluid. They also studied how NF optical properties in the visible radiation specter are highly dependent on the local nanoparticle concentration, which is in contrast to the infrared spectrum, where variations in the NP distribution have little effect on optical properties. The results obtained are important when designing this type of solar collector because they demonstrate how the performance of the collector depends on the spatial distribution of NPs. The simulation results were in excellent agreement with the experiment. However, the particles were modelled using the Lagrangian approach which is computationally expensive and, therefore, becomes hardly scaled to a DASC with dimensions of industrial relevance. Otanicar et al. [55] demonstrated four advantages of using DASC over conventional collectors by studying how to improve the efficiency of nanofluid technology. These advantages include limiting heat losses from peak temperature, maximising spectral absorption of solar energy, enhancements of thermal conductivity, and enhancements of surface areas due to tiny particle sizes. They also used a microsized plate collector, and have good results for thermal efficiency, which is adapted later in this thesis. The results of their study are shown in Figure 3.2.

In conclusion, DASC with nanoparticle technology could minimise heat losses and maximise efficiency [38, 55]. Saidur et al. [65] evaluated the performance of a DASC with various working fluids and discovered how the DASC is limited by the absorption properties of the working fluid. They also evaluated how the volume fraction affects the efficiency, and concluded that low VF is essential to avoid drawbacks like clogging and unstable suspensions.
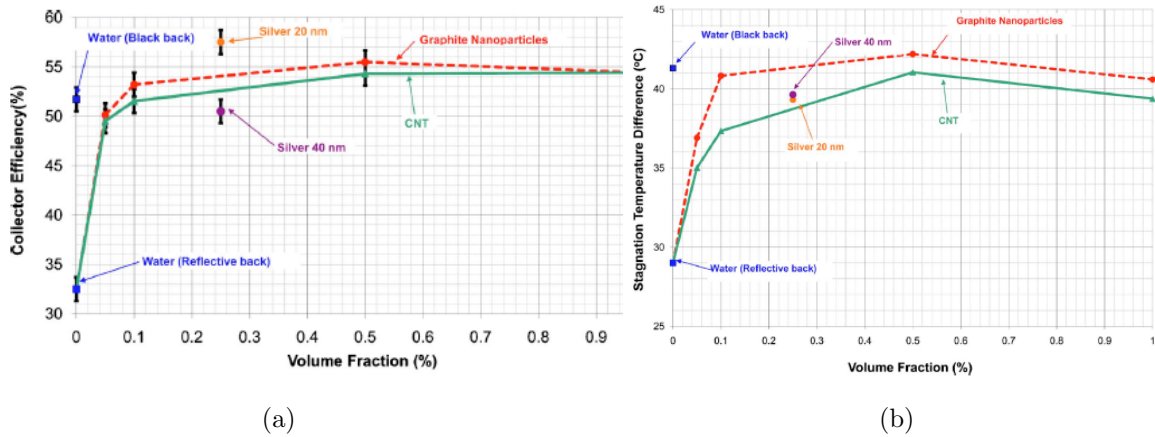

(a) (b)

Figure 3.2: Experimental microsolar thermal collector test results for: a) thermal efficiency and b) temperature [55].

Luo et al. [45] investigated performance improvements of a DASC solar collector with nanofluids. They used a simulation model combining the radiative heat transfer in a particular media with convective and conductive heat transfer in the DASC collector to predict the photothermal efficiency. different NPs were used. The simulation results include how specific NPs can have acceptable performances to improve the efficiency of a DASC [45]. Also, Gorji and Ranjbar [23] studied how to optimise the dimensions of a nanofluid filled DASC. They focused on the DASC geometry and its effect on thermal efficiency and entropy. One of the conclusions was that increased length and larger heights were beneficial for thermal efficiency and entropy but had the opposite impact on the overall performance. Sharaf et al. [68] investigated the geometry of microsized collectors. Their study indicated that lower collector heights gives the best collector

performance. Additionally, different surface materials were tested.

The numerical and experimental research done by Otanicar et al. [55] is inadequate when it comes to particle concentration effects on collector performance. Additionally, there is a lack of numerical research done on geometry optimisation of microsized collectors, and the influence of nanofluid velocity on collector efficiency. Finally, it could be interesting to obtain more information on how Brownian motion and thermophoresis influence the nanofluid flow.

In this study, a pragmatic CFD model of the nanofluid-based DASC based on the E-E approach was created to study the thermal efficiency of the DASC under solar radiation. The DASC consists of a plating container filled with water and graphene nanoparticles. The plate has the same dimensions as the plate in the DASC investigated by Otanicar et al. [55]. The article by Otanicar et al. is used for comparing their experimental results with the new model made for this thesis. The new model considers volumetric absorption of the incident light and how different forces affect the collector efficiency. This model was made in the CFD software STAR-CCM+. Theoretical analysis and validation are performed for all correlations.

Chapter 4

Model Description

This chapter describes the continuity, momentum and energy relations used to describe the model. Relations for volumetric absorption of heat, Brownian motion and thermophoresis were included in the model by making user-defined functions in STAR-CCM+.

4.1 Governing Equations

The nanofluid used is modelled using the E-E two-fluid model, which assumes that both phases (base fluid and nanoparticles) constitute two different interpenetrating fluids, with equal pressure. The system with the two phases is, therefore, described by two distinct systems of Navier-Stokes equations. Conservation equations were used separately for each of the phases. The continuity equation is [76]:

$$\frac{\partial(\alpha_i \rho_i)}{\partial t} + \nabla(\alpha_i \rho_i \mathbf{v}_i) = 0, \tag{4.1}$$

where α_i, ρ_i and $\mathbf{v}_i$ are the volume fraction, the density and the velocity vector of the respective phase.

Each phase is denoted by $i = p$ for the nanoparticles and $i = f$ for the base fluid. The Eulerian momentum equation becomes [5]:

$$\frac{\partial(\alpha_i \rho_i \mathbf{v}_i)}{\partial t} = -\alpha_i \nabla p + \nabla(\alpha_i \mu_i \nabla \mathbf{v}_i) + \alpha_i \rho_i \mathbf{g} + \mathbf{F}_D + \delta_{i,j}(\mathbf{F}_B + \mathbf{F}_{Th}), \tag{4.2}$$

where p is the static field pressure, μ_i is the dynamic viscosity, $\mathbf{g}$ is acceleration due to gravity and $\delta_{i,j}$ is the Kroenecker delta. $\mathbf{F}_D$ represents the drag force, $\mathbf{F}_B$ represents the Brownian force, and $\mathbf{F}_{Th}$ represents the thermophoretic force. The volume fraction of the particles in DASC is below 1% so the influence of the particles to the rheology of the nanofluid is assumed as negligible.

Finally, the energy equation can be written [36]:

$$\frac{\partial(\alpha_i \rho_i e_i)}{\partial t} = \nabla(\alpha_i \rho_i \nabla T_i) - q_{ij} + q_{V,i}, \qquad (4.3)$$

where $e_i = C_{pi}T_i$ is the phase-specific enthalpy, q_V is the volumetric heat generation due to absorption of radiant heat by phases. q_{ij} is the inter-phase heat transfer term, which with the assumption that there is a convective heat transfer between the phases, is computed according to Ranz-Marshall [5].

4.2   Interphase Momentum Coupling

When two phases are mixed on a macroscopic level, they influence each other. This influence is called coupling, and the flow can be either one-way or two-way coupled. The one-way coupling means that only the continuous phase impacts the dispersed phase. The two-way coupling means that the continuous phase impacts the dispersed phase, but the dispersed phase also impacts the continuous phase [16].

In general, the dispersed phase is driven by the motion of the continuous phase. Considering that the particle size is small, the hydrodynamic effect of the NPs on the base fluid is negligible. Also, particle-particle interactions are negligible in dilute concentrations and not considered here. The interparticle forces such as Van der Waals and electrostatic forces can also be neglected, due to their minimal contribution [81]. The particle movement is affected by many slip mechanisms, e.g. fluid drag, inertia, gravity, thermophoresis, Brownian motion. Momentum coupling between phases occurs as a result of these mechanisms. For nanoparticles, the Brownian force, thermophoretic force, and the flow drag force are the dominating mechanisms [84]. As the number of particles is high, direct simulation of inter-particle collisions is not practicable because of high computational cost and large storage requirements.

Figure 4.1 illustrates how the forces act on a nanoparticle in a fluid with a temperature gradient. The blue arrows represent the water flowing, and black arrows represent forces. Forces shown here are Brownian force (F_B), thermophoretic force (F_{Th}) and drag force (F_D). The small black dots represents the water molecules, and the lager sphere is the nanoparticle.

4.2.1   Particle Drag Force

The coupling that occurs in multiphase flows gives rise to several inter-phase forces. One of these forces is the drag force. The drag force is the force exerted on the particle by the fluid. There are two contributions to drag, the component of wall shear, τ_{wall}, and fluid pressure acting normal to the wall, as shown in Figure 4.2. When the wall of an object is parallel with the direction of flow, only the shear force makes a contirbution to the drag force. More generally, the wall of an immersed object makes an angle with the direction of flow. Then the component of the wall shear in the direction of the flow contributes to the drag [49].

Total drag on a spherical object (as shown in Figure 4.2) is the sum of the integrals of these quantities over the entire surface. The total integrated drag from wall shear is the wall drag,
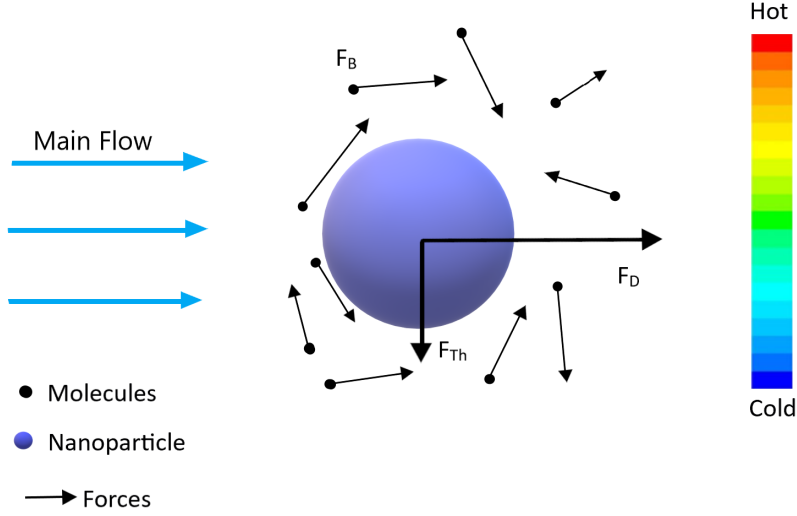
Figure 4.1: Illustration of forces acting on the nanoparticle. Brownian force (F_B), thermophoretic force (F_{Th}) and drag force (F_D).

and the total integrated drag from pressure is called form drag. Drag depends on the fluid properties, the size, and shape of the object and the relative velocity between the continuous fluid and the object. A steady-state drag is the drag force that acts on the particle in a velocity field when there is no acceleration of the relative velocity between the particle and the carrier fluid. A general form of the steady-state drag force can be quantified by the drag coefficient, and is defined as [16, 20]:

$$F_{ss} = \frac{1}{2}C_D\rho_f A(u-v)\,|u-v|\,,\tag{4.4}$$

where v is the particle velocity, and u is the fluid velocity, C_D is the drag coefficient, A is the representative area of the particle. The drag coefficient depends on the particle shape and orientation to the flow, as well as the flow parameters such as *Reynolds number, Mach number*, turbulence level, and more. C_D can be defined using an empirical correlation developed for laminar flow by Schiller-Naumann [39]:

$$C_D = \begin{cases} \frac{24}{Re_r}(1 + 0.15Re_r^{0.687}) & Re_r \leq 1000 \\ 0.44 & Re_r > 1000 \end{cases}\tag{4.5}$$

The Reynolds number used in Schiller-Naumann, is the relative Reynolds number of the dispersed phase, which is defined as [49, 85]:

$$Re_r = \frac{\rho_f\,|v|\,d_p}{\mu_f}.\tag{4.6}$$

The drag force in the simulations is computed using the standard expressions by Schiller- Naumann. Due to rarefication effects, no numerical model can provide the particle drag coefficient
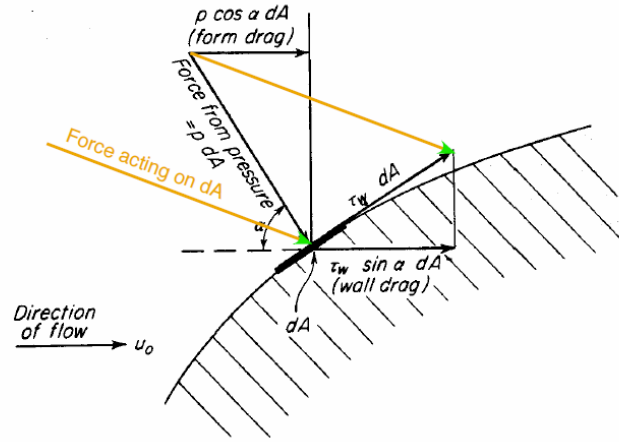
Figure 4.2: Illustration of drag force on particle surface [49].

for particles all over the regime. A classic experiment for free molecule flow was carried out, and the drag of the drop varied with a factor, now called the *Cunninghams correction factor* [5]:

$$C_c = 1 + Kn(2.49 + 0.85\exp[-1.74/Kn]), \tag{4.7}$$

where Knudsens number $Kn = \lambda_m/d_p$, $d_p = 30$ nm is the size of the particles and λ_m is the molecular mean free path in the base fluid. The drag force in the simulations was corrected with Cunningham's correction.

This thesis explored the effect of the drag force. The Schiller-Naumann expression for drag force was corrected with the retardation factor adapted from Rastegar et al. [61]. This retardation factor is calculated to account for velocity reductions close to the walls [41]. Rastegar et al. [61] calculated the drag force from:

$$F_D = m_p \frac{18\mu_f}{d_p^2 \rho_p C_c f_{HR}}(\mathbf{u} - \mathbf{v}), \tag{4.8}$$

where m_p is the nanopatricle mass and f_{HR} is the retardation factor. This drag force is used for theoretical calculations only, since the Schiller-Naumann drag used in the simulations has a function in STAR-CCM+. The coefficient f_{HR} for the radial and tangential velocity components were calculated by Rastegar et al. [61] as:

$$f_{HR_r} = 1 - \left(\frac{9}{8}\right)\left(\frac{d_p}{2y}\right) + 0.5\left(\frac{d_p}{2y}\right)^3 \tag{4.9}$$

$$f_{HR_t} = 1 - \left(\frac{9}{16}\right)\left(\frac{d_p}{2y}\right) + \left(\frac{1}{8}\right)\left(\frac{d_p}{2y}\right)^3 - \left(\frac{45}{256}\right)\left(\frac{d_p}{2y}\right)^4 - \left(\frac{1}{16}\right)\left(\frac{d_p}{2y}\right)^5, \tag{4.10}$$

where y is the distance from nanoparticle to the wall of the container. To use this combined retardation factor, it is necessary to use this relation:

$$f_{HR} = \sqrt{f_{HR_r}^2 + f_{HR_t}^2}. \tag{4.11}$$

4.2.2 Brownian Motion

Brownian motion is the random movement of the particles in a fluid due to their collisions with other atoms or molecules [32]. There is an absolute dependence on the nature of the fluid medium, especially its viscosity. Since the viscosity is temperature dependent, so is the Brownian motion magnitude. Brownian motion is also stable in time, and persists as long as the particle remains in the fluid [48]. The size of the surrounding medium and the particles affected influence the force magnitude. For nanosized particles, the force magnitude is very high. The particle diffusion is much higher than for large particles, and leads to a high particle deposition rate [84]. Brownian motion can be considered as a macroscopic picture of a particle influenced by many microscopic random effects (as seen in Figure 4.1). The mathematical description of Brownian motion is a relatively simple probability calculation. It can be considered as a Gaussian white noise process. The Brownian motion of a microparticle in fluid in one dimension is governed by the Langevin equation [18, 48]:

$$\frac{\mathrm{d}u}{\mathrm{d}t} + Bu = F(t). \tag{4.12}$$

Dong et al. [18] solved the Langevin equation for one-dimensional motion of a single particle in Brownian liquid:

$$F_B = F(t) = \xi \sqrt{\frac{\pi S_0}{\Delta t}}. \tag{4.13}$$

with spectral intensity:

$$S_0 = \frac{2k_B T_c B}{m_p C_c}, \tag{4.14}$$

where $B = \alpha/m_p$, $\alpha = 3\pi\mu_c d_p$ and $m_p = \pi d_p^3/6$. Using these relations yield:

$$S_0 = \frac{216 k_B T_c \mu_c}{\pi d_p^5 \rho_p^2 C_c}, \tag{4.15}$$

where k_B is the Boltzmann constant. For numerical purposes it is helpful to calculate the force acting over each cell, since it's Eulerian modeling, and so the number density of the dispersed phase (particles) is added. Rewritten for three-dimensional motion, and validated, the correlation becomes:

$$\mathbf{F}_B = m_p n_p \sqrt{\frac{\pi S_0}{\Delta t}} (\xi_1 \mathbf{e}_x + \xi_2 \mathbf{e}_y + \xi_3 \mathbf{e}_z), \tag{4.16}$$

where n_p is the number density of the particles, ξ_i are zero-mean and unit-variance Gaussian random numbers, generated independently of each other within a solution time step Δt, and $\mathbf{e}_i$ are unit vectors in x,y, z-direction. This correlation accurately describes the computation in STAR-CCM+, and gives a value of the Brownian force in each computational cell. The random number generation procedure is described in detail in the numerical procedure (chapter 5).

4.2.3   Thermophoresis

The phenomenon of thermophoresis stands for particle transport due to a temperature gradient [1]. Dispersed phase particles tend to move from the higher-temperature region to the lower-temperature region, due to thermophoresis [84]. The higher molecular velocities on one side of the particle, due to a higher temperature, gives rise to more momentum exchange and a resulting force in the direction of decreasing temperature [16]. Thus, the force acts in the direction of the negative temperature gradient vector in the area and is proportional to the vector magnitude [1]. Thermophoresis in dilute suspensions is driven by hydrodynamic stresses resulting from a local interaction between particle and fluid [14]. Equations provided by Brock [13] provides the best fit with experimental data over a wide range of Knudsen numbers and thermal conductivity ratios [16]:

$$F_{Th} = \frac{-6n_p\pi\mu_f\nu_f d_p C_s}{1 + 6C_m Kn} \frac{k_f/k_p + 2C_t Kn}{1 + 2k_f/k_p + 4C_t Kn} \nabla T, \tag{4.17}$$

where C_s is the thermal slip coefficient, C_t is the thermal exchange coefficient and C_m is the momentum exchange coefficient. The best values based on kinetic theory are $C_s = 1.17$, $C_t = 2.18$ and $C_m = 1.14$ [16].

4.3   Interphase Heat Transfer

One of the physics models chosen in STAR-CCM+ is the Multiphase Segregated flow with the Phase Coupled Fluid Energy model. These models indicate that the heat transfer mechanism between the two phases is thermal diffusion. Thermal diffusion is modelled in STAR-CCM+ as [71]:

$$q_{ij} = -q_{ji} = h_{ij}A_{ij}(T_j - T_i), \tag{4.18}$$

where q_{ij} is the interphase heat transfer rate, h_{ij} is the mean surface average heat transfer coefficient, and A_{ij} is the interfacial area per unit volume. The mean heat transfer coefficient, specific for the nanofluid, is computed as a function of the nanofluid thermal conductivity, the Nusselt number and particle diameter [16]:

$$h_{nf} = \frac{k_f Nu}{d_p}, \tag{4.19}$$

where Nu is calculated using the Ranz-Marshall correlation [70]:

$$Nu = 2 + 0.6Re^{\frac{1}{2}}Pr^{\frac{1}{3}}, \tag{4.20}$$

where Re is the nanoparticle Reynolds number and Pr is the Prandtl number of the base fluid. The Ranz-Marshall correlation is valid for $Re \in (0, 200)$ and $Pr \in (0, 250)$ [21].

4.4 Volumetric Heat Generation

Figure 4.3 shows the heat flow through the nanofluid DASC. The nanofluid is contained in an enclosed space between two parallel plates. Heat flux from the solar radiation is transmitted vertically through the transparent top plate and is absorbed volumetrically by the suspended graphite nanoparticles. The base fluid is simultaneously heated from the absorbed heat from the NPs. The transparent glass surface allows most of the solar radiation to pass through. Following Otanicar et al. [55], the top boundary was indentified as the only source of thermal losses with an equivalent heat transfer coefficient as in the range $h \in [23, 34]$ W/m^{2}K. The coefficient accounts for thermal leaks due to convection of air around the collector at the ambient temperature of $25\,°C$.

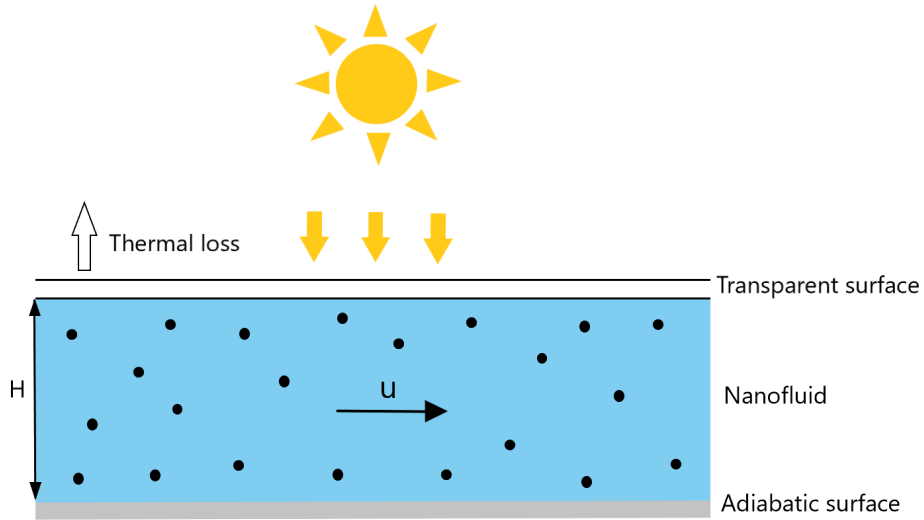Figure 4.3: Schematic of the heat flow in a nanofluid-based direct absorption collector.

The volumetric heat generation in nanofluid exposed to solar radiation was derived following Bohren and Huffman [12], where the extinction cross-section of an individual spherical particle reads as:

$$C_{ext} = \frac{2\pi}{|x(\lambda)|^2} \sum_{i=1}^{\infty} (2i + 1)\Re\left[a_i + b_i\right]. \tag{4.21}$$

In Eq. (4.21) λ is a wavelength, $x(\lambda) = 2\pi n(\lambda)/\lambda$ is a wave number; $n(\lambda)$ is a real part of the complex refractive index of the base fluid, and a_i and b_i are coefficients of scattered electromagnetic field, that can be written as follows [6]:

$$a_i = \frac{m\psi_i(m\overline{\alpha})\psi_i'(\overline{\alpha}) - \psi_i(\overline{\alpha})\psi_i'(m\overline{\alpha})}{m\psi_i(m\overline{\alpha})\xi_i'(\alpha) - \xi_i(\overline{\alpha})\psi_i'(m\overline{\alpha}}; \tag{4.22}$$

$$b_i = \frac{\psi_i(m\overline{\alpha})\psi_i'(\overline{\alpha}) - m\psi_i(\overline{\alpha})\psi_i'(m\overline{\alpha})}{\psi_i(m\overline{\alpha})\xi_i'(\overline{\alpha}) - m\xi_i(\overline{\alpha})\psi_i'(m\overline{\alpha})}, \tag{4.23}$$

where m is a complex refractive index of the particle relative to the base fluid; $\overline{\alpha} = \pi n(\lambda)d_p/\lambda$ is the size parameter of particle; $\psi_i(z)$ and $\xi_i(z)$ are Riccati-Bessel functions of i-th order. Riccati-Bessel functions are related to the Bessel functions of the first (J_ν) and second (Y_ν) kind: $\psi_i(z) = \sqrt{\pi z/2}J_{i+1/2}(z)$ and $\xi_i(z) = \sqrt{\pi z/2}(J_{i+1/2}(z) + Y_{i+1/2}(z))$.

As can be seen from Eq. (4.21), the expression of the extinction cross-section includes infinite series that are hardly resolved numerically. In order to simplify this calculation, a maximum index n_{max} is used. According to Kiran and Diaz [40], a maximum index can be calculated as: $n_{max} = \left[2 + \overline{\alpha} + 4\overline{\alpha}^{1/3}\right]$.

The extinction coefficient of particles in nanofluid with volume fraction α_p can be calculated according to Taylor et al. [73]:

$$\sigma_p = \frac{3}{2}\alpha_p\frac{Q_{ext}}{d_p}, \tag{4.24}$$

where Q_{ext} is the extinction efficiency, which is related to the extinction cross-section, as $Q_{ext} = C_{ext}/S_p$; S_p is the area of the particle cross-section.

The total extinction coefficient of the nanofluid is composed of particle and base fluid extinction coefficients:

$$\sigma_{nf} = \sigma_p + (1 - \alpha_p)\sigma_f, \tag{4.25}$$

where σ_f=52m^{-1} [75] is the extinction coefficient of the continuous phase, which can be calculated according to Bohren and Huffman [12] as $\sigma_f = 4\pi k(\lambda)/\lambda$; and $k(\lambda)$ is the imaginary part of the complex refractive index of the base fluid. The optical properties of the base fluid $k(\lambda)$ and the particles m are found elsewhere [29, 59].

In order to calculate the solar heat flux in nanofluid as a function of distance from the entrance to the volume of nanofluid, and dependent on particle concentration, it is necessary to specify the spectral distribution of incident radiation $I(\lambda)$, which is given in [11, 25, 26].

According to Beer-Lambert's law, the solar heat flux in nanofluid reads as:

$$q = \int_0^\infty I(\lambda)\exp\left[-x\sigma_{nf}\right]dx. \tag{4.26}$$

Eq. (4.26) is hardly applicable for use in CFD simulation due to the high computational costs associated with integration of the function. To realise the calculation of solar heat flux in CFD simulation, the equivalent depth of optical penetration l_{eq} was computed for 30-nm carbon
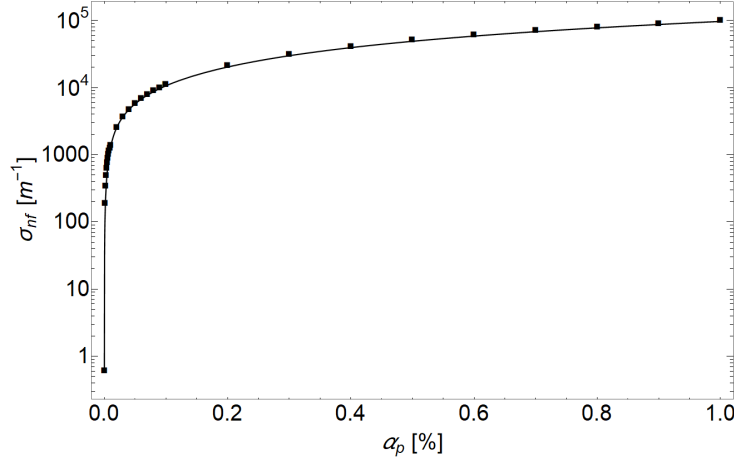
Figure 4.4: Equivalent extinction coefficient as a function of particle concentration [6].

nanoparticles at different particle concentrations. The equivalent depth of optical penetration is defined as a distance from the light entrance to the nanofluid, towards the place at which the total heat flux becomes e times smaller. Thus, the equivalent depth of optical penetration is computed when the numerically-solved Eq. (4.26) becomes equivalent $q_0 e^{-1}$. The reciprocal of the equivalent depth of optical penetration, $\overline{\sigma_{nf}} = l_{eq}^{-1}$, is considered as the equivalent extinction coefficient.

Eq. (4.26) was solved numerically outside the CFD model for a variety of nanoparticle concentrations. The integral in Eq. (4.26) was computed using the trapezoidal rule with 1 nm wavelength steps. Further, the equivalent extinction coefficient was fitted as a function of particle volume fraction with a simplified expression of the type using the conjugate gradient method [6, 33]:

$$\overline{\sigma_{nf}} = \frac{2}{\pi}(A + B\alpha_p)\arctan\left(\kappa\alpha_p\right) + \overline{\sigma_f}. \tag{4.27}$$

Fitting the equivalent extinction coefficient $\overline{\sigma_{nf}}$ with the expression from Eq. (4.27) resulted in the following values of fitting coefficients: $A = 2020.07\mathrm{m}^{-1}$, $B = 9.53094 \cdot 10^6\mathrm{m}^{-1}$ and $\kappa = 8031.63$. In this equation, $\overline{\sigma_f}$ is an equivalent extinction coefficient of the base fluid. The approximation result is presented in Fig. 4.4, where the extinction coefficient is resolved numerically (line) and compared to Eq. (4.27) (boxes) for different particle concentrations.

The solar heat flux in nanofluid can be therefore written as $q = q_0\exp\left[-x\overline{\sigma_{nf}}\right]$, where q_0=1kW/m^2 is the incident solar radiation. The volumetric heat generation then becomes [6]:

$$q_v = -dq/dx = q_0\overline{\sigma_{nf}}\exp\left(-\overline{\sigma_{nf}}l\right), \tag{4.28}$$

where l is the optical path in the direction of thermal radiation and $\overline{\sigma_p} = \overline{\sigma_{nf}} - \overline{\sigma_f}$.

4.5   Surface Absorption

A surface absorption system converts the solar radiation into thermal energy of the working fluid with two steps. First, the solar radiation is absorbed by the surface, and then the energy is

transferred to the fluid through conductive and convective heat transfer. In surface absorption systems, the solar radiation absorption is a characteristic of the surface material. A surface can only absorb a part of the incident solar radiation. How much is absorbed is determined by the absorption efficiency α. The energy absorbed per unit surface is:

$$\frac{Q_{abs}}{A} = \alpha q_0. \tag{4.29}$$

In this thesis, black surface absorption was tested. For these cases, $\alpha = 1$, all radiation is absorbed by the surface. However, thermal losses also have to be accounted for. The specific conditions for top and bottom surfaces are described as boundary conditions in section 5.3.2.

Chapter 5

Numerical Procedure

Multiple factors need to be specified when making an effective CFD simulation that generates reliable results. This chapter shows the numerical set-up for the simulations done in STAR-CCM+ based on the model description from chapter 4.

5.1 Geometry

The flat-plate geometry modelled in this study was adapted from Otanicar et al. [55], who constructed a micro-scale-thermal-collector pumping a nanofluid between two parallel plates with dimensions 3×5 cm^2. The thickness of the gap was 150 μm. The microchannel geometry is presented schematically in Figure 5.1. The microchannel geometry was selected to minimise the amount of nanofluid necessary for each collector test. Simultaneously, this collector height allowed for the measurement of appreciable temperature gain for the pure fluid cases, while allowing an extensive range of nanofluids to be tested where the expected amount of energy reaching the bottom of the channel is nonzero [55].

For simplification and computational time reduction purposes, an axisymmetric cross-section of the plate is used in these simulations. The length of the cross-section is 5 cm, the width 45 μm and the height 150 μm. The symmetry axis is implemented to get an overview of how the plate model behaves.

Figure 5.1: Geometry for illustration purposes. Dimensions are not correct.

5.2   Mesh

The mesh chosen for the simulation is shown in Figure 5.2. Three-dimensional cells in an ordered collection define a closed volume in space [71]. These cells are generated for solvers that use the finite-volume method. A hexahedral mesh with uniform size through the computational domain was used. By default, the meshing model uses a template mesh constructed from hexahedral cells at the target size from which is cuts or trims the core mesh using the starting input surface [71]. The computational domain was discretised with uniform 20 μm cubical mesh.
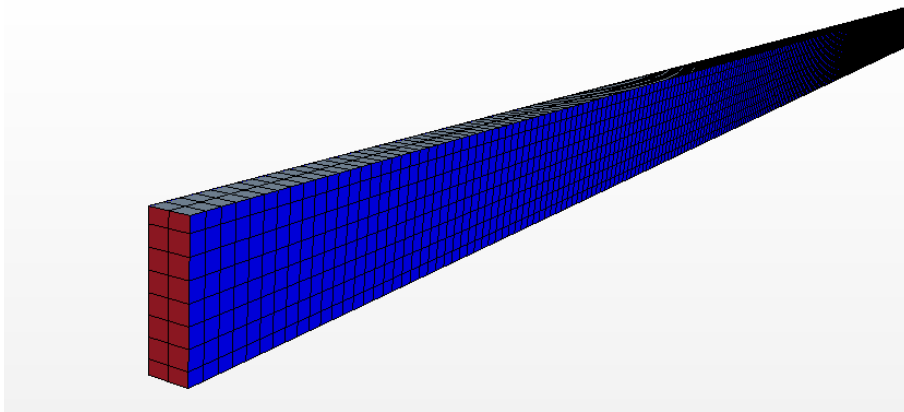

Figure 5.2: Mesh chosen for simulations. Base size is set as 2×10^{-5}m.

Defining an optimal mesh is important for accurate results. A satisfactory mesh should give similar results as a finer mesh, without being too time-consuming. A mesh optimisation study was done to decide which mesh was optimal. The simulation used for studying the mesh is presented as Model 1. In this simulation, no momentum source was added. The outlet temperature and ΔP were used to validate the results.

The mesh study resulted in optimal base size of 2×10^{-5}m. Table 5.1 compares the measured values.

Table 5.1: Comparison of the different meshes.

Base size	Cells	Outlet temperature [°C]	ΔP [Pa]
1×10^{-5}m	480 000	43.28	61.15
2×10^{-5}m	40 000	43.13	61.79
4×10^{-5}m	10 000	41.48	87.8

5.3 Boundary Conditions

In this section, boundary conditions used for the simulations are described. Boundaries are surfaces that surround and define a region [3]. There are different boundary conditions computed for black surface absorbers and volumetric absorption. However, they have some conditions in common. These boundary conditions include two symmetry planes at the frontal surfaces of the model, and a velocity inlet on the left of the section studied. The inlet boundary condition sets the uniform distribution of velocity, volume fraction and temperature (25 °C). The equivalent flow parameters were set for the initial condition. The outlet boundary defines the zero field of relative pressure, uniform distribution of volume fraction and zero gradient of temperature at the exit of the model. The bottom and the top boundary are the no-slip walls. The no-slip boundary condition for viscous flow assumes no relative velocity between the surface and the phase in immediate contact with the surface.

The top wall of the DASC is exposed to solar radiation, and the distribution of volumetric heat generation is set accordingly in Eq. (4.28). Following Otanicar et al. [55], the top boundary was identified as the only source of thermal losses. At the inlet, the boundary conditions equal the initial conditions set for the fluid:

$$x = 0, \quad 0 < y < H, \qquad T(0, y) = T_{inlet} \tag{5.1}$$

There are different alternatives for the top and bottom boundary condition. Primarily the model consists of a transparent top and an adiabatic bottom. However, to understand the influence of a blackbody top and bottom of the collector, constant heat flux were prescribed to the surfaces.

5.3.1 Volumetric Absorption

It is necessary to define boundary conditions for the temperature of the bottom wall. This wall is assumed to be adiabatic, which means there is no heat transfer to this surface. Subsequently, there is no temperature gradient:

$$0 < x \le L, \quad y = 0; \qquad \left(\frac{\partial T}{\partial y}\right) = 0 \tag{5.2}$$

The top wall of the DASC is exposed to solar beams, and because of controlled flow through the plates, the result is forced convection through the nanofluid. The heat flux through the nanofluid is expected to be constant at the axis perpendicular to the top wall. The boundary condition for the top wall is combined convection and radiation:

$$0 < x \le L, \quad y = H; \qquad -k\left(\frac{\partial T}{\partial y}\right) = h[T_{amb} - T(x, 0)], \tag{5.3}$$

where k is the thermal conductivity of the fluid in contact with the wall, y is the distance from the wall, h is the combined convection and radiation heat transfer coefficient experimentally determined by Otanicar et al. [55] and $T(x, 0)$ is the top wall temperature [49].

5.3.2   Black Surface Absorption

After investigating the volumetric absorption, it was interesting to investigate how black surface absorption influence the thermal efficiency of the collector.

Two cases were tested, black top surface and black bottom surface. For the black top wall case, the bottom wall continues to be adiabatic (Eq. (5.2)) and the top wall condition is changed:

$$0 < x \le L, \quad y = H; \qquad -k\left(\frac{\partial T}{\partial x}\right) = q_0 - h_{amb}\Delta T, \tag{5.4}$$

where $q_0 = 1000$ W/m^2 is the incoming solar radiation, h_{air} is the heat transfer coefficient of the ambient air and $\Delta T = T(x, H) - T_{amb}$. $h_{amb}\Delta T$ accounts for the thermal losses from the black top plate to the air surrounding the DASC.

When investigating the black bottom surface, the top wall is transparent and volumetric absorption occurs as described in the previous subsection (Eq. (5.3)). Here, the bottom wall boundary conditions has to include the fact that all radiation not absorbed by the nanofluid is absorbed by the bottom wall. To understand the influence of a black-body bottom of the collector a constant heat flux at the boundary was prescribed. The absolute value of the boundary heat flux was set proportionally to the radiate heat flux absorbed by the bottom of the collector. First, the computation was done with only base fluid. Thus, all incoming radiation is absorbed by the bottom plate. When nanoparticles was added to the model, the bottom wall boundary condition was expressed as:

$$0 < x \le L, \quad y = 0; \qquad -k\left(\frac{\partial T}{\partial y}\right) = q_0 \frac{(q_{V,p})_{y=0}}{(q_{V,p})_{y=H}} \tag{5.5}$$

5.4   Initial Conditions

Nanoparticles were assumed to be of uniform size and spherical. The model specifies the interfacial area available for momentum, heat, and mass transfer between each pair of phases in an interaction. Initial conditions specified in STAR-CCM+ are presented in table 5.2.

Table 5.2: Initial Conditions used in simulations.

Property	Water	Graphite
Diameter [nm]	–	30
Static Temperature [°C]	25	25
Velocity [m/s]	[0.0026, 0, 0]	[0.0026, 0, 0]
Volume Fraction	0.995	0.005

Volume fractions were changed to validate how thermal efficiency changed with changing particle concentration. Various heat transfer coefficients, collector heights and velocities are also studied for optimising collector efficiency.

5.5 Thermodynamic Properties

This section provides an overview of the thermodynamic properties used in the models, and calculations. It is necessary to specify that STAR-CCM+ operates with constant values for different properties; these values are presented in Table 5.3.

Table 5.3: Material properties used in STAR-CCM+ at 25 °C [71, 78].

Property	Water	Graphite
Density [kg/m^3]	997.05	2210
Dynamic viscosity [kg/(m s)]	8.8871 $\times 10^{-4}$	–
Thermal conductivity [W/(m K)]	0.620271	1950
Specific heat [kJ/(kg K)]	4.18	0.709

Some properties are shown in Table 5.3, but most of these properties are not constant for the fluid. Table 5.4 shows how different properties vary with temperature for water. Most of the properties are collected and verified with data from McCabe et al. [49, 74].

The heat transfer coefficient was considered at first to have a constant value at 34 W/m^{2}K, which does not occur in reality. So far, there exists minimal literature on nanofluid convection exploring the heat transfer coefficient. So-called heat transfer characteristics of nanofluid convection published by numerous studies have never reviewed the heat transfer coefficient [67]. Otanicar et al. [55] investigated the heat transfer coefficient in experiments and suggested that the heat transfer coefficient changes with particle concentration. The heat transfer coefficient was in the range $h \in [23, 34]$W/m^{2}K for NP volume fractions $\in [0, 1]$%. This coefficient also accounts for thermal leaks due to convection of air around the collector at the ambient temperature of 25 °C. These values for h were used in a linear regression to find an expression for h at each volume fraction. The results are presented in Figure 5.3, additionally displaying the obtained equation.

Table 5.4: Thermal properties of water, within a temperature range relevant for this thesis [4, 49, 74].

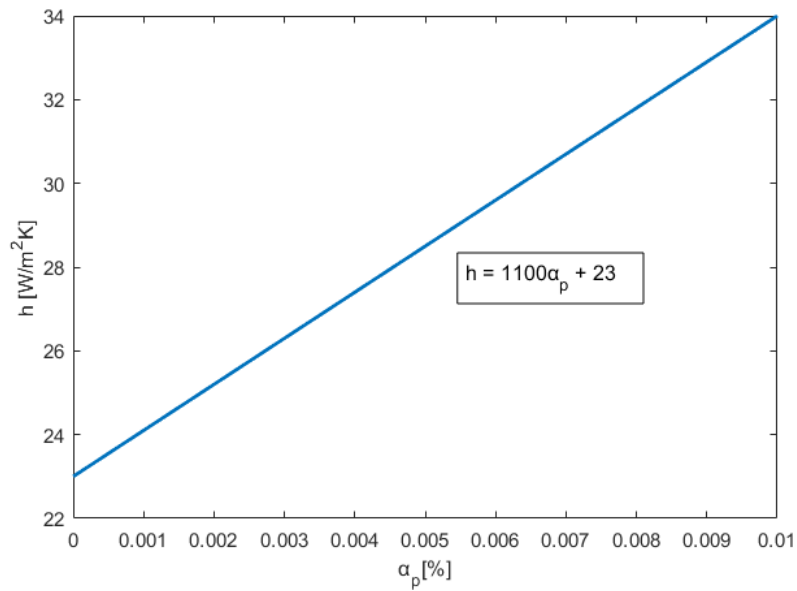| T [°C]	μ [kg/(m s)]	ν [m^2/s]	ρ [kg/m^3]	k [W/(m K)]
25	8.89×10^{-4}	8.90×10^{-7}	997	0.606
30	7.90×10^{-4}	8.01×10^{-7}	996	0.614
35	7.20×10^{-4}	7.24×10^{-7}	994	0.621
40	6.54×10^{-4}	6.59×10^{-7}	992	0.628
45	5.97×10^{-4}	6.03×10^{-7}	990	0.634
50	5.47×10^{-4}	5.54×10^{-7}	988	0.640
55	5.04×10^{-4}	5.11×10^{-7}	986	0.646
60	4.66×10^{-4}	4.74×10^{-7}	983	0.650

Figure 5.3: Heat transfer coefficient vs. volume fraction of particles. Values are extracted from Otanicar et al. [55] and the relation is assumed to be linear.

5.6   Random Number Generator

In this research, Brownian motion was modelled using expressions for Gaussian white noise processes. Gaussian white noise is a stationary and ergodic random process with zero-mean that is defined by one fundamental property: any two values of Gaussian white noise are statistically independent, no matter how close they are in time [47].

The random number factor in the Brownian motion was modelled by the implementation of a pseudorandom number generator. The algorithm is called Lehmer pseudorandom number generator and passes any test for randomness. The algorithm is a type of linear congruential generator for random numbers. The general formula for this random series is adopted from Becker [7]:

$$X_k = gX_{k-1}mod(n), \tag{5.6}$$

where the modulus n is a prime number, and multiplier g is an element of high multiplicative order modulo n. Proposed values from Lehmer are [7]:

$$n = 2^{48} - 1; g = 48271 \tag{5.7}$$

To define an element in this random series (X_k), it is necessary to include the previous value (X_{k-1}) into the calculation. In STAR-CCM+, the field sum monitors are used for storing values for every cell [7]. Figure 5.4 shows the random numbers generated at each physical time step, both showing random numbers generated over a wider region and in each cell. It is only the random numbers generated for each cell that is used in the Brownian motion computation.
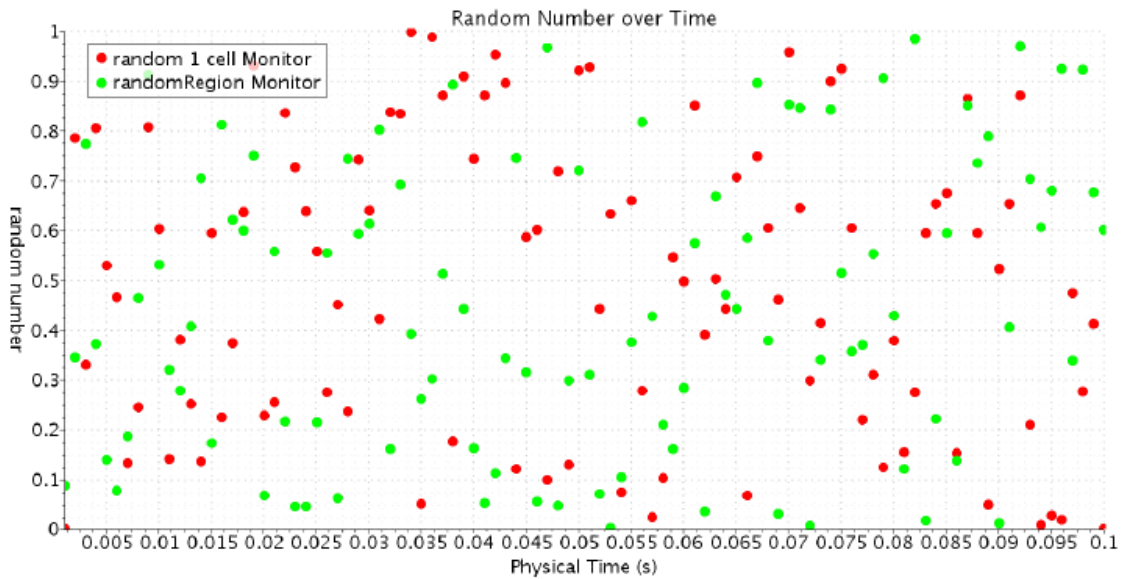

Figure 5.4: Random distribution in time for region and one cell [7].

So far, random numbers $\xi_0 \in [0, 1]$ are generated in every cell. The Brownian force acts in all directions, so it is necessary to generate numbers between -1 and 1. This was done by using the relation:

$$\xi = 2(0.5 - \xi_0). \tag{5.8}$$

5.7 Numerical Models

This section describes all the simulations done, and all models defined in STAR-CCM+. Table 5.5 shows the models and solvers that are common for all simulations. Models and solvers changed are the flow regimes (laminar/turbulent) and time dependency (steady/unsteady). The momentum sources and drag force relations are added as user defined functions, and are described in section 4. The only exception here, is Schiller-Naumann, which is defined directly in STAR-CCM+. Table 5.6 shows the different simulations performed for the first part of this thesis. This part of the simulations focuses on how thermophoresis and Brownian motion influence the nanofluid and the thermal efficiency. The main goal here is to find the best model for describing the collector, compared to the experimental results.

Table 5.5: Models and solvers common for all simulations.

Common models	Solvers
Gravity	
Phase Coupled Fluid Energy	
Multiphase Equation of State	
Multiphase Segregated Flow	
Multiphase Interaction	Partitioning
Eulerian Multiphase	Wall Distance
Three Dimensional	Multiphase Segregated Flow
Lift Force	Volume Fraction
Interaction Area Density	Segregated Energy
Interaction Length Scale	
Mutliphase Material	
Continuous-Dispersed Phase Interaction	

Table 5.7 shows the simulations performed for the next part. Here, the best model is developed further in order to optimise collector performance. The volume fraction (α_p), collector height (H) and nanofluid velocity (u) are changed here. Some models are also changed, to account for turbulence.

Table 5.6: Description of each simulation performed for finding an optimal model.

Case	Momentum Source	Drag Force	h [W/m^{2}K]	Models	α_p
1	None	Schiller-Naumann	34	Laminar Steady	$\in [0,1]$
2a	Thermophoresis	Schiller-Naumann Cunningham Corr.	34	Laminar Steady	$\in [0,1]$
2b	Thermophoresis	Schiller-Naumann Cunningham Corr. Retardation Factor	34	Laminar Steady	$\in [0,1]$
2c	Thermophoresis	Schiller-Naumann Cunningham Corr.	$\in [23,34]$	Laminar Steady	$\in [0,1]$
3a	Brownian Motion	Schiller-Naumann Cunningham Corr.	34	Laminar Implicit Unsteady	$\in [0,1]$
3b	Brownian Motion	Schiller-Naumann Cunningham Corr. Retardation Factor	34	Laminar Implicit Unsteady	$\in [0,1]$
3c	Brownian Motion	Schiller-Naumann Cunningham Corr.	$\in [23,34]$	Laminar Implicit Unsteady	$\in [0,1]$

Table 5.7: Description of each simulation performed for collector optimisation.

Case	α_p [%]	$\mathbf{H}[\mu m]$	$\boldsymbol{u}$ [mm/s]	Bottom Plate	Top Plate	Models
4	$\in [0,1]$	$\in [50, 400]$	2.6	Adiabatic	Transparent	Laminar Steady
5	0.3	150	$\in [1.6, 80]$	Adiabatic	Transparent	Turbulence $K - \epsilon$ RANS y+ Wall Treatment Steady
6a	0	150	2.6	Black	Transparent	Laminar Steady
6b	0	150	2.6	Adiabatic	Black	Laminar Steady
6c	0.3	$\in [50, 400]$	2.6	Black	Transparent	Laminar Steady

Chapter 6

Results and Discussion

This chapter presents the results from simulations and validations against experimental results.

6.1   Validation of the Model

Otanicar et al. [55] experimented with a microscale thermal collector. They used a SuperPAR64 lamp to simulate solar radiation. various volume fractions and particle sizes were tested to understand how these factors impact solar energy thermal collection. The volume fractions were in the range from 0 to 1%, and the particle size was 30 nm. Their results show that the efficiency is limited by the absorption properties of the working fluid. The test apparatus in their study was a plate with dimensions 3×5 cm^2 with thickness 150μm. Otanicar performed both experimental and numerical studies. Therefore, both of these results are included and validated against Case 1 simulation results.

In this thesis, the first simulation (Case 1) was run for various volume fractions. Nanoparticle diameter was held constant at 30 nm. These results were validated against the results extracted from Otanicar. In Case 1 a volume fraction of particles $\in [0, 1]\%$ was used and heat transfer coefficient was 34 W/m^{2}K. The validation of the model was done for two parameters: thermal efficiency of the collector and outlet temperature, and the results are shown in figure 6.1. The thermal efficiency graph includes both the experimental and numerical results from Otanicar. The temperature graph only focuses on the experimental results. The highest temperature is found at the end of the plate ($x = L$). This temperature is the outlet temperature, and is extracted from all simulations done in this research.

Comparing the results in Figure 6.1 shows that Case 1 leads to higher efficiency, but lower efficiency at higher particle concentrations, compared to the numerical model developed by Otanicar et al. [55]. The results from Case 1 deviate from the experimental values, with a maximum discrepancy for $\alpha_p = 0.05\%$. The studied DASC does not entirely absorb the radiant heat at dilute particle concentrations so the efficiency is low there. However, there is a qualitatively similar evolution of the thermal efficiency at various particle concentrations. Thus, the model was valid for testing and was used further in this thesis for developing a more precise model describing nanofluid flow through a flat-plate direct absorption solar collector.
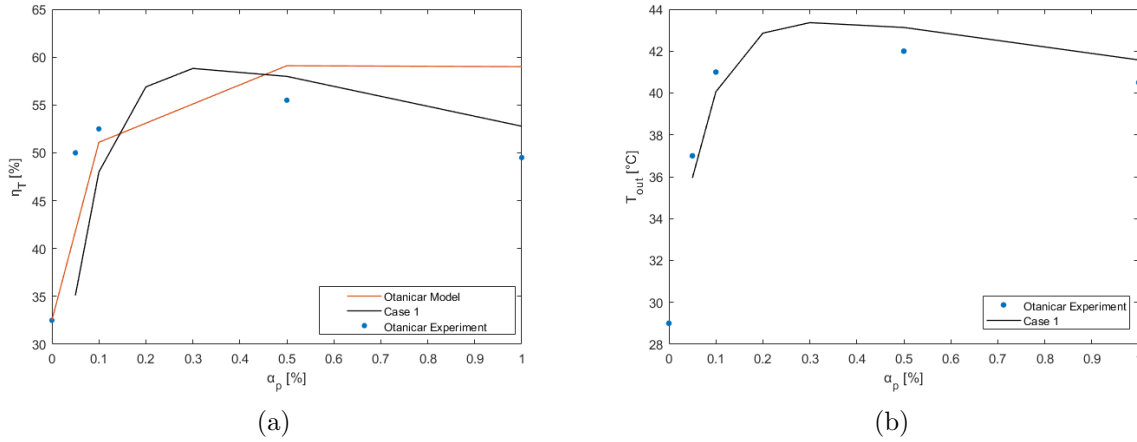
Figure 6.1: Validation of results from Otanicar with results from the new model for: a) thermal efficiency and b) temperature.

6.2   Theoretical Calculations

This section theoretically investigates how the drag, thermophoretic, and Brownian force affect the particles and compares the results with earlier works.

As mentioned in the previous section, Case 1 was run. The results of these simulations are discussed in the previous section. The maximum outlet temperature was $43\,°C$, and the simulation resulted in a temperature gradient in x-direction when $t \to \infty$, and no visible temperature gradient in y-direction. However, it is expected that a thermal boundary layer develops when there is convection. This thermal boundary layer determines the direction of the temperature gradient. To confirm that the thermal boundary layer in y-direction is negligible, its thickness was calculated at various times with Eq. (2.13-2.15) (see values calculated in Appendix A). Since the collector height is low, and the thermal boundary layer develops quickly, the temperature gradient in y-direction makes a minimal contribution. Thus, in this section, it is assumed that the temperature gradient in y-direction can be neglected, and only the temperature gradient in x-direction is used for further calculations.

Predicting the Brownian force effects on the nanoparticles is challenging. According to literature, it is evident that particle size makes a significant contribution on the Brownian force [17, 18, 84]. For larger particles ($d_p > 1\mu m$), the Brownian force is less important. However, for the nanosized particles used in this thesis, Brownian force make a significant contribution. Previous studies have concluded that the net result of the Brownian force is a redistribution of particles between regions with higher particle concentrations to regions with lower concentrations. Thus, the result is a more homogeneous particle distribution [18, 84].

In this study, force magnitudes are calculated for one single graphite particle dispersed in water. This was done by using Eq. (4.4), (4.8), (4.13) and (4.17).

Both the thermophoretic and Brownian forces vary with temperature, and the temperature dependence is shown in Figure 6.2. The thermophoretic force varies with the temperature gradient, so the plotted value is for ΔT in x-direction, where ΔT is the change in temperature from inlet of the collector to the outlet. T_{in} is constant at $25\,°C$, and is set as an initial condition.

T_{out} is measured in the simulations, which is the temperature at the outlet of the collector when $t \to \infty$. The Case 1 simulation was used to define which temperature intervals are relevant for these calculations. The calculations are done for multiple outlet temperatures, in order to estimate temperature effects of the forces. The focus was on Brownian-, thermophoretic- and drag force. The calculated force magnitudes are shown in Figure 6.2, where the blue line represents the Brownian force and red line represents the thermophoretic force. The stapled lines represent the drag force, both steady-state drag and corrected drag. The corrected drag corresponds to the drag force including the retardation factor, Eq. (4.8). Additionally, all values used for theoretical calculations are shown in Appendix A.
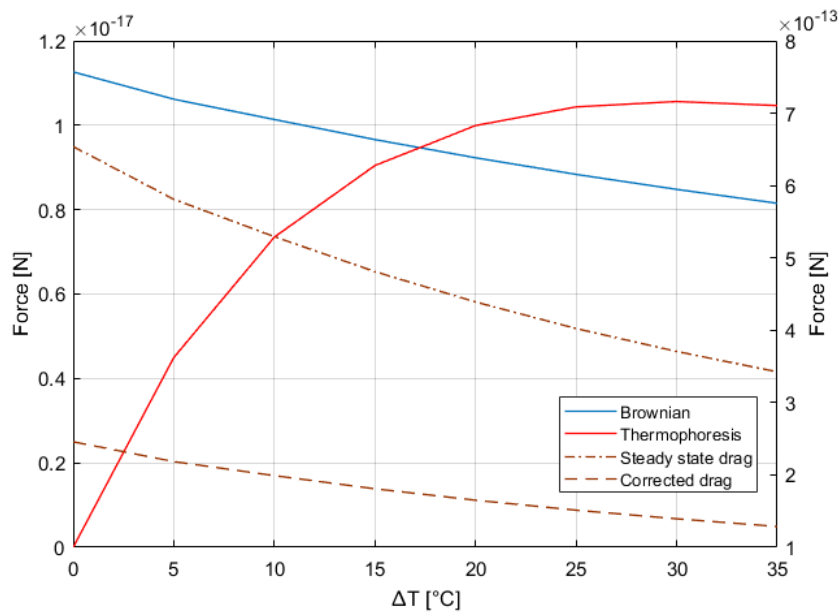

Figure 6.2: The magnitude of the Brownian, thermophoretic and drag forces, based on theoretical calculations. The stapled lines follow right y-axis.

The figure shows that when $\Delta T \approx 17\,°\mathrm{C}$, the magnitude of the thermophoretic force is larger than the Brownian force. It must be noted that the direction of the Brownian force is not considered. The direction is random and individual for each "cell" in the numerical computations. Thus, the Brownian force leads to fluctuations in particle trajectories. As mentioned previously, it is realistic to believe that these fluctuations contribute to a more homogeneous particle distribution. The calculations indicate that the thermophoretic force moves the particle in negative x- and y-direction, possibly disturbing the concentration profile, and making the particle distribution less uniform. This corresponds to the study done by Yin et al. [84].

A theoretical comparison of the forces shows that the Brownian force moves the particles towards a more homogenous distribution, while the thermophoretic force has the opposite effect. Thus, knowing that the temperature increases with time, the Brownian force dominates the particle distribution at first, but later the thermophoretic force dominates.

6.3   Numerical Investigation of Forces

This section presents results from the first part of the simulations. Here, the simulations focuses on how thermophoresis and Brownian motion influence the nanofluid and the thermal efficiency, outlet temperature and deposition. The main goal is to find the best model for describing the nanofluid DASC. The best model was used further as a base case for investigating how the collector performance can be optimised.

The thermal efficiency of the DASC is defined as the ratio of the thermal energy consumed to the incident solar energy [55]:

$$\eta_T = \frac{\int_{y=0}^{y=H} \left(u_o C_{nf,o} \rho_{nf,o} T_{f,o} - u_i C_{nf,i} \rho_{nf,i} T_{f,i} \right) dy}{q_0 \cdot H} \times 100\%, \tag{6.1}$$

where H is the thickness of the collector in the direction normal to flow and q_0 is the solar radiation, $C_{nf} = \alpha_p C_{p,p} + \alpha_l C_{p,l}$ and $\rho_{nf} = \alpha_p \rho_p + \alpha_l \rho_l$ are the equivalent specific heat and the density of the nanofluid, indices o and i denote outlet and inlet boundaries.

Additionally, the deposition efficiency was investigated. It was modelled as:

$$\eta_{dep} = \frac{\alpha_{p,in} - \alpha_{p,out}}{\alpha_{p,in}} \times 100\%, \tag{6.2}$$

where $\alpha_{p,in}$ and $\alpha_{p,out}$ is the volume fraction of particles at inlet and outlet.

The first simulations were done with no momentum source added, and represent Case 1. This case was tested for various volume fractions. Next, Brownian force and thermophoretic force was added as momentum source, in separate models. After evaluating how these forces affected the flow, the drag force was updated to include the retardation factor, for both the thermophoretic and Brownian model. Finally, the models were tested for an updated heat transfer coefficient. All of the models were tested for various volume fractions of particles $\in [0, 1]\%$. All of these simulations were validated against experimental values extracted from Otanicar et al. [55]. Additionally, the simulation with no momentum source added (Case 1) was included in the validations.

The next subsections investigated how to optimise the model in order to make the results correspond better to the experimental results. The goal is to make a model sufficient to investigate and prepare an experiment with this type of DASC.

6.3.1   Thermophoresis

In section 6.2, a theoretical analysis of the thermophoretic force was done, showing that the particles could be potentially moved in a direction opposite to the fluid flow due to the thermophoretic force. This would occur if the thermophoretic force were greater than the drag force. To reduce the computational time, the steady solver was used for the thermophoretic models. There are no time-dependent properties in the equation for thermophoresis, so the result does not change.

An evaluation of the temperature gradient in the collector was done, and Figure 6.3 shows the scenery of the temperature distribution for the Case 2a simulation, and how temperature changes with position after a significant amount of time. When obtaining more accurate results, a function displaying the temperature through the collector was made in Matlab. Figure 6.4a shows that the temperature increases linearly with position, when $t \to \infty$. This indicates that the temperature gradient is constant at this time. Following the research of Burelbach et al. [14], this yields a thermophoretic force through the collector increasing linearly with temperature. To determine if the thermophoretic force acts as predicted, the velocity of the particles was investigated. Velocity profiles are shown in Figure 6.4b. These profiles show that the velocity of the particles decreases after adding the thermophoretic force, and the largest decrease occurs with higher particle concentration. The mutual effect of the thermophoretic force and gravity slightly moves the particles to the middle and bottom of the collector, and decreases the particle velocity in these areas. The velocity decrease is not significant, which relates to the fact that the drag force is dominating. This is also expected, after theoretically evaluating the drag force.

Figure 6.3: Temperature distribution through the collector for Case 2a simulation.
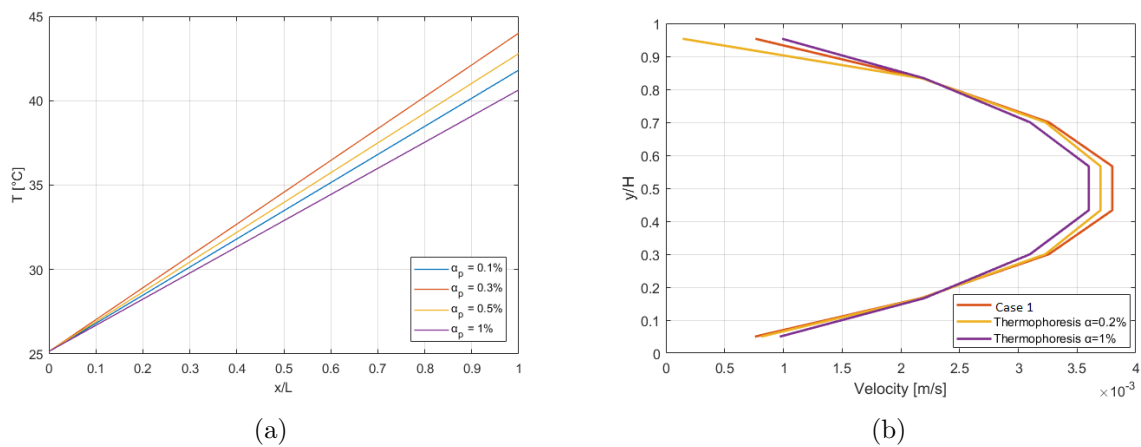

Figure 6.4: Output values from STAR-CCM+ showing how thermophoresis affect the (a) Temperature distribution and (b) velocity profile of the particles.

The changes in thermal efficiency after introducing the thermophoretic force to the model are shown in Figure 6.5. Here, the black line shows Case 1 results with no momentum source added, and the blue dots are the experimental results. The red line (Case 2a) shows the results obtained when the thermophoretic force is included in the model. The figure shows that implementing the thermophoretic force leads to a decrease in efficiency. For volume fractions $\alpha_p = 0.05\%$ and $\alpha_p = 0.1\%$, the thermophoretic model corresponds to Case 1, but significant deviations occur for higher volume fractions.

The results from the thermophoretic model with higher volume fractions is in better agreement with the experimental values. There are large deviations in efficiency from the experimental values for $\alpha_p = 0.05\%$. This is related to an inaccuracy in the volumetric absorption in the model for such low particle concentrations.
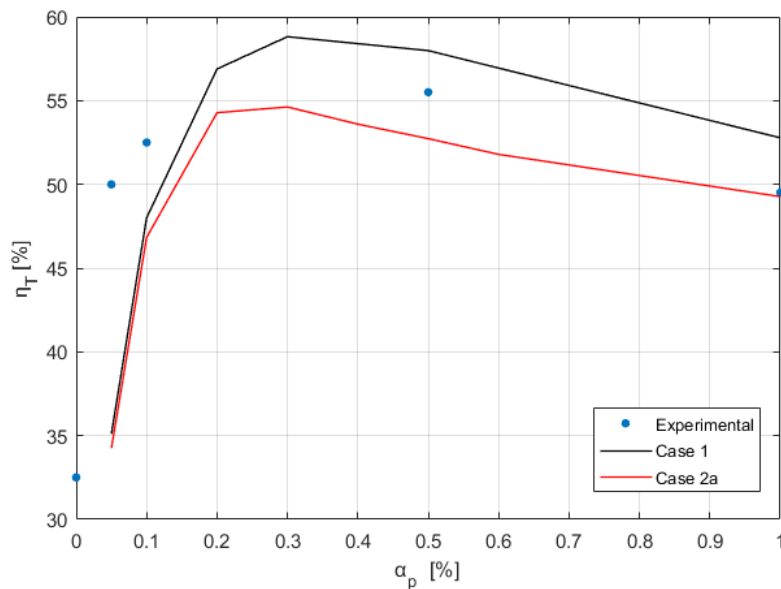

Figure 6.5: Thermophoresis effects on the thermal efficiency.

Figure 6.6a shows how the outlet temperature changes when adding the thermophoretic force to the model. The maximum temperature decreases from 43 °C to 42 °C. The curve representing the results from the model including the thermophoretic force also shows deviating values. However, as seen for the efficiency, updating the model with thermophoretic momentum source yields results closer to the experimental values.

Previous research shows that the nanoparticle deposition increases when including the thermophoretic force in the model [1, 84]. Is has also been observed that a higher temperature gradient leads to a higher deposition efficiency. Yin et al. [84] state that the deposition efficiency is dominated by the Brownian force when $d_p \leq 30$nm, so it is expected that the thermophoretic force impact on the nanoparticle deposition is low. Figure 6.6b shows how the nanoparticle deposition efficiency changes with volume fraction. Here, the red line represents the results from the model with thermophoretic force, and the black line represents results from Case 1. One observation is that the deposition efficiency is higher than for Case 1, but this is expected. The values are not high, mostly between 5% and 6%. The decrease in deposition efficiency as volume

fraction increases occurs because higher volume fraction results in lower temperature, and lower impact of the thermophoretic force.
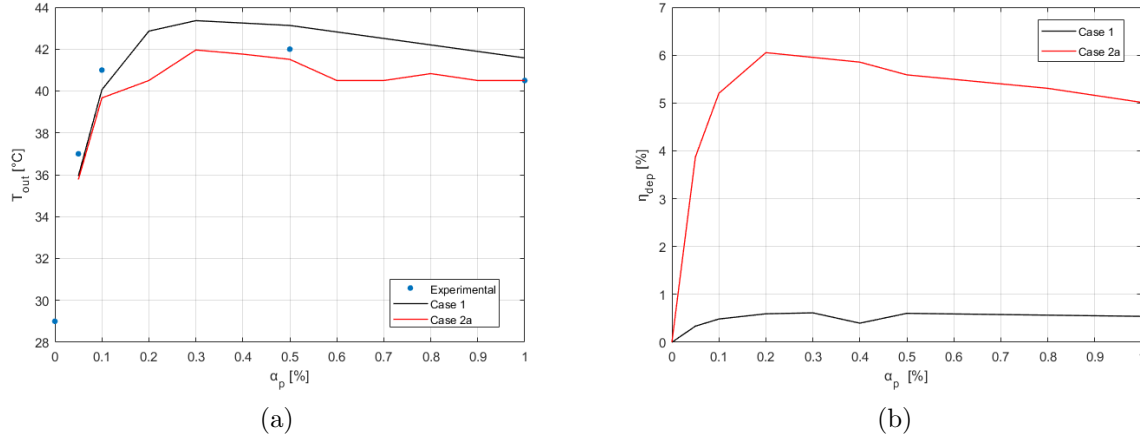

Figure 6.6: Thermophoretic force effects on: a) outlet temperature and b) nanoparticle deposition efficiency.

6.3.2 Brownian Motion

The Brownian force has a significant effect on particle distribution and behaviour [17, 18, 84]. This is obvious from Figure 6.7, which shows how the thermal efficiency oscillates for each iteration step. This figure shows the results obtained in STAR-CCM+ for the simulations done for $\alpha_p = 0.3\%$, which is the volume fraction that yields the highest thermal efficiency for this model. The blue line shows the results after adding the Brownian force, and the yellow line shows the results from the Case 1 simulation. The randomness of the Brownian force, both in magnitude and direction, causes the efficiency to have large oscillations. This Brownian force behaviour correlates to the behaviour observed by Dong et al. [18].

In this research, it was not possible to read an accurate convergence value from the efficiency plot. Thus, to obtain the most precise result for the Brownian force, the convergence curve was averaged in Matlab. Averaging is a technique used to recover one average value from a set of results with deviating values [9]. These averaged values were extracted from each simulation, and plotted in Figure 6.8.

Figure 6.8 shows the results from simulations after implementing the Brownian force. Here, the blue dots represent the experiments, the black line shows the results from the model with no momentum source (Case 1) and the yellow line shows the results obtained when adding the Brownian force to the model (Case 3a). The results show that there is a very small discrepancy of results from the no-momentum source model and the Brownian model. This indicates that even if the Brownian force has an effect on the particles in the flow, the average impact over time does not have a significant impact on the thermal efficiency of the collector. However, there is an increase in efficiency when $\alpha_p \in [0.6, 0.9]\%$, which is explained by the increasing action of the Brownian force with decreasing temperature.

Studying the particle velocity vectors also gives an estimate of the fluctuating particle movement obtained from the Brownian force. Since this simulation utilises the E-E method, it is not
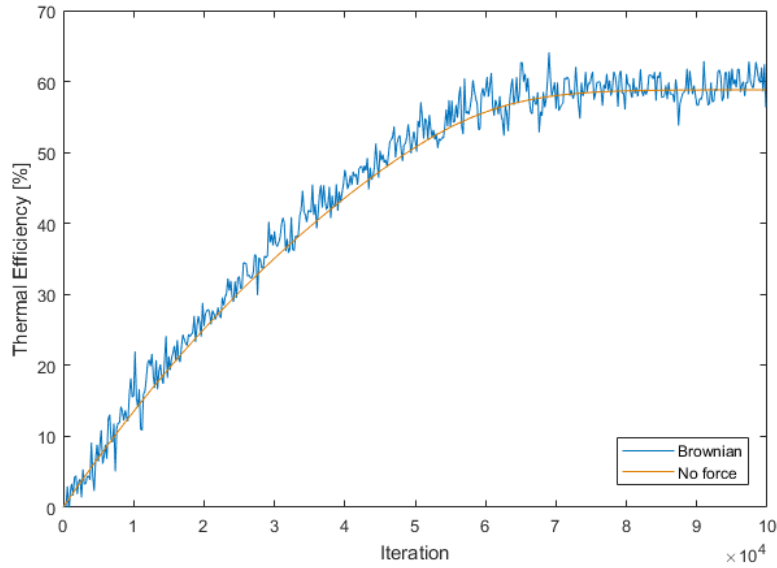
Figure 6.7: Results obtained from STAR-CCM+ before and after including the Brownian force to the model, as a function of iteration.
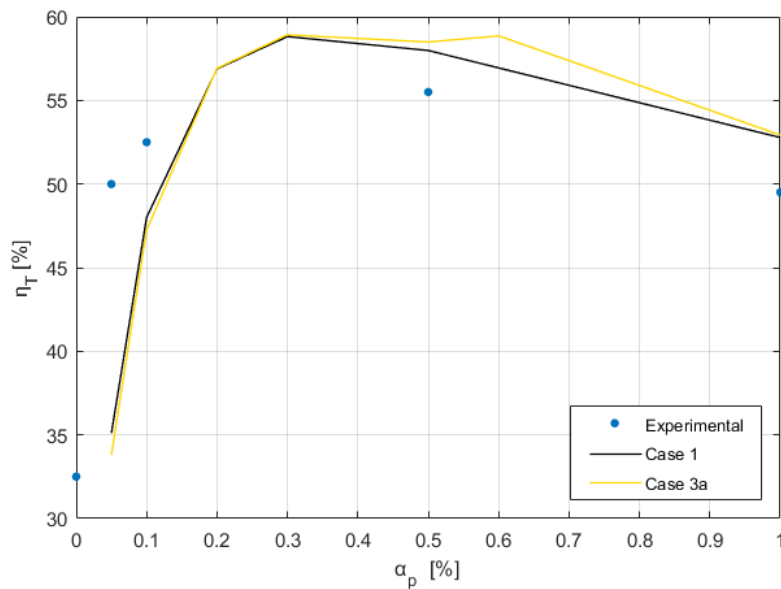

Figure 6.8: Thermal efficiencies obtained before and after adding the Brownian force to the model, as a function of particle volume fraction.

possible to trace single-particle trajectories, but the vector scenes in STAR-CCM+ gives an overview of the particle behaviour.

The volume fraction scene in Figure 6.9a confirms that the Brownian motion contributes to homogeneous particle distribution. The results were obtained for $\alpha_p = 0.3\%$ The figure shows a part of the volume fraction distribution. In the rest of the collector, no changes in volume

fractions were observed. The velocity vectors in Figure 6.9b are shown to confirm the particle behaviour. Comparing the scenes displaying particle volume fraction with velocity vectors shows that when there is an area containing high particle concentration, the velocity of the particles in this area also has a significant increase. Because of the low particle concentration, the particles are subjected to violent Brownian motion.

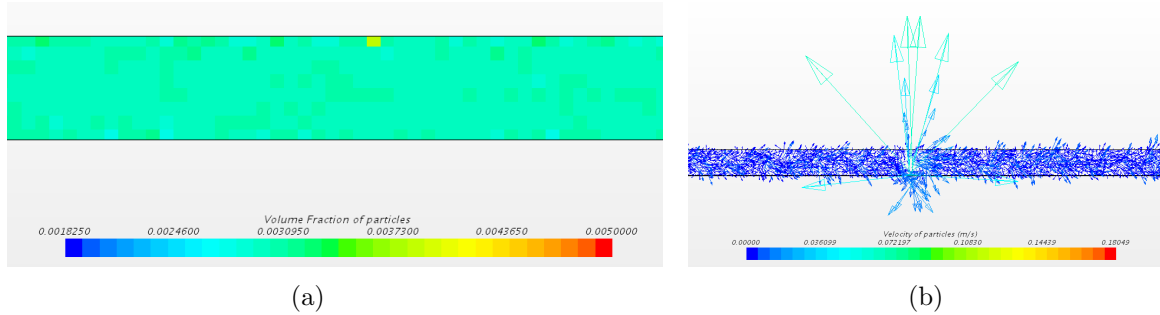(a)   (b)

Figure 6.9: Output values from STAR-CCM+ showing: a) particle distribution and b) velocity vectors.

The simulations in this section also investigated the outlet temperature and particle deposition efficiency. Figure 6.10a shows the results of the outlet temperature. The outlet temperature when the Brownian force is included is very similar to the Case 1 simulations. What is interesting in this figure is that the values for $\alpha_p < 0.2\%$ are very similar to the experimental values. When studying the thermal efficiency, there was a significant deviation from the experimental values for $\alpha_p = 0.05\%$.

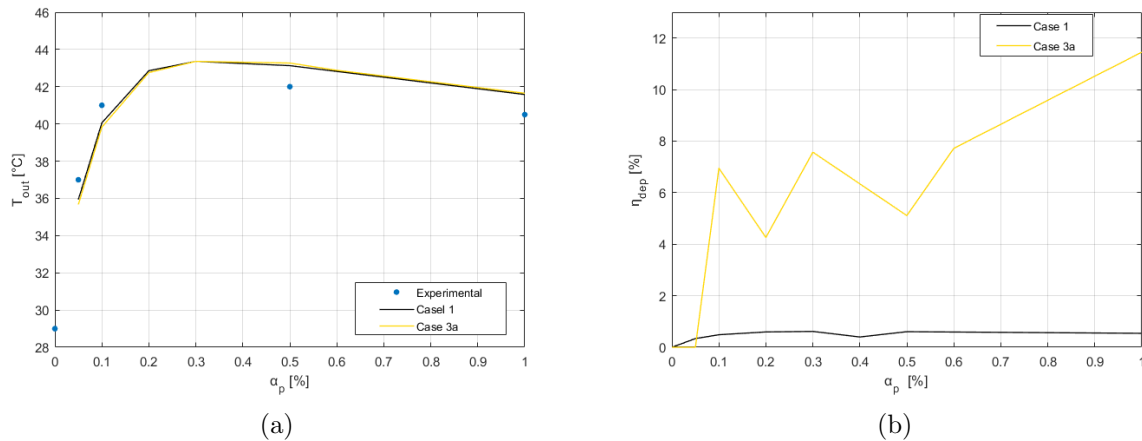(a)   (b)

Figure 6.10: Brownian force effects on: a) outlet temperature and b) nanoparticle deposition efficiency.

According to Yin et al. [84], the deposition efficiency increases with decreasing fluid temperature and has a minimal increase with changing particle size, when Brownian motion is present. From simulations, low particle concentrations, results in a low nanoparticle deposition efficiency. However, for higher particle concentrations, areas with a higher accumulation of nanoparticles are subjected to a more violent Brownian motion. It is thus giving the particle a higher probability of hitting the surface. Theoretical calculations shown in Figure 6.2 shows that the action of the Brownian force reduces with increasing outlet temperature. Thus, since the temperature reduces for volume fractions above 0.3%, Brownian force impacts increase and therefore the

deposition efficiency increases. This is shown in Figure 6.10b, where the yellow line represents the model with Brownian force (Case 3a), and the black line represents Case 1. The values have significant deviations, but there is an increase with increasing volume fraction of particles. Thus, the results from Figure 6.10b confirms the conclusions drawn by Yin et al. [84] that higher volume fractions leads to higher deposition efficiency. However, particle-wall and particle-particle collisions are not modelled here, so in reality it is possible that these collisions contribute to a better dispersion of the particles and the Brownian force promotes the collisions. Therefore, it is possible that the deposition efficiency would not be so high in reality.

6.3.3   Influence of the Retardation Factor

After evaluating the forces and how they affect the particles, the drag force was updated to account for both Cunningham's correction factor and retardation factor. The retardation factor was adopted from Rastegar et al. [61]. Their experiment showed that including the retardation factor in the drag force resulted in a lower deposition rate of particles. This decrease occurs because of the increased viscous resistance near the walls.

The equations for drag force including the retardation factor (described in section 4.2.1) show that closer to the walls, the drag force has a more significant impact on the particles. This seems unlikely since the velocity decreases near the walls. The drag force equation including the retardation factor (Eq. (4.11)) was studied theoretically, and considered to be inaccurate. Due to the slip-conditions at the top and bottom walls, the retardation factor should make the drag force lower close to the walls.

The results from the simulations are presented in Figure 6.11, where the yellow lines shows the results obtained using the model updated with Brownian force, the red line shows the results obtained using the model including the thermophoretic force, the black line shows the results obtained using the model without force effects (Case 1), and the blue dots represent the experimental values. The stapled lines shows the results obtained using the models excluding the retardation factor, while continuous lines represent the results from the model with the updated drag force. The same figure descriptions are used for Figure 6.12a and 6.12b. The updated drag force does not affect the thermal efficiency significantly. Including the retardation factor leads to lower efficiency for the thermphoretic model, but not for the Brownian model. For $\alpha_p \leq 0.3\%$, the results from the Brownian models have similar behaviour. It is when the volume fraction is higher than 0.5% that there occurs a significant deviation. There is also a significant deviation for Case 2b. This deviation indicates that high concentration results in lower thermal efficiencies. Most likely, this deviation comes from an error made in the model, because the efficiency for $\alpha_p = 1\%$ is much higher than expected and all other models has not shown deviating behaviour. The maximum efficiency obtained for the models with updated drag force is 59% and was obtained when using Case 3b.

Outlet temperature effects are shown in Figure 6.12a. Updating the drag force results in a more constant outlet temperature for the various volume fractions in the thermophoretic model. The deviation at $\alpha_p = 1\%$ also occurs here. For the Brownian model, the results are almost identical to the results obtained before updating the drag force to include the retardation factor. Figure 6.12b shows how the updated drag force affects the deposition efficiency in the collector. As shown, the deposition is higher after updating the drag force, which means that the relation is
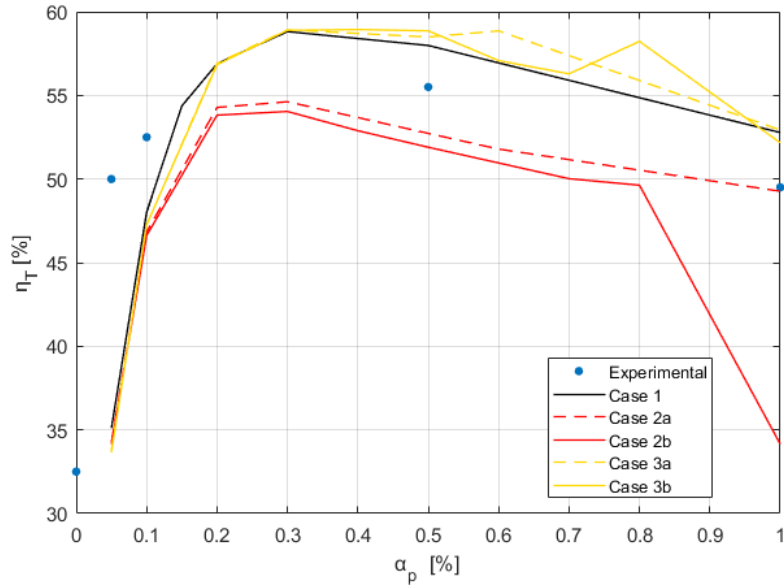
Figure 6.11: Thermal efficiencies obtained before and after updating the drag force, for both Brownian and thermophoretic model.

not precise. For comparison purposes Case 1 has been added, and as seen from the figure, it has no significant particle deposition. The updated drag force significantly increases the deposition efficiency for Case 2b. However, the Brownian model deposition seems to be random, so that it is difficult to draw conclusions. For the thermophoretic model, the updated drag force gives similar results as Case 2a. The only difference is that it slightly increases (and a larger increase for $\alpha_p = 1\%$).

This updated drag force does not influence the heat absorbed, q_V. The figures made to confirm this were identical to Figure 6.15, and therefore not included here.
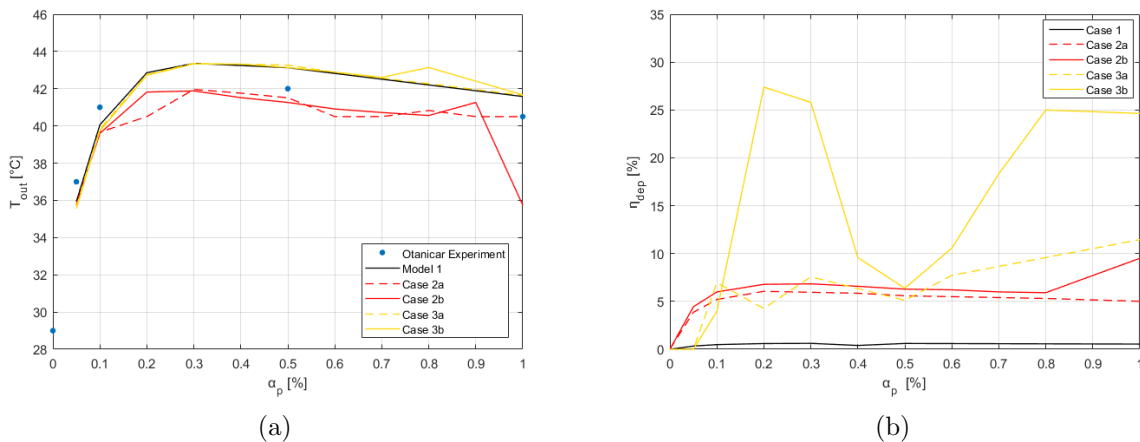

Figure 6.12: Drag force effects on: a) thermal efficiency and b) deposition efficiency.

To summarise, the updated drag force does not contribute to increasing efficiency. The effect

of the drag force was as expected from theoretical investigations, and a more precise analysis of the parameters should be done to optimise this drag force model. These models (2b and 3b) are not used for further investigation.

6.3.4 Influence of the Heat Transfer Coefficient

As mentioned previously, there have been few theoretical formulations of the heat transfer co-efficient in nanofluids. Therefore, the heat transfer coefficient in the model was initially set to a constant value of 34 W/m^{2}K. This value was obtained by Otanicar et al. [55], and was considered a maximum value when $\alpha_p = 1\%$. Thus, the assumption that h is constant is not accurate. As mentioned in section 5.5, the heat transfer coefficient changes with particle concentration and a linear regression was done to obtain a correct h for each particle concentration. For this section, h was updated in the models (2c and 3c) for each particle concentration, so that this coefficient varies between $\in [23, 34]$. The equation obtained from the linear regression showed in section 5.5 was used to obtain the correct h for each volume fraction. The results showing the influence of h is shown in Figure 6.13. Here, the black line shows the results obtained using Case 1, the blue dots represent the experimental values, red lines shows the results obtained using the thermophoretic models, and the yellow line shows the results obtained using the Brownian models. The stapled lines are results from models with constant h and continuous lines are results from models where h is updated with the experimental values. It is clear that updating the heat transfer coefficient had a significant impact on the results for both the thermophoretic and Brownian models. These impacts resulted in a much higher efficiency for low particle concentrations.
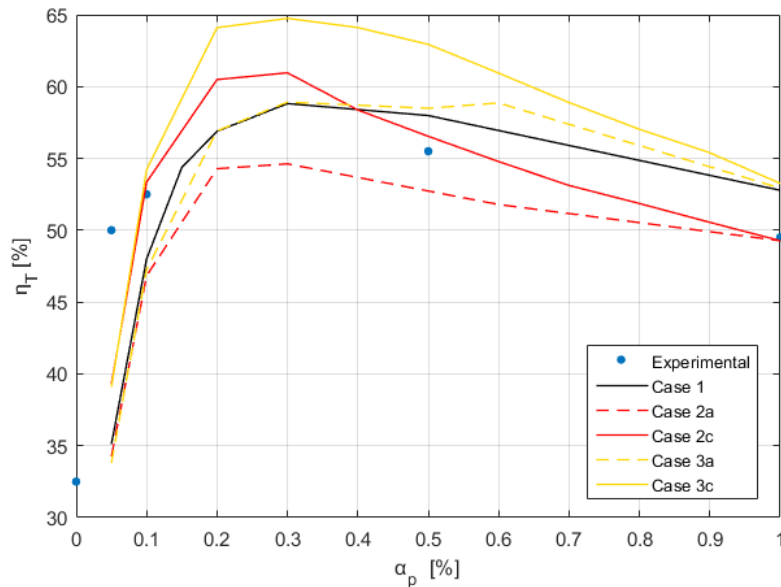

Figure 6.13: Thermal efficiencies obtained before and after updating the heat transfer coefficient, for both Brownian and thermophoretic model.

For higher particle concentrations, the efficiency corresponds to the experimental results from Otanicar [55]. The largest deviation from the models with constant h occurs when $\alpha_p = 0.05\%$,
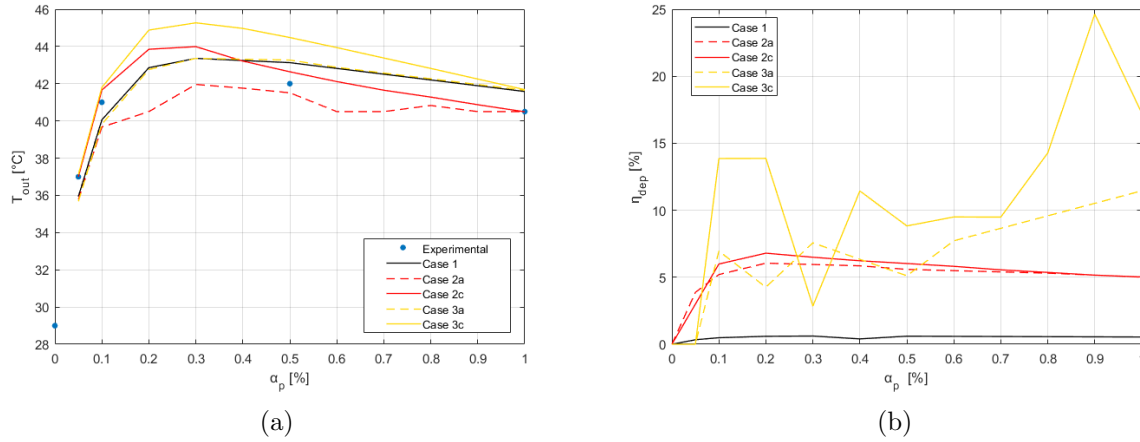
Figure 6.14: Heat transfer coefficient effects on: a) outlet temperature and b) deposition efficiency.

and has maximum value at 16%. The peak efficiency for Brownian model, with updated h, occurs at $\alpha_p = 0.3\%$ and has a 10% increase from the model with constant h. For the thermophoretic model, the peak efficiency also occurs at $\alpha_p = 0.3\%$, here with an increase of 13% from the model with constant h. It is interesting to note that for the thermophoretic model with updated h (Case 2c), with volume fractions $\geq 0.5\%$, the model corresponds to the experimental curve. The fact that there is a lack of experimental testing of various volume fractions makes it challenging to compare the behaviour of the thermal efficiency when $\alpha_p \in [0.1, 0.5]\%$.

Figure 6.14a shows that the heat transfer coefficient also has a significant impact on the outlet temperature. The thermophoretic model has a maximum increase of 5% in outlet temperature when h is updated. The Brownian model has a maximum increase of 4% after updating h. It makes sense that updating the heat transfer coefficient gives better collector performance since it provides a correct model for heat transfer through the nanofluid. The deposition efficiency is displayed in Figure 6.14b. The updated h does not have a considerable effect on the thermophoretic model results. For the Brownian models, it has a significant effect on the results. Here, the deposition efficiency increases considerably, and has large deviations. The result obtained here is similar to the results obtained for Brownian deposition in the previous subsection; it is challenging to draw trends from these values.

This updated heat transfer coefficient does not influence the heat absorbed, q_V. The figures made to confirm this was almost identical to Figure 6.15, and therefore not included here.

6.3.5   Influence of the Particle Concentration

The particle concentration influences the heat absorption. When the nanofluid has a higher nanoparticle concentration, the transmitted light intensity into the nanofluid is higher, but the light also attenuates faster. Thus, the absorption capacity has limitations. It has been shown that for high-concentration nanofluids, the light would be absorbed by a thin top layer [73]. This is confirmed from the results in Figure 6.15, that shows the heat absorbed as a function of distance from the collector bottom. This figure also shows that there is a significant difference between lower and higher particle concentrations. When the volume fraction is low, the heat

absorbed does not significantly differ between the amount of heat absorbed at the top versus the bottom. For higher volume fractions, there is a large amount of heat absorbed at the top, while the heat absorbed at the bottom is approaches zero. Thus, it can be confirmed that a top layer of nanoparticles absorbs most of the heat, while there is little heat absorption at the bottom. Figure 6.15 shows that the heat absorbed from the model including Brownian motion has higher values than for the model including thermophoresis. This can be explained by the fact that the Brownian model results in a more homogeneous particle distribution.
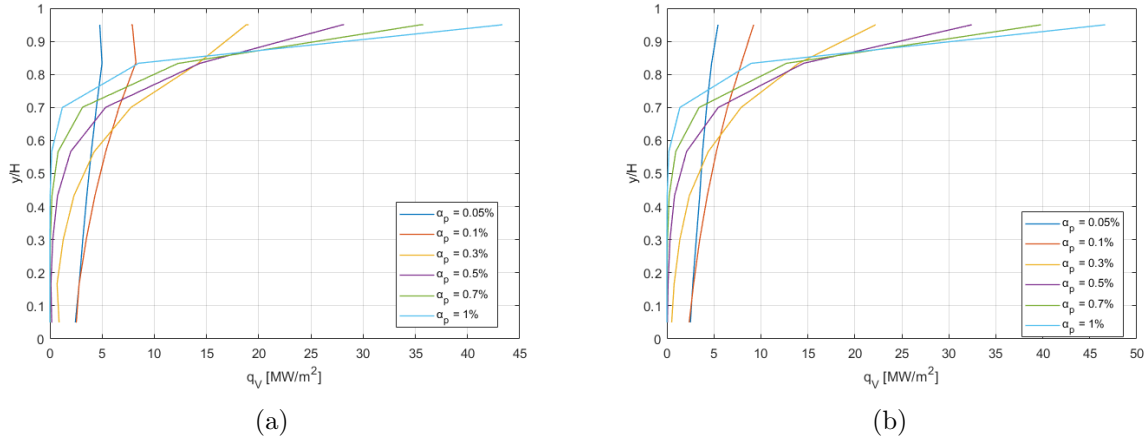

Figure 6.15: Heat absorption from models including a) thermophoresis (Case 2a) and b) Brownian motion (Case 3a), as a function of the distance from collector bottom at various volume fractions.

The results in Figure 6.5, 6.13, 6.11 and 6.13 shows that increasing the amount of nanoparticles, the efficiency increases for volume fractions of up to 0.3%. When increasing the number of nanoparticles further, most of the radiant heat absorbs at the top surface of the collector, increasing the temperature of the top boundary. This enhances the thermal leak to the surroundings and the thermal efficiency of the collector reduces again. The largest deviation from the experiment is observed close to the maximum of the function. This inaccuracy is addressed to the approximation done for the extinction coefficient and the experimental uncertainty in the determination of thermal leaks.

For the results presented in Figure 6.13, the maximum thermal efficiency reaches 65%, and this occurs when the Brownian model was considered, and the heat transfer coefficient was updated. The maximum outlet temperature was obtained when $\alpha_p = 0.3\%$, and was equal to $45\,^{\circ}\text{C}$, also for the Brownian model. For the microsized collector, the temperature was equal at the top and bottom of the collector, see the temperature distribution in Figure 6.3. Both the efficiency and outlet temperature reach maximum values when $\alpha_p = 0.3\%$. Before and after this, the efficiency and outlet temperature is lower. This result is supported by literature [34].

The investigated forces are highly dependent on particle concentration. Both Brownian and thermophoretic forces affect particles in the flow, and the higher particle concentration leads to a higher force magnitude in the computational cell. This can be confirmed by Eq. (4.16) (Brownian force) and (4.17) (thermophoresis). Both these equations involve the number density, which depends on the particle concentration. These forces affect the flow, but as discussed earlier, as long as the fluid drag is significantly higher than the forces affecting the particles, the flow is not dominated by these forces. Comparing the particle distributions are for each case,

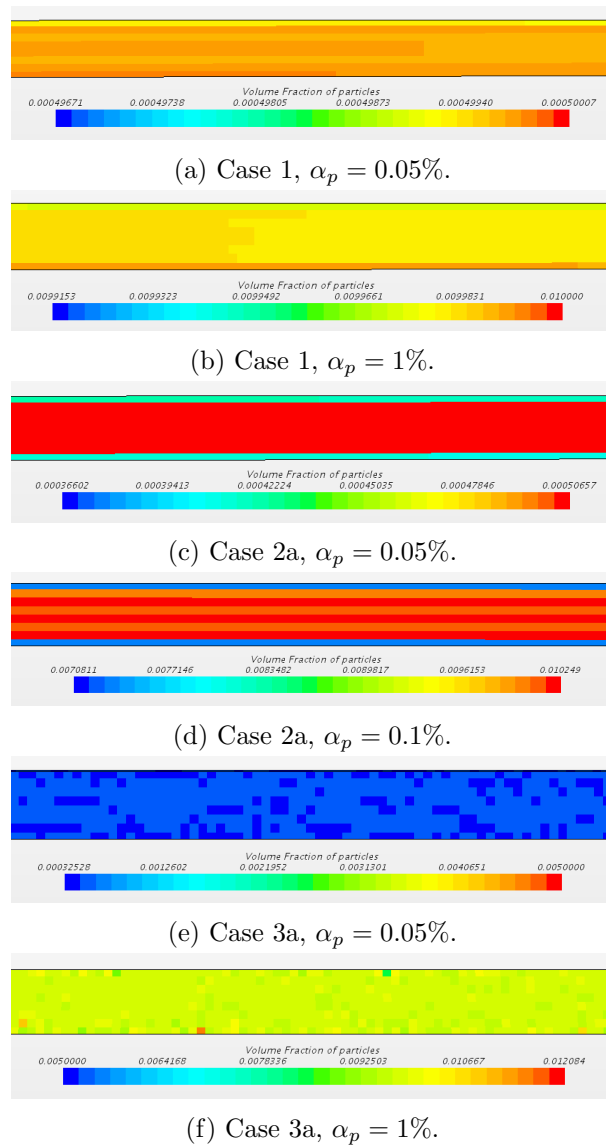the volume fraction distributions from STAR-CCM+ are shown in Figure 6.16.

(a) Case 1, $\alpha_p = 0.05\%$.

(b) Case 1, $\alpha_p = 1\%$.

(c) Case 2a, $\alpha_p = 0.05\%$.

(d) Case 2a, $\alpha_p = 0.1\%$.

(e) Case 3a, $\alpha_p = 0.05\%$.

(f) Case 3a, $\alpha_p = 1\%$.

Figure 6.16: Particle distribution in three different models with $\alpha_p = 0.05\%$ and $\alpha_p = 1\%$, in the middle of the collector.

Figure 6.16 shows that there are some differences in the particle distribution when the model is subjected to the different forces, and various particle concentrations. Figures 6.16a and 6.16b, refer to Case 1 (with no momentum source), that is, only gravity and drag affecting the particles. Through the geometry, the volume fraction decreases and is higher at the inlet than the outlet. There is a small deposition layer at the collector's bottom, which is expected from this type of flow. Figure 6.16a shows lower volume fraction and more homogeneous distribution than Figure 6.16b. Figure 6.16c and 6.16d show the flow after including the Brownian force, Case 3a. This model results in the most homogeneous particle distribution. There are a few "pockets" where the particle concentration is higher, this mainly occurs for the higher particle concentration. For the lower particle concentration, the distribution is homogeneous. Figure 6.16d and 6.16e show

how the thermophoretic force affects the particle distribution. Therefore the distribution is less homogeneous in Case 2a than for other models. This occurs because the thermophoretic force reduces the effect of gravity and moves the particles to the middle of the collector. The higher particle concentration has a less homogeneous distribution. A more homogeneous distribution gives the most effective heat absorption.

Figure 6.17 demonstrates profiles of the nanoparticle concentration at different axial positions of the collector. The figure displays both the model including themophoresis and Brownian motion, with updated heat transfer coefficient (Cases 2c and 3c). It follows from the figure that the nanoparticles are not uniformly distributed in the cross-section; the profiles are asymmetrical. Figure 6.17a shows has more smooth lines than Figure 6.17b, and has more visible trends. However, Figure 6.17a also have asymmetrical profiles. This is explained by the mutual action of gravity and thermophoresis drifting the particles towards the bottom boundary. The asymmetry increases closer to the outlet from the collector.
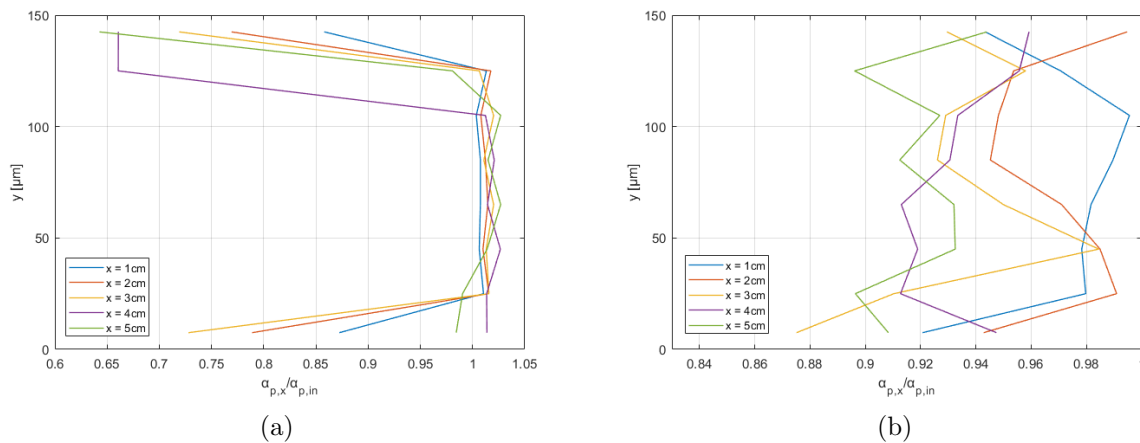

Figure 6.17: Transverse distribution of particle concentration, scaled with the inlet value for: a) thermophoresis (Case 2c) and b) Brownian motion (Case 3c), at different axial coordinates of the collector. Volume fraction of particles is 0.3%.

As shown in Figure 6.17a, the volume fraction is higher at the bottom of the collector, and very low at the top. This same pattern can be seen from Figure 6.16c and 6.16d. For the model including Brownian motion, the volume fraction is more random, and it is challenging to spot a trend here. However, there is a lower volume fraction at the end of the collector. The volume fraction decreases with larger x. This is a result that is difficult to spot in Figure 6.16e and 6.16f.

6.3.6   Comparison

After evaluating both the Brownian and the thermophoretic forces, the drag force and the heat transfer coefficient it is necessary to make a comparison of the numerical models.

The Brownian force and thermophoretic forces are similar in the way that they increase the thermal efficiency significantly compared to Case 1 and the experimental values. The fact that there is such a significant deviation from the experimental results can be easily addressed to

the approximation done for the extinction coefficient and the experimental uncertainty in the determination of thermal leaks. Also, as mentioned earlier, Otanicar et al. [55] have no results for $\alpha_p \in [0.1, 0.5]\%$, which means that it is impossible to validate the numerical results for these volume fractions.

There are many similarities between the Brownian force and thermophoresis. They are both dependent on temperature, particle size and fluid medium. Both of the forces also increased the thermal efficiency of the collector investigated. Because of these similarity it is necessary to discuss whether these forces do not describe the same phenomena. The main difference is the temperature dependency. Thermophoresis occurs as a result of the temperature gradient, while the Brownian force only gets an increased effect due to temperature changes. Also, thermophoresis increases with increasing temperature, while Brownian force decreases with increasing temperature. This was shown in Figure 6.2, and is supported by research [17, 18, 84]. Additionally, the Brownian force contributes to a more homogeneous particle distribution, and thermophoresis does not.

Figure 6.18 shows how the results from all numerical models investigated deviate from the experimental values. It shows both efficiency and temperature differences. In Figure 6.18a, there is a stapled black line representing the 5% error limit for the experimental results. There is a large deviation in the numerical against experimental values for $\alpha_p = 0.05\%$, for all models. This is a result of inaccuracy in the computation of the volumetric absorption for the low particle concentration. Additionally, the figure shows that the model including thermophoresis with an updated heat-transfer coefficient (Case 2c), has the smallest deviation from the experimental values. The error is less than 5% for $\alpha_p > 0.05\%$. Thus, it is chosen as the model with the highest similarity to experimental results and is chosen for further investigation. Comparing these results with Figure 6.18b, the same model has the smallest deviation in temperature. Figure 6.18b also shows better results for $\alpha_p = 0.05\%$.
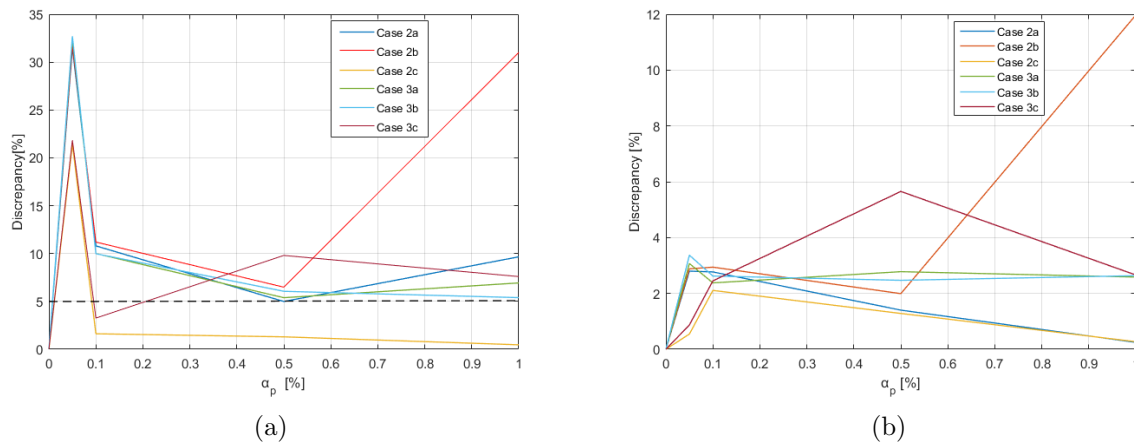

Figure 6.18: Deviations from the experimental values for: a) thermal efficiency and b) outlet temperature.

Comparing the deposition efficiencies shows that the Brownian force results in a significantly higher deposition efficiency than the thermophoretic force. These results are presented in Figures 6.6b, 6.10b, 6.12b and 6.14b. The maximum for the Brownian model is 27%, while the maximum for the thermophoretic model is 9.5%. The Brownian models show deviating behaviour, and it is difficult to draw conclusions or trends from these results. The thermophoretic models do not

lead to deviating results. Here, the higher volume fractions result in lower deposition efficiency, except for the drag force model. Nevertheless, this is a large deviation, so that a numerical inaccuracy might be the cause.

The optimal model for investigating the nanofluid DASC is the thermophoretic model with updated heat transfer coefficient (Case 3c), with volume fraction of particles of 0.3%. This model yields a maximum efficiency of 62%. Due to the low concentration and size of the particles the phases are weakly coupled and concentration profiles do not affect the symmetry of the velocity and the temperature patterns, the temperature increases linearly from the inlet towards the outlet of the collector.

6.4   Parametric Analysis

A base case simulation was developed, that results in a qualitatively similar evolution of thermal efficiency, an optimal absorption of radiant heat and low discrepancy from experiments. In this section, this base case was used in a parametric analysis in order to optimise the performance of the collector.

6.4.1   Influence of the Collector Height

An important model specification when optimising the efficiency is the size of the collector. The height of the solar collector has vital influence on the amount of heat absorbed and transferred by the nanofluid. Gorji and Ranjbar [23] studied how geometry affects the temperature distribution and efficiency in a flat-plate DASC. However, their tests consisted of larger geometries, where there was no temperature gradient on the bottom plate, which makes their results different from the results expected in this thesis. However, they concluded that there is an optimum height/length ratio associated with the best thermal performance of the collector. As mentioned in chapter 5, one of the reasons for choosing the micro-geometry was to have a nonzero amount of energy expected to reach the bottom. Sharaf et al. [68] performed tests on a microscale collector, identical to the geometry used by Otanicar et al. [55]. They discovered some interesting aspects of how collector height influences efficiency.

In this section, various heights for the collector were tested to evaluate how the thermal efficiency changes. Both lower and higher collectors were simulated. The results of the model-based optimisation are presented in Figure 6.19, where the thermal efficiency and the outlet temperature are shown for various heights of the collector and types of the bottom boundary.

As seen in Figure 6.19, when increasing the thickness, more heat is taken by the flow of the nanofluid and the temperature decreases. The outlet temperature decreases almost linearly with collector height. This limits the thermal losses and the collector efficiency increases. The observed dependence of the thermal efficiency on the height of the volumetric receiver is consistent with the results obtained by [68]. However, at a thickness of 300 μm, the efficiency begin to decrease as the volumetric absorption is no longer active across the entire volume of nanofluid. The consumed heat, therefore, leaks to internal layers with the incipient volumetric absorption, which reduces the thermal efficiency. In a more detailed investigation, the collector heights were
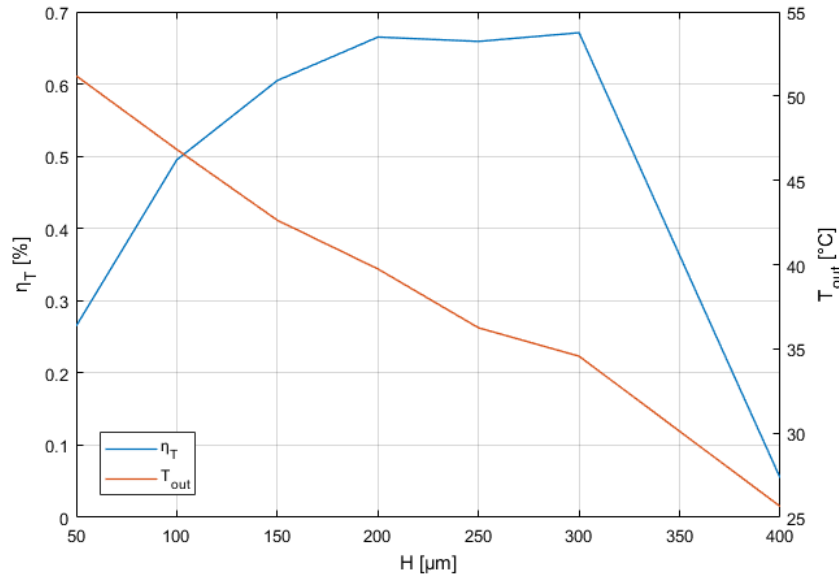
Figure 6.19: Thermal efficiency and outlet temperature as a function of collector height. The blue line represents thermal efficiency, read from the left y-axis, and the orange line represents the temperature, read from the right y-axis.

tested for various volume fractions. These results are illustrated in Figure 6.20. This figure shows thermal efficiency as a function of volume fractions and for various collector heights.
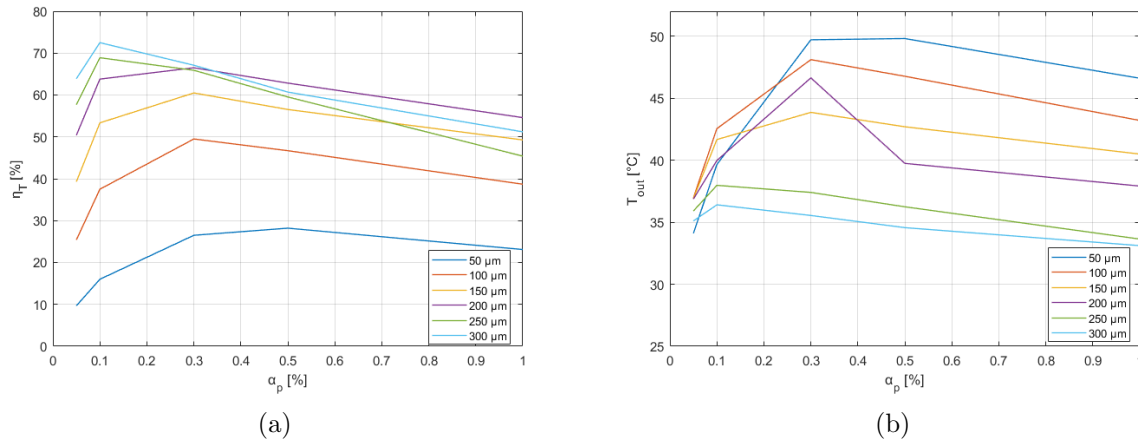

(a)

(b)

Figure 6.20: Collector height effects on: a) thermal efficiency and b) temperature as a function of volume fraction.

Figure 6.20a shows that the peak efficiency occurs at lower volume fractions when the height is increased above 200 μm. After reaching the peak values, the efficiency decreases for higher volume fractions. At $\alpha_p \leq 0.3\%$ larger heights do not lead to a higher efficiency. At higher volume fractions, a higher collector gives more room for thermal energy transfer and losses to the surroundings. Also, for high volume fractions, the solar radiation is absorbed by a top thin layer [73], which makes the efficiency less dependent on the collector height. However, when the main absorption happens by the thin top layer, there is less conduction of heat down to the rest

of the collector, resulting in an inefficient heating process. For higher collector heights the peak efficiency occurs at lower volume fractions. This might occur because of the increased optical path and homogeneous distribution of particles. Figure 6.20b shows the temperature, which is generally higher for lower collector heights.

The heat absorbed by the nanofluid changes with collector height. The results are illustrated in Figure 6.21. Here, the heights have been converted to dimensionless heights. The figure shows that lower collector heights have more uniform heat absorption through the collector, while the larger heights have zero heat absorption near the bottom wall. For collector heights above 200 m, there is zero heat absorbed at the bottom. Comparing these results to the results in Figure 6.19 shows that the collector with $H = 200$m is optimal, because it has high thermal efficiency, in addition there is heat absorbed near the bottom wall.
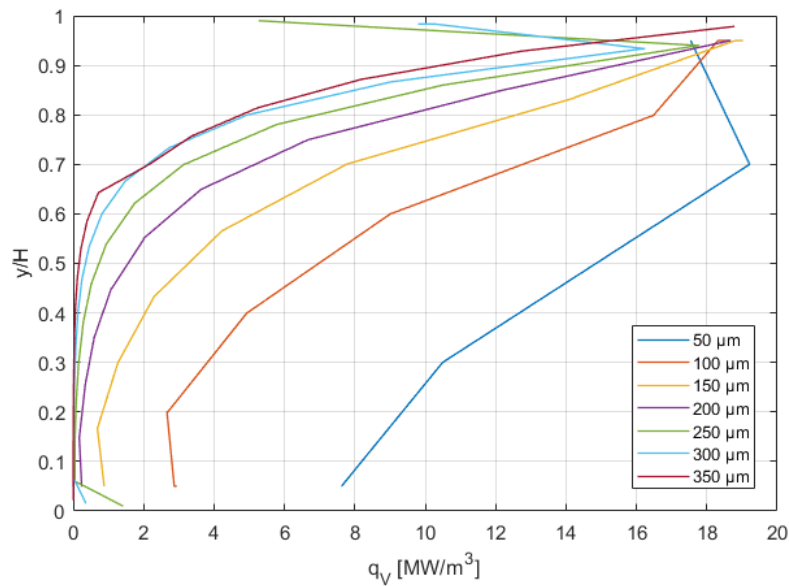

Figure 6.21: Heat absorbed by the nanofluid as a function of dimensionless collector height.

In this research, the deposition efficiency was also tested. Figure 6.27a shows the results from these simulations for various collector sizes and types of the boundary condition. As seen in the figure, the highest deposition efficiency was 11% at the lowest size of the gap. Furthermore, increasing the size, the deposition efficiency reduces. This is explained by the destabilising action of the thermophoretic force which deposits more particles in a narrow gap while the disperse action of drag becomes stronger for a wider collector. Moreover, the temperature reduces with the height of the collector, weakening the thermophoresis effect.
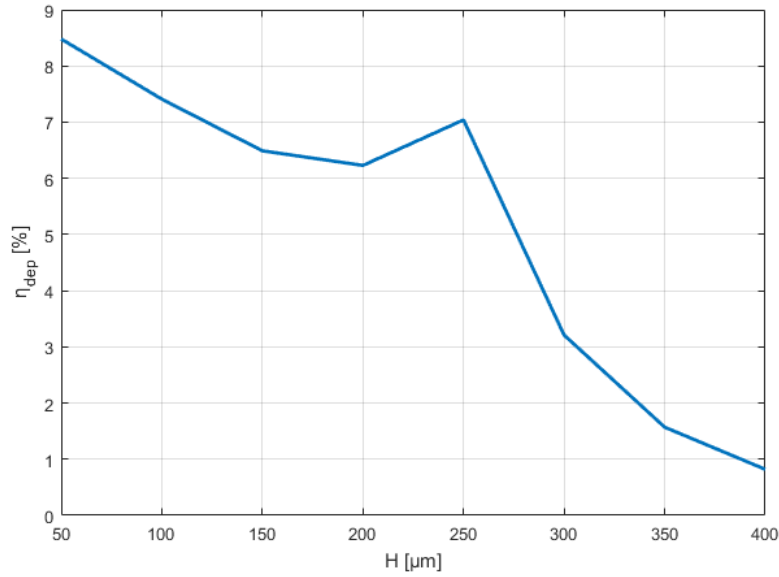
Figure 6.22: Deposition efficiency as a function of collector height.

6.4.2   Influence of the Nanofluid Velocity

Nanofluid velocity through the collector has an impact on thermal efficiency. According to Eq. (6.1), thermal efficiency depends on the mass flow through the collector. Following this equation leads to increased efficiency with increasing nanofluid velocity. Furthermore, it is important to note that there occurs a pumping cost penalty growing with the flow velocity. To account for this effect, a total efficiency of the process is defined:

$$\eta = \eta_T - \frac{Q\Delta P}{q_0 A},\tag{6.3}$$

where Q is the volumetric flow, ΔP is the friction pressure drop in the collector, and A is the irradiated area of the collector. Another factor that needs to be accounted for is the turbulence that occurs in the collector when the flow reaches a particular value. Turbulence is related to the Reynolds number for the nanofluid flow and was calculated. For $u > 4.6$ cm/s, the Reynolds number reaches the transient zone, and turbulence occurs.

To calculate the turbulent stress in Eq. (4.2), the CFD model was updated with RANS and the $K - \epsilon$ model. How the total efficiency changes with the mass flow is illustrated in Figure 6.23, where the blue line represents the efficiency and is read from left y-axis, and the orange line represents the pressure drop and is read from the right y-axis.

The results from Figure 6.23 shows that a peak efficiency of 87% is obtained at $u = 3$ cm/s. This efficiency is 42% higher than the maximum efficiency of the base case model (Case 3c), and 30% higher than the maximum efficiency obtained when changing collector height. This significant increase is directly related to the fact that efficiency is proportional to fluid velocity.

In addition to evaluating the efficiency, it is also relevant to evaluate the pressure drop through
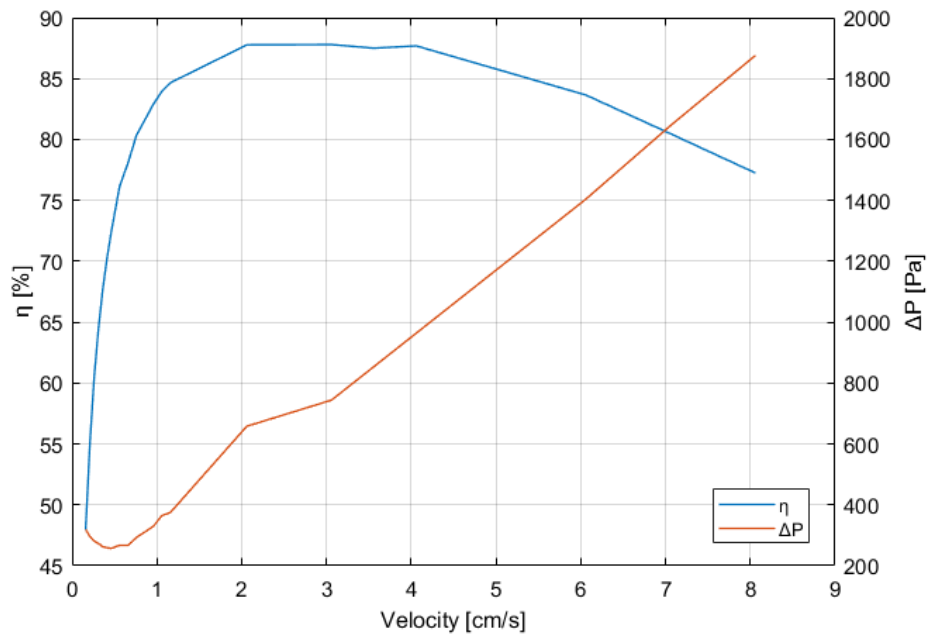
Figure 6.23: Thermal efficiency and pressure loss as a function of nanofluid velocity.

the collector. As shown in Figure 6.23, the pressure drop increases significantly with increasing velocity. It is important that the pressure drop does not get too high.

The results for deposition efficiency and outlet temperature are shown in Figure 6.24. Higher velocity leads to less heat absorbed by the nanofluid. This occurs because the particles have less time to absorb the radiation from the Sun before moving beyond the collector. The deposition efficiency decreases as the velocity increases. Figure 6.24b shows that the deposition efficiency reduces asymptotically to 0.8% with the mean flow velocity due to a better distribution of the dispersed phase.
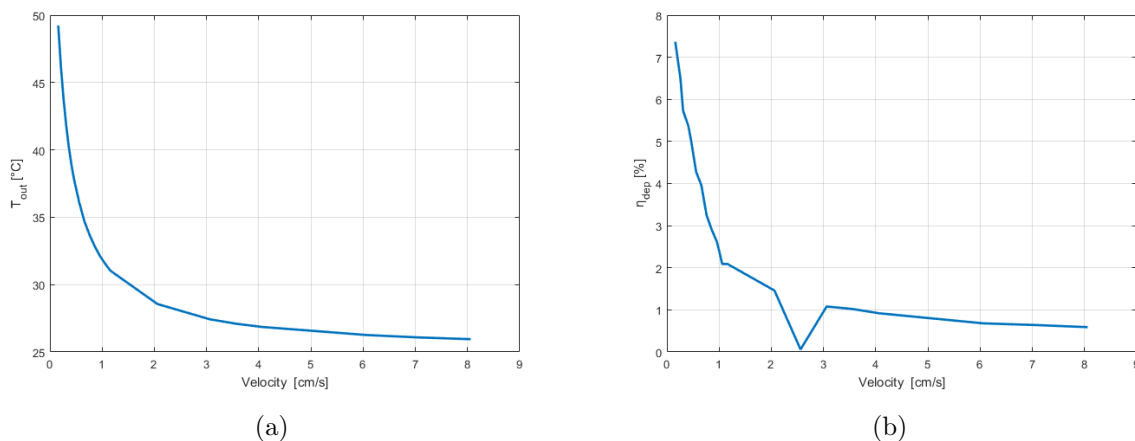

Figure 6.24: Velocity effects on: a) temperature and b) deposition efficiency.

Higher velocity results in better collector performance, until a maximum velocity of 3 cm/s.

The efficiency begin to decrease when velocity is 4 cm/s, and the pressure drop, resulting in a pumping penalty, increases.

6.4.3   Influence of Black Surface Absorbers

Otanicar et al. [55] performed a test where the bottom copper plate was painted black to imitate an absorbing blackbody. This resulted in increased collector efficiency. Later, Sharaf et al. [68] researched the optical behaviour of the bottom surface, and how an absorbing bottom influences the efficiency at various volume fractions.

In this study, simulations of black absorbing surfaces were primarily done with only the continuous phase present. The purpose of these simulations was to investigate the difference between volumetric absorption and black surface absorption. The volumetric absorption results were obtained from the model including thermophoresis with updated heat transfer coefficient at $\alpha_p = 0.3\%$. For the surface absorption, two models were made; one with the top plate as a black absorbing body, and one with the bottom plate as the black absorbing body. For the top plate, convection occurs in the same direction as in the previous results. The sunlight is first absorbed by the fluid, then absorbed by the bottom plate. All simulations in this section are modelled with fluid velocity of 0.26 cm/s and $H = 300\mu m$.

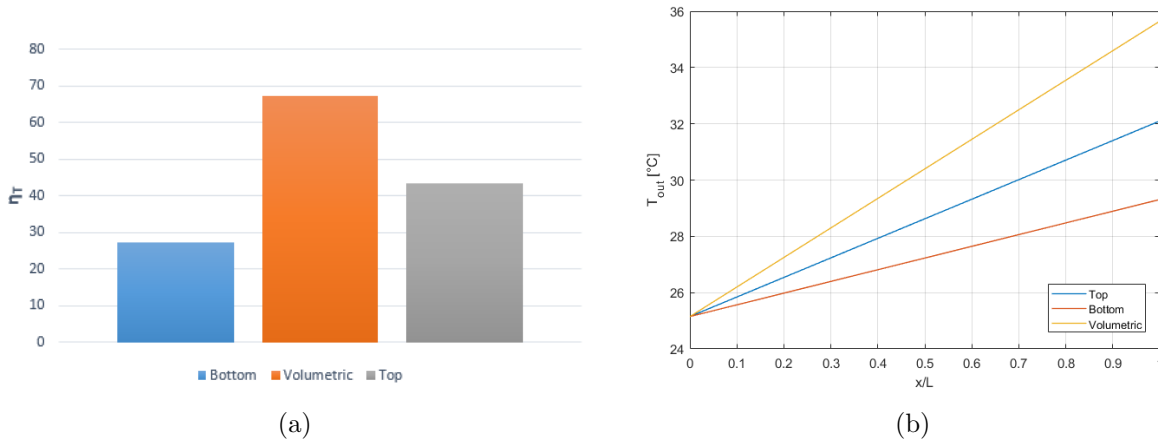(a)   (b)

Figure 6.25: Results from testing surface absorbers for: a) thermal efficiency and b) temperature for the different cases. Temperature profiles are plotted for the dimensionless position x/L.

Figure 6.25 shows that the bottom plate absorber has the highest efficiency, even higher than the volumetric absorber. This result is unexpected because most previous research indicates that volumetric absorption is the most effective choice. However, it is necessary to specify that this simulation was run without accounting for radiation losses, which normally occurs in such a collector. Since the efficiency has such high value, it is interesting to investigate this plate collector further. Sharaf et al. [68] concluded that a collector with a fully-absorptive bottom surface outperforms other alternatives due to the complete absorption of any radiation that reaches the bottom plate of the collector. The model was developed further to include nanoparticles with $\alpha_p = 0.3\%$. The nanoparticles primarily absorb the radiation, but the black bottom plate absorbs the radiation not absorbed by the nanoparticles. Heat flux to the bottom is changed to include this effect (see section 5.3.2). After testing the nanofluid with the bottom

black plate, various collector heights were tested. Figure 6.26 shows the results from these
simulations. The blue lines represent the thermal efficiency, read from left y-axis, and orange
lines represent outlet temperature, read from the right y-axis. The continuous lines represent
results from the model with the black absorbing bottom plate, and the stapled lines represents
results from simulations with the adiabatic bottom plate, also investigated in section 6.5.
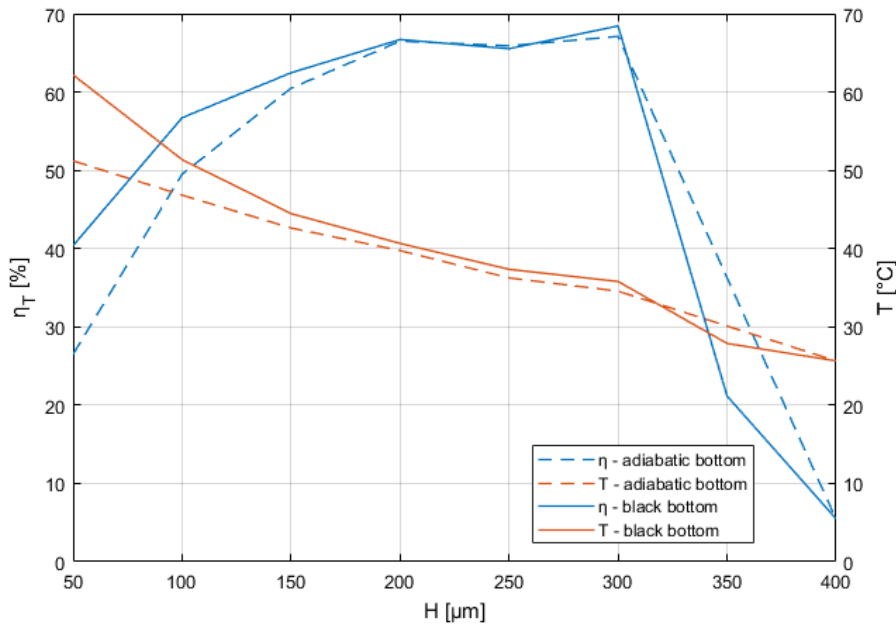

Figure 6.26: Efficiency and outlet temperature as a function of collector height for both adiabatic and black
bottom plate.

Figure 6.26 shows that for collector heights lower than 200μm, the efficiency is higher for the
model with the black absorbing bottom plate. In this case, a warmer bottom surface returns
absorbed heat back into the process, boosts the thermal efficiency, and increases the outlet
temperature. At the point of maximum difference, the efficiency is 52% higher for the black
bottom plate, than for the adiabatic plate. This occurs at the lowest collector height tested,
50μm. For collector heights above 200μm, the thermal efficiency decays towards the values for
the case with the adiabatic bottom. This can be explained by the fact that increasing the gap,
the nanofluid consumes most of the thermal radiation in the bulk and the bottom does not receive
sufficient heat. The same results occur for outlet temperature. Lower collector heights results in
a more significant temperature deviation from the adiabatic bottom. When the collector height
is above 150μm, the temperature deviation is less than 5%. At the maximum deviation, the
black bottom plate collector has an outlet temperature 21% higher than the adiabatic bottom
plate collector. These results indicate that the black absorbing bottom plate is optimal when
the plate thickness is lower than 200μm. However, for collector heights higher than this, the
deviation is insignificant or negative.

It is well-established in the literature that DASCs with thicker nanofluid films generally exhibit
higher collector efficiencies [68]. Indeed, there is a lower efficiency for the collector with lower
heights. However, the physical explanation for this is that the efficiency is highly dependent on
the bottom surface type. For collectors with a black absorbing bottom surface, the reason for

low efficiency at low collector heights is the increased thermal losses from the top surface due
to the higher top-layer temperature.

Figure 6.27 shows the deposition efficiency, for both black bottom and adiabatic bottom. In-
creasing the collector height, the deposition efficiency reduces. As mentioned previously, this is
explained by the destabilising action of the thermophoretic force which deposits more particles in
a narrow gap while the disperse action of drag becomes stronger for a wider collector. Moreover,
the temperature reduces with the height of the collector, weakening the effect of thermophoresis.
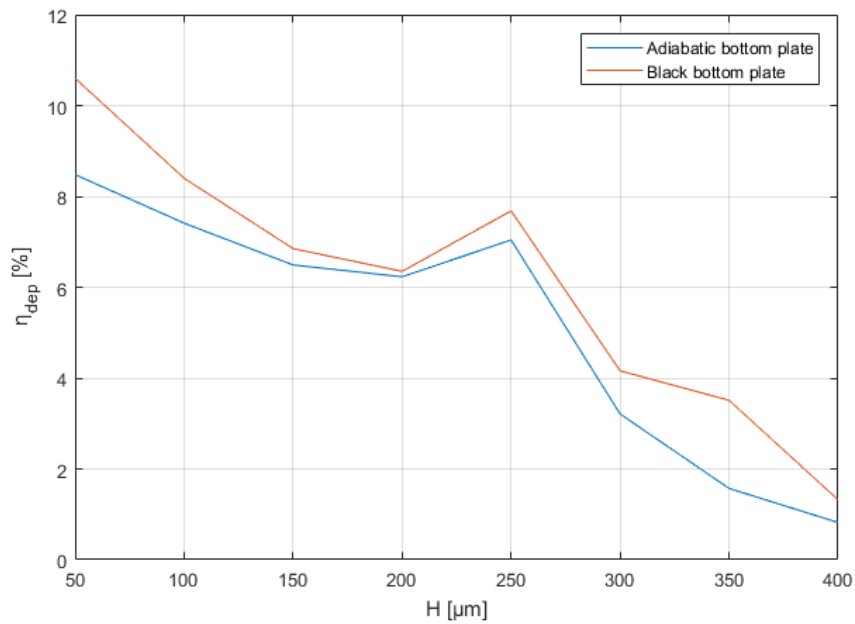For the model with a black absorptive surface, the deposition efficiency is higher.

Figure 6.27: Deposition efficiency as a function of collector height for black bottom and adiabatic bottom.

Chapter 7

Conclusion

An Eulerian-Eulerian two-phase model was developed to simulate the flow of carbon-based aqueous nanofluid in the direct absorption solar collector. The model is capable of simulating thermophoresis and Brownian motion, and reproduces optics of the sunlight absorption in the nanofluid. The models were validated against the experimental data and further used for developing an optimal model for describing the nanofluid DASC. After obtaining this optimal model it was used as a base case for a parametric optimisation of the collector. The parameters considered were the concentration of the nanoparticles, the geometry of the collector, the flow rate and the optical properties of the boundaries.

Theoretical prediction of the particle movement showed that the Brownian motion would contribute to a more homogeneous particle distribution, while the thermophoretic force would do the opposite. The drag force was also evaluated. Its value was much higher than both the Brownian force and thermophoretic force, so these two forces would not disturb the flow significantly. Validation of the model against the experimental results showed that the accuracy of the model was satisfactory.

Investigating the forces separately showed that the Brownian force has a significant effect on the particles, but it is random and has a deviating behaviour. The Brownian force leads to a homogeneous particle distribution. In areas with higher particle concentration, the force would move the particles away from the high concentration areas. Enhancements in efficiency were observed when testing various particle concentrations. The thermophoretic force did not result in a homogeneous distribution, but the results were in better agreement with experiments. The thermophoretic model with updated heat transfer coefficient was used as a base case model for the parametric analysis. The maximum efficiency were achieved for volume fraction of particles at 0.3%.

Adjusting the height of the collector had an impact on the thermal efficiency. Heights below 150μm gave low thermal efficiencies, and high outlet temperature. For collector heights above 150μm, the efficiency increased, but outlet temperature decreased. The highest efficiency was obtained for $H = 300\mu$m. Deposition efficiency increased for lower collector heights.

Nanofluid velocity through the collector also had a significant impact on thermal efficiency. Turbulence occurred for velocities above 4.6 cm/s. Maximum efficiency of 87% was obtained with flow velocity of 3 cm/s and decreased with higher velocities. Additionally, deposition

efficiency and outlet temperature decreased for higher velocities. The pressure loss through the collector increased significantly for higher velocities.

Lastly, black bottom surface absorbers were tested. A collector with a black bottom containing only water proved to be effective in the simulation. However, it was outperformed by volumetric absorption. The top surface black absorber was also tested and was not efficient as the volumetric absorption. This technology resembles a conventional flat-plate collector, as mentioned in the introduction. A black bottom collector containing nanofluid was also tested and increased the efficiency for low collector heights compared to the model with adiabatic bottom plate. The light-absorbing bottom boundary with nanofluid improved the thermal efficiency of the collector.

In conclusion, a pragmatic CFD model of the nanofluid-based DASC was proposed based on the E-E approach, which requires low computational power and therefore suitable for various particle concentrations and dimensions of the collector. Based on the simulations performed, the optimal volume fraction is 0.3%, and the optimal collector height is 300μm. Increasing nanofluid velocity also increases efficiency, but also has high pressure loss. For an increased effect at lower collector heights, a black absorbing bottom can be used.

Chapter 8

Future Work

Nanofluid technology has many opportunities for further work. This study has focused on microsized collectors, with relatively low velocity. The study has been performed in order to prepare an experimental study with this type of flat-plate direct absorption solar collector. An experimetal set-up with concentrated solar radiation should be tested. The various geometries and flow velocities should also be tested in experiments in order to validate these numerical results.

Convetionally, pumps have been used for driving the nanofluid through the collector, but it can also be interesting to investigate if a magnetic field can replace pumps in these experiments. Erosion from the usage of nanoparticles is also relevant for investigation.

Other studies can be related to enhance the performance of the model, including effects such as:

1. Particle material and different base fluids

2. Agglomeration of particles

3. Different particle geometries

4. Account for the viscosity of the nanofluid

5. Improvement of Brownian model

6. Particle size distribution, instead of uniform sized particles

7. Improvement of the model for the heat transfer coefficient

Bibliography

[1]   M. Abarham, P. Zamankhan, J.W. Hoard, D. Styles, S. Sluder, J.M.E. Storey, M.J. Lance, and D. Assanis. "CFD Analysis of Particle Transport in Axi-symmetric Tube Flows Under the Influence of Thermophoretic Force". In: *International Journal of Heat and Mass Transfer* 61 (2013), pp. 94–105.

[2]   N. Akram, R. Sadri, S.N. Kazi, M.N.M. Zubir, M. Ridha, W. Ahmed, M.E.M. Soudagar, and M. Arzpeyma. "A Comprehensive Review on Nanofluid Operated Solar Flat Plate Collectors". In: *Journal of Thermal Analysis and Calorimetry* (2019).

[3]   J.D. Anderson. *Computational Fluid Dynamics, The Basics with Applications.* McGraw-Hill Eduacation, 1995.

[4]   P. Atkins and J. de Paula. *Physical Chemestry.* Oxford University Press, 2014.

[5]   B.V. Balakin, O.V. Zhdaneev, A. Kosinka, and K.V. Kutsenko. "Direct Absorption Solar Collector with Magnetic Nanofluid: CFD Model and Parametric Analysis". In: *Elsevier Ltd* 136 (2018), pp. 23–32.

[6]   R. Bårdsgård, D.M. Kuzmenkov, P. Kosinski, and B.V. Balakin. "Eulerian CFD Model of direct Absorption Solar Collector with Nanofluid". In: *Unpublished* (2019).

[7]   L. Becker. "Getting Random Numbers in Every Cell". In: *Unpublished* (2018).

[8]   E. Bellos, Z. Sais, and C. Tzivanidis. "The use of Nanofluids in Solar Concentrating Technologies: A Comprehensive Review". In: *Journal of Cleaner Production* 196 (2018), pp. 84–99.

[9]   J.P. Bentley. *Principles of Measurement Systems.* Pearson Education Limited, 2005.

[10] H. Bhowmik and R. Amin. "Efficiency Improvement of Flat Plate Solar Collectors using Reflector". In: *Energy Reports* 3 (2017), pp. 119–123.

[11] R.E. Bird, R.L. Hulstrom, and L.J. Lewis. "Terrestrial Solar Spectral Sata Sets". In: *Solar Energy* 30.6 (1983), pp. 563–573. ISSN: 0038-092X.

[12] C.F. Bohren and D.R. Huffman. *Absorption and scattering of light by small particles.* Wiley, New York, 1983.

[13] J.R. Brock. "On the Theory of Thermal Forces Acting on Aerosol Particles". In: *Journal of Colloid Science* 17 (1962), pp. 768–780.

[14] J. Burelbach, M. Zupkauskas, R. Lamboll, Y. Lan, and E. Eiser. "Colloidal Motion Under the Action of a Thermophoretic Force". In: *The Journal of Chemical Physics* 147 (2017).

[15] Y.A. Cengel and M.A. Boles. *Thermodynamics - An Engineering Approach.* McGraw-Hill, 1994.

[16] C.T. Crowe, J.D. Schwartzkopf, M. Sommerfeld, and Y. Tsuji. *Multiphase Flows with Droplets and Particles.* CRC press, 2012.

[17] Y. Ding and D. Wen. "Particle Migration in a Flow of Nanoparticle Suspensions". In: *Powder Technology* 149 (2005), pp. 84–92.

[18]   S. Dong, L. Zheng, X. Zhang, S. Wu, and B. Shen. "A New Model for Brownian Force and the Application to Simulating Nanofluid Flow". In: *Springer-Verlag* (2013).

[19]   A.H. Elseikh, S.W. Sharshir, M.E. Mostafa, F.A. Essa, and M.K.A. Ali. "Applications of Nanofluids in Solar Energy: A Review of Recent Advances". In: *Renewable and Sustainable Energy Reviews* (2017).

[20]   Z. Fang, Y. Zhen, O. Neumann, A. Polman, J. G. de Abajo, P. Nordlander, and N.J. Halas. "Evolution of Light-Induced Vapor Generation at a Liquid-Immersed Metallic Nanoparticle". In: *NANO Letters* 13 (2013), pp. 1736–1742.

[21]   M.H. Fard, M.N. Esfahany, and M.R. Talaie. "Numerical Study of Convective Heat Transfer of Nanofluids in a Circular Tube Two-phase Model Versus Single Model". In: *International Communications in Heat and Mass Transfer* 37 (2010), pp. 91–97.

[22]   H. Ghasemi, G. Ni, A.M. Marconnet, J. Loomis, S. Yerci, N. Milijkovic, and G. Chen. "Solar Steam Generation by Heat Localization". In: *Nature Communications* (2014).

[23]   T.B. Gorji and A.A. Ranjbar. "Geometry Optimization of a Nanofluid-based Direct Absorption Solar Collector Using Response Surface Methodology". In: *Solar Energy* 122 (2015), pp. 314–325.

[24]   W. Graebel. *Advanced Fluid Mechanics*. Elsevier Science, 2007.

[25]   C.A. Gueymard. "The Sun's Total and Spectral Irradiance for Solar Energy Applications and Solar Radiation Models". In: *Solar Energy* 76.4 (2004), pp. 423–453. ISSN: 0038-092X.

[26]   C.A. Gueymard, D. Myers, and K. Emery. "Proposed Reference Irradiance Spectra for Solar Energy Systems Testing". In: *Solar Energy* 73.6 (2002), pp. 443–467. ISSN: 0038-092X.

[27]   Z. Haddad, E. Abu-Nada, H.F. Oztop, and A. Mataoui. "Natural Convection in Nanofluids: Are the Thermophoresis and Brownian Motion Effects Significant in Nanofluid Heat Transfer Enhancement?" In: *International Journal of Thermal Sciences* 57 (2012), pp. 152–162.

[28]   D.A. Hagos, A. Gebremedhin, and B. Zethraeus. "Solar Water Heating as a Potential Source for Inland Norway Energy Mix". In: *Journal of Renewable Energy* 2014 (2014), p. 968320.

[29]   G. M. Hale and M.R. Querry. "Optical Constants of Water in the 200-nm to 200-μm Wavelength Region". In: *Applied Optics* 12.3 (Mar. 1973), pp. 555–563.

[30]   D. Han, Z. Meng, D. Wu, C. Zhang, and H. Zhu. "Thermal Properties of Carbon Black Aqueous Nanofluids for Solar Absorption". In: *Nanoscale Research Letters* 457 (2011).

[31]   W.M. Hashim, A.T. Shomran, H.A. Jurmut, T.S. Gaaz, A.A.H. Kadhum, and A.A. Al-Amiery. "Case Study on Solar Water Heating for Flat Plate Collector". In: *Case studies in Thermal Engineering* 12 (2018), pp. 666–671.

[32]   A.M. Helmenstine. *An Introduction to Brownian Motion*. Last accessed 28 June 2019. 2019. URL: thoughtco.com/brownian-motion-definition-and-explanation-4134272.

[33]   M.R. Hestenes and E. Stiefel. "Methods of Conjugate Gradients for Solving Liner Systems". In: *Journal of Research fo the National Bureau of Standards* 49.6 (1952), pp. 409–436.

[34]   N.J. Hogan, A.S. Urban, C. Ayala-Orozco, A. Pimpinelly, P. Nordlander, and N.J. Halas. "Nanoparticles Heat Through Light Localization". In: *Nano Letters* 14 (2014), pp. 4640–4645.

[35]   H. Jin, G. Lin, L. Bai, M. Amjad, E.P.B. Filho, and D. Wen. "Photothermal Conversion Efficiency of Nanofluids: An Experimental and Numerical Study". In: *Solar Energy* 139 (2016), pp. 278–289.

[36] M. Kalteh, A. Abbassi, M. Saffar-Avval, and J. Harting. "Eulerian-Eulerian Two-phase Numerical Simulation of Nanofluid Laminar Forced Convection in a Microchannel". In: *Elsevier Ltd* 32 (2011), pp. 107–116.

[37] A. Kamyar, R. Saidur, and M. Hasanuzzaman. "Application of Computational Fluid Dynamics (CFD) for Nanofluids". In: *International Journal of Heat and Mass Transfer* 55 (2012), pp. 4104–4115.

[38] M. Karami, M.A. Akhavan-Bahabadi, S. Delfani, and M. Raisee. "Experimental Investigation of CuO Nanofluid-based Direct Absorption Solar Collector for Residental Applications". In: *Renewable and sustainable Energy Reviews* 52 (2015), pp. 793–801.

[39] M. Karimi, G. Akdogan, K.H. Dellimore, and S.M. Bradshaw. "Comparison of Different Drag Coefficient Correlations in the CFD Modelling of a Laboratory-scale Rushton-turbine Flotation Tank". In: *CSIRO Australia* (2012).

[40] S. Kiran and G. Diaz. "Activated Carbondispersion as Absorber for Solar Water Evaporation: A Parametric Analysis". In: *Solar Energy* 184 (2019), pp. 40–51.

[41] N.I. Lebovka, S.V. Khrapatiy, R. Melnyk, and N. Vygornitskii. "Effects of Hydrodynamic Retardation and Interparticle Interactions on the Self-Assembly in a Drying Droplet Containing Suspended Solid Particles". In: *Physical Review* 89 (2014).

[42] J. Lee, K.S. Hwang, S.P. Jang, B.H. Lee, J.H. Kim, S.U.S. Choi, and C.J. Choi. "Effective Viscosities and Thermal Conductivities of Aqueous Nanofluids Containing Low Volume Concentrations of Al_3O_3 Nanoparticles". In: *International Journal of Heat and Mass Transfer* 51 (2008), pp. 2651–2656.

[43] J.H. Lienhard. *A Heat Transfer Textbook.* Dover Publications, 2019.

[44] J. Liu, Z. Ye, L. Zhang, X. Fang, and Z. Zhang. "A Combined Numerical and Experimental Study on Graphene/Ionic Liquid Nanofluid Based on Direct Absorption Solar Collector". In: *Solar Energy Materials and Solar Cells* 136 (2015), pp. 177–186.

[45] Z. Luo, C. Wang, W. Wei, G. Xiao, and M. Ni. "Performance Improvement of a Nanofluid Solar Collector Based on Direct Absorption Collection (DAC) Concepts". In: *International Journal of Heat and Mass Transfer* 75 (2014), pp. 262–271.

[46] O. Mahian, A. Kianifar, S.A. Kalogirou, I. Pop, and S. Wongwises. "A Review of the Applications of Nanofluids in Solar Energy". In: *International Journal of Heat and Mass Transfer* 57 (2013), pp. 582–594.

[47] V.Z. Marmarelis. *Nonlinear Dynamic Modeling of Physiological Systems.* Institute of Electrical and Electronics Engineers, 2004.

[48] R.M. Mazo. *Brownian Motion: Fluctuations, Dynamics and Applications.* Oxford University Press, 2002.

[49] W.L. McCabe, J.C. Smith, and P. Harriot. *Unit Operations of Chemical Engineering.* McGraw-Hill, 2005.

[50] J.E. Minardi and H.N. Chuang. "Performance of a Black Liquid Flat-Plate Solar Collector". In: *Solar Energy* 17 (1975), pp. 179–183.

[51] M. Mirzaei, S.M.S. Hosseini, and A.M.M. Kashkooli. "Assessment of Al_2O_3 Nanoparticles for the Optimal Operation of the Flat Plate Solar Collector". In: *Applied Thermal Engineering* 134 (2018), pp. 68–77.

[52] O. Neumann, A.S. Urban, J. Day, S. Lal, P. Nordlander, and N.J. Halas. "Solar Vapor Generation Enabled by Nanoparticles". In: *American Chemical Society* 7 (2013), pp. 42–49.

[53] R.G. Newell, D. Raimi, and G. Aldana. *Global Energy Outlook 2019: The Next Generation of Energy*. Last accessed 28 August 2019. 2019. URL: https://media.rff.org/documents/GEO_Report_8-22-19.pdf.

[54] G. Ni, N. Miljkovic, H. Ghasemi, X. Huang, S.V. Borinska, C. Lin, J. Wang, Y. Xu, Md. M. Rahman, T. Zhang, and G. Chen. "Volumetric Solar Heating of Nanofluids for Direct Vapor Generation". In: *Nano Energy* 17 (2015), pp. 290–301.

[55] T.P. Otanicar, P.E. Phelan, R.S. Phrasher, G. Rosengarten, and R.A. Taylor. "Nanofluid-based Direct Absorption Collector". In: *Journal of Renewable and Sustainable Energy* 2 (2010).

[56] S.J. Palm, G. Roy, and C.T. Nguyen. "Heat Transfer Enhancement with the use of Nanofluids in Radial Flow Cooling Systems Considering Temperature Dependent Properties". In: *Applied Thermal Engineering* 26 (2006), pp. 2209–2218.

[57] K.M. Pandey and R. Chaurasiya. "A Review on Analysis and Development of Solar Flat Plate Collector". In: *Renewable an Sustainable Energy Reviews* 67 (2017), pp. 641–650.

[58] J. Philip and S.P. Damodaran. "Thermal Properties of Nanofluids". In: *Advances in Colloid and Interface Science* 183–184 (2012), pp. 30–45.

[59] H. R. Phillip and E. A. Taft. "Kramers-Kronig Analysis of Reflectance Data for Diamond". In: *Phys. Rev.* 136 (5A Nov. 1964), A1445–A1448.

[60] B.E. Rapp. *Microfluids: Modelling, Mechanics and Mathematics*. Elsevier Inc., 2017.

[61] V. Rastegar, G. Ahmadi, and S. Babu. "Filtration of Aqueous Colloidal Ceria Slurries Using Fibrous Filters - An Experimental and Simulation Study". In: *Separation and Purification Technology* 176 (2017), pp. 231–242.

[62] H. Richie and M. Roser. *Energy Production Changing Energy Sources*. Last accessed 28 August 2019. 2019. URL: https://ourworldindata.org/energy-production-and-changing-energy-sources.

[63] F. Roelofs and A. Shams. "CFD - Introduction". In: *Thermal Hydraulics Aspects of Liquid Metal Cooled Nuclear Reactors* (2019), pp. 213–218.

[64] R. Saidur, K.Y. Leong, and H. Mohammed. "A Review on Applications and Challenges of Nanofluids". In: *Renewable and Sustainable Energy Reviews* 15 (2011), pp. 1646–1668.

[65] R. Saidur, T.C. Meng, Z. Said, M. Hasanuzzaman, and A. Kamyar. "Evaluation of the Effect of Nanofluid-based Absorbers on Direct Solar Collector". In: *International Journal of Heat and Mass Transfer* 55 (2012), pp. 5899–5909.

[66] *Navier-Stokes on Programmable Graphics Hardware using SMAC*. XVII Brazilian Symposium on Computer Graphics and Image Processing. 2004.

[67] D. Shang and L. Zhong. *Heat Transfer due to Laminar Natural Convection of Nanofluids*. Springer, 2019.

[68] O. Z. Sharaf, D.C. Kyritsis, A.N. Al-Khateeb, and E. Abu-Nada. "Effect of Bottom Surface Optical Boundary Conditions on Nanofluid-based DASC: Parametric Study and Optimization". In: *Solar Energy* 164 (2018), pp. 210–223.

[69] O.Z. Sharaf, A.N. Al-Khateeb, D.C. Kyritsis, and E. Abu-Nada. "Direct Absorption Solar Collector (DASC) Modelling and Simulation Using a Novel Eulerian-Lagrangian Hybrid Approach: Optical, Thermal and Hydrodynamic Interactions". In: *Applied Energy* 231 (2018), pp. 1132–1145.

[70] T. Sheikhalipour and A. Abbassi. "Numerical Analysis of Nanofluid Flow Inside a Trapezoidal Microchannel Using Different Approaches". In: *Advanced Powder Technology* 29 (2018), pp. 1749–1757.

[71]   Siemens PLM Software Simcenter. *STAR-CCM+ User guide for version 13.06*. Last accessed 27 August 2019. 2019.

[72]   S.T. Surjikov. *Mie Scattering*. Last accessed 13 November 2019. 2011. DOI: `10.1615/AtoZ.m.mie_scattering`.

[73]   R.A. Taylor, P.E. Phelan, T.P. Otanicar, R. Adrian, and R. Prasher. "Nanofluid Optical Property Characterization: Towards Efficient Direct Absorption Solar Collectors". In: *Nanoscale Research Letters* 6 (2011), p. 225.

[74]   Engineering Toolbox. *Water - Dynamic and Kinematic Viscosity*. Last accessed 11 September 2019. 2004. URL: `https://www.engineeringtoolbox.com/water-dynamic-kinematic-viscosity-d_596.html?vA=55&units=C#`.

[75]   E.T. Ulset, P. Kosinski, Y. Zabednova, O.V. Zhdaneev, P.G. Struchalin, and B.V. Balakin. "Photothermal Boiling in Aqueous Nanofluids". In: *Nano Energy* 50 (2018), pp. 339–346.

[76]   Z. Valizadeh and M. Shams. "Numerical Investigation of Water-based Nanofluid Subcooled Flow Boiling by Three-phase Euler-Euler, Euler-Lagrange approach". In: *Heat Mass Transfer* 52 (2015), pp. 1501–1514.

[77]   Dr. A. Verma. *National Programme on Technology enhanced Learning; Heat Transfer*. Last accessed 19 August 2019. 2012. URL: `https://nptel.ac.in/courses/103103032/15`.

[78]   W. Wagner and A. Pruß. "The IAPWS Formulation 1995 for the Thermodynamic Properties of Ordinary Water Substance for General and Scientific Use". In: *Journal of Physical and Chemical Reference Data* 31.2 (2002), pp. 387–535.

[79]   B. Wang, X. Wang, W. Lou, and J. Hao. "Thermal Conductivity and Rheological Properties af Graphite/Oil Nanofluids". In: *Colloids and Surfaces A: Physiochem* 414 (2012), pp. 125–131.

[80]   Z. Warhaft. *The Engine and the Athmosphere: An Introduction to Engineering*. Cambridge University Press, 1997.

[81]   D. Wen, L. Zhang, and Y. He. "Flow and Migration of Nanoparticle in a Single Channel". In: *Heat Mass Transfer* 45 (2009), pp. 1061–1067.

[82]   *What is CFD, Computational Fluid Dynamics?* Last accessed 01 July 2019. 2017. URL: `https://www.simscale.com/docs/content/simwiki/cfd/whatiscfd.html`.

[83]   D.C. Wilcox. *Turbulence Modeling for CFD*. DCW Industries, 2006.

[84]   Z. Yin, X. Li, F. Bao, C. Tu, and X. Gao. "Thermophoresis and Brownian Motion Effects on Nanoparticle Deposition Inside a 90 degree Square Bend Tube". In: *Aerosol and Air Quality Research* 18 (2018), pp. 1746–1755.

[85]   L. Zhang, J. Shao, and X. Chen. "CFD Simulation of Nozzle Characteristics in a Gas Aggregation Cluster Source". In: *Vacuum* 129 (2016), pp. 105–110.

[86]   K. Zhukovsky, D. Oskolkov, and N. Gubina. "Some Exact Solutions to Non-Fourier Heat Equations with Substantial Derivative". In: *Axioms* 7 (2018), pp. 179–183.

Appendices

Appendix A

Theoretical Calculations

This appendix shows the values used for theoretical calculations of the force magnitude. Thermodynamic properties of water and graphite are collected from the model description in chapter 5.5.

Table A.1: Calculated values for Brownian and thermophoretic forces.

$\Delta\mathbf{T}[^{\circ}\mathrm{C}]$	$\mathbf{S}_0$	$\mathbf{F}_B[\mathrm{N}]$	kc/kd	β	$\mathbf{F}_{Th}[\mathrm{N}]$
0	2075413567	1.12638×10^{-17}	0.000310769	2.136×10^{-8}	0
5	1844293271	1.06182×10^{-17}	0.000314872	2.13622×10^{-8}	4.4957×10^{-18}
10	1680407971	1.01354×10^{-17}	0.000318462	2.13642×10^{-8}	7.3506×10^{-18}
15	1526794683	9.66106×10^{-18}	0.000322051	2.13661×10^{-8}	9.0459×10^{-18}
20	1393725421	9.23045×10^{-18}	0.000325128	2.13678×10^{-8}	9.9934×10^{-18}
25	1276997999	8.83547×10^{-18}	0.000328205	2.13694×10^{-8}	1.0435×10^{-17}
30	1176612416	8.48108×10^{-18}	0.000331282	2.13711×10^{-8}	1.0563×10^{-17}
35	1086965756	8.15159×10^{-18}	0.000333333	2.13722×10^{-8}	1.0467×10^{-17}

Table A.2: Calculated values for steady-state drag force and updated drag force. Force acting in the height of H/2.

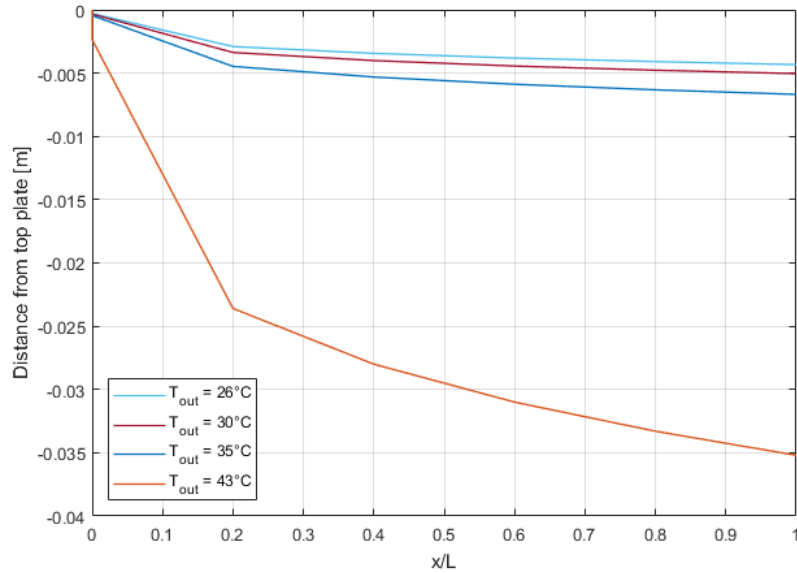| $\mathbf{T}_{out}[^\circ\text{C}]$	$\mathbf{Re}_r$	$\mathbf{C}_D[\text{N}]$	$\mathbf{F}_{D,ss}[\text{N}]$	$\mathbf{F}_{D,corr}$
25	8.74758×10^{-5}	274429	6.538×10^{-13}	2.459×10^{-13}
30	9.83392×10^{-5}	244118	5.810×10^{-13}	2.185×10^{-13}
35	0.000107713	222877	5.294×10^{-13}	1.991×10^{-13}
40	0.000118312	202915	4.810×10^{-13}	1.809×10^{-13}
45	0.000129347	185607	4.391×10^{-13}	1.651×10^{-13}
50	0.000140885	170410	4.023×10^{-13}	1.513×10^{-13}
55	0.000152595	157335	3.707×10^{-13}	1.394×10^{-13}
60	0.000164678	145794	3.425×10^{-13}	1.288×10^{-13}

Figure A.1: Calculated values for thickness of thermal boundary layer at different outlet temperatures, plotted against dimensionless position.

Appendix B

Publication

This appendix shows a paper that is planned to be submitted for a journal publication.

Eulerian CFD Model of Direct Absorption Solar Collector with Nanofluid

Runa Bårdsgård, Dmitrii M. Kuzmenkov, Pawel Kosinski, Boris V. Balakin

December 4, 2019

Abstract. Solar energy is the most promising source of renewable energy. However, the solar energy harvesting process has relatively low efficiency, while the use of solar energy is challenging. Direct Absorption Solar Collectors (DASC) have been proved to be effective for a variety of applications. In this article, a numerical study of a nanofluid direct absorption solar collector was performed using CFD. A flat plate DASC with incident light on the top surface was simulated using an Eulerian-Eulerian two-phase model. The model was validated against the experiments. A number of parameters such as collector height, particle concentration, and bottom surface properties were tested. Investigation of the particle concentration showed that the optimum volume fraction of particles for enhancing efficiency was obtained for 0.3 wt%, and a decrease in efficiency was observed for ≥ 0.5 wt%. Design recommendations based on the numerical analysis were presented. The optimum configuration of the collector considered reaches the best efficiency of 68% for 300 μm thickness of the receiver and the highest total efficiency is 87% at the velocity of 3 cm/s. The deposition of the particles in the collector was studied, with the finding that over 10% of the nanoparticles are captured in the collector.

1 Introduction

To meet the world's energy demands, and to prevent more harmful emissions, renewable energy sources are good alternatives. Solar energy has the greatest potential of all the sources of renewable energy, especially when other sources are depleted [23]. However, electricity generation from solar energy is not efficient enough to replace fossil fuels and coal in northern countries, where the solar resources are insufficient. In this case, the solar thermal power becomes more interesting as over 65% of a household's electrical energy consumption is used to heat the premises [12]. Enhancing the heat transfer process in solar energy systems is essential to achieving better performance of these systems and reducing their dimensions. In a direct absorption solar collector (DASC), a heat transfer fluid volumetrically absorbs the incidental solar radiation.

Nanofluids are considered to be the most efficient heat transfer fluids for this type of collectors. Otanicar et al. [21] demonstrated four advantages of using DASC over conventional collectors by studying how to improve the efficiency of nanofluid technology. These advantages include limiting heat losses from peak temperature, maximising the spectral absorption of solar energy, enhancement of thermal conductivity, and enhancement of surface areas due to tiny particle sizes. They also used a microsized DASC, and detected excellent enhancement of the collector's thermal efficiency. Mirzaei et al. [18] compared conventional flat-plate collectors and direct absorption solar collectors and observed an efficiency increase of 23.6% for nanoparticle (NP) volume fractions of 0.1%. The nanofluid used in their experiment was 20 nm Al_2O_3 particles dispersed in water.

One of the first detailed descriptions of effective heat generation by NPs was obtained by Neumann et al. [19]. They studied the absorption of NPs dispersed in water and demonstrated efficient steam generation using solar illumination. The solar illumination is approximately 1 kW/m^2 [7, 20]. The experiments were performed to show boiling by illumination and generated steam temperatures of up to 150°C. Their thermodynamic analysis showed that 80% of the absorbed sunlight is converted into water vapour, and only 20% of the absorbed light energy is converted into heating of the surrounding liquid. Ni et al. [20] studied the effect of different nanofluids on the receiver efficiency by performing solar vapor generation experiments on a custom-built lab-scale receiver. In their study, for low concentration sunlight (10 suns), the efficiency was 69%. Running a numerical analysis of the problem, better performance was found in transient situations for graphitised CB and graphene nanofluids than for CB nanofluid. Finally, the study by Ghasemi et al. [7] shows a solar thermal efficiency of up to 85% at low concentration sunlight.

Although there have not been many computational studies of the flow of nanofluids in DASC, a number of papers consider flow and heat transfer of nanofluids in thermal systems of other types. Yin et al. [30] investigated how aerosol NPs were affected by forces using a discrete phase model that was used to investigate the particle motion. It was observed that the main forces acting on the particle are the drag, Brownian and thermophoretic forces. The simulation results included the efficiency and deposition patterns at different temperature gradients. Haddad et al. [11] observed that thermophoresis and Brownian motion enhanced heat transfer in the nanofluid. The enhancements were higher at lower vol-

ume fractions. Another study, by Burelbach et al. [5], investigated the behaviour of colloids under the impact of a thermophoretic force. They discovered that the thermophoretic force varies linearly with the temperature gradient.

A comprehensive numerical analysis of a microsized DASC with nanofluid was performed by Sharaf et al. [24], who modelled the collector using a Eulerian-Lagrangian approach. They discovered that the Reynolds number has a strong effect on the local NP distribution in the flow of a nanofluid. The results obtained are important when designing this type of solar collector because they demonstrate how the performance of the collector depends on the spatial distribution of NPs. The simulation results were in excellent agreement with the experiment. However, the particles were modelled using the Lagrangian approach which is computationally expensive and, therefore, becomes hardly scaled to a DASC with dimensions of industrial relevance.

Luo et al. [17] investigated performance improvements of a DASC solar collector with nanofluids. They used a simulation model combining the radiative heat transfer in a particular media with convective and conductive heat transfer in the DASC collector to predict the photothermal efficiency. Various NPs were used. The simulation results include how specific NPs can have acceptable performance, to improve the efficiency of a DASC [17]. Also, Gorji and Ranjbar [8] studied how to optimise the dimensions of a nanofluid filled DASC. They focused on the DASC geometry and its effect on thermal efficiency and entropy. One of the conclusions was that increased length and larger heights were beneficial for thermal efficiency and entropy, but had the opposite impact on the overall performance. Sharaf et al. [25] investigated the geometry of microsized collectors. Their study indicated that lower collector heights gives the best collector performance. Additionally, various surface materials were tested.

In this paper, we propose a pragmatic CFD-model of the nanofluid-based DASC based on the Eulerian-Eulerian approach, which requires low computational power and is therefore suitable for various particle concentrations and dimensions of the collector. Making use of the developed model, we study how the boundary conditions and the dimensions of the collector influence its thermal efficiency and deposition of particles.

2 Model description

2.1 Flow geometry

The flat-plate geometry modelled in this study was adapted from Otanicar et al. [21], who constructed a micro-scale-thermal-collector pumping a nanofluid between two parallel plates with dimensions of 3×5 cm^2. The thickness of the gap was 150 μm. The microchannel geometry is presented schematically in Fig. 1. For simplification and computational time reduction purposes, an axisymmetric cross-section of the plate is used in these simulations. The length of the cross-section is 5 cm, the width 45 μm and the height 150 μm. The computational domain was discretised with uniform 20-μm cubical mesh.

2.2 CFD-model

The nanofluid is modelled using the Eulerian-Eulerian two-fluid model, which assumes that both phases (base fluid and NPs) constitute two different interpenetrating fluids, with equal pressure. Conservation equations were used separately for each of the phases. The continuity equation is given by [28]:

$$\frac{D(\alpha_i \rho_i)}{Dt} = 0, \Sigma \alpha_i = 0, \qquad (1)$$

where D/Dt is the substantial derivative, and α_i, ρ_i and $\mathbf{v}_i$ are the volume fraction, the density and the velocity vector of the respective phase. Each phase is denoted by $i = p$ for the NPs and $i = f$ for the base fluid. The thermophysical properties of water were defined by IAWPS formulation [29]. The density of the particle material was ρ_p=2210 kg/m^3.

The Eulerian momentum equation becomes [1]:

$$\frac{D(\alpha_i \rho_i \mathbf{v}_i)}{Dt} = -\alpha_i \nabla p + \nabla \cdot (\alpha_i \mu_i \nabla \mathbf{v}_i) + \alpha_i \rho_i \mathbf{g} + \mathbf{F}_D + \delta_{i,j} \mathbf{F}_{th}, \qquad (2)$$

where p is the static pressure, μ is the dynamic viscosity, $\mathbf{g}$ is acceleration due to gravity and δ is Kronecker delta. The volume fraction of the particles in DASC is below 1%, so the influence of the particles to the rheology of the nanofluid is assumed to be negligible. We therefore assume particulate phase viscosity equivalent to the viscosity of the base fluid.

The drag force $\mathbf{F}_D$ is computed using the standard expression by Schiller-Naumann [6] and further corrected with Cunningham's expression to account for rarefaction [6]:

$$C_c = 1 + Kn(2.49 + 0.85 \exp[-1.74/Kn]), \qquad (3)$$

where Knudsen's number $Kn = \lambda_m/d_p$, d_p=30 nm is the size of the particles and λ_m is the molecular mean free path in the base fluid.

Thermophoresis in dilute suspensions is driven by hydrodynamic stresses resulting from local interaction between particle and fluid [5]. The thermophoretic force $\mathbf{F}_{th}$ is computed following Brock's approximation [4]:

$$F_{Th} = \frac{-6n_p \pi \mu_f \nu_f D C_s}{1 + 6C_m Kn} \frac{k_f/k_p + 2C_t Kn}{1 + 2k_f/k_p + 4C_t Kn} \nabla T, \qquad (4)$$

where k_i is the thermal conductivity of phases, n_p is the number density of the particles, ν is the kinematic viscosity, C_s is the thermal slip coefficient, C_t is the thermal exchange coefficient, and C_m is the momentum exchange

coefficient. The best values based on kinetic theory are $C_s = 1.17$, $C_t = 2.18$ and $C_m = 1.14$ [6].

The energy equation is given by [15]:

$$\frac{D(\alpha_i \rho_i e_i)}{Dt} = \nabla(\alpha_i \rho_i \nabla T_i) - q_{ij} + q_{V,i}, \qquad (5)$$

where $e_i = C_{pi} T_i$ is the phase-specific enthalpy, q_v is the volumetric heat generation due to absorption of radiant heat by the phases, and q_{ij} is the inter-phase heat transfer term. With the assumption that there is convective heat transfer between the phases, the inter-phase heat transfer term is computed according to Ranz-Marshall [6].

2.3 Optical model

The volumetric heat generation in nanofluid exposed to solar radiation was derived following Bohren and Huffman [3], where the extinction cross-section of an individual spherical particle reads as:

$$C_{ext} = \frac{2\pi}{|x(\lambda)|^2} \sum_{i=1}^{\infty} (2i+1) \Re \left[a_i + b_i \right]. \qquad (6)$$

In Eq. (6) λ is a wavelength, $x(\lambda) = 2\pi n(\lambda)/\lambda$ is a wave number; $n(\lambda)$ is a real part of the complex refractive index of the base fluid, and a_i and b_i are coefficients of scattered electromagnetic field, that can be written as follows:

$$a_i = \frac{m\psi_i(m\overline{\alpha})\psi_i'(\overline{\alpha}) - \psi_i(\overline{\alpha})\psi_i'(m\overline{\alpha})}{m\psi_i(m\overline{\alpha})\xi_i'(\alpha) - \xi_i(\overline{\alpha})\psi_i'(m\overline{\alpha})}; \qquad (7)$$

$$b_i = \frac{\psi_i(m\overline{\alpha})\psi_i'(\overline{\alpha}) - m\psi_i(\overline{\alpha})\psi_i'(m\overline{\alpha})}{\psi_i(m\overline{\alpha})\xi_i'(\overline{\alpha}) - m\xi_i(\overline{\alpha})\psi_i'(m\overline{\alpha})}, \qquad (8)$$

where m is a complex refractive index of the particle relative to the base fluid; $\overline{\alpha} = \pi n(\lambda) d_p / \lambda$ is the size parameter of particle; $\psi_i(z)$ and $\xi_i(z)$ are Riccati-Bessel

functions of i-th order. Riccati-Bessel functions are related to the Bessel functions of the first (J_ν) and second (Y_ν) kind: $\psi_i(z) = \sqrt{\pi z/2} J_{i+1/2}(z)$ and $\xi_i(z) = \sqrt{\pi z/2}(J_{i+1/2}(z) + Y_{i+1/2}(z))$.

As can be seen from Eq.(6), the expression of the extinction cross-section includes infinite series that are hardly resolved numerically. In order to simplify this calculation, a maximum index n_{max} is used. According to Kiran and Diaz [16], a maximum index can be calculated as: $n_{max} = \left[2 + \overline{\alpha} + 4\overline{\alpha}^{1/3} \right]$.

The extinction coefficient of particles in nanofluid with volume fraction α_p can be calculated according to Taylor et al. [26]:

$$\sigma_p = \frac{3}{2} \alpha_p \frac{Q_{ext}}{d_p}, \qquad (9)$$

where Q_{ext} is the extinction efficiency, which is related to the extinction cross-section, as $Q_{ext} = C_{ext}/S_p$; S_p is the area of the particle cross-section.

The total extinction coefficient of the nanofluid is composed of particle and base fluid extinction coefficients:

$$\sigma_{nf} = \sigma_p + (1 - \alpha_p)\sigma_f, \qquad (10)$$

where $\sigma_f = 52\text{m}^{-1}$ [27] is the extinction coefficient of the continuous phase, which can be calculated according to Bohren and Huffman [3] as $\sigma_f = 4\pi k(\lambda)/\lambda$; and $k(\lambda)$ is the imaginary part of the complex refractive index of the base fluid. The optical properties of the base fluid $k(\lambda)$ and the particles m are found elsewhere [13, 22].

In order to calculate the solar heat flux in nanofluid as a function of distance from the entrance to the volume of nanofluid, and dependent on particle concentration, it is necessary to specify the spectral distribution of incident radiation $I(\lambda)$, which is given in [2, 10, 9].
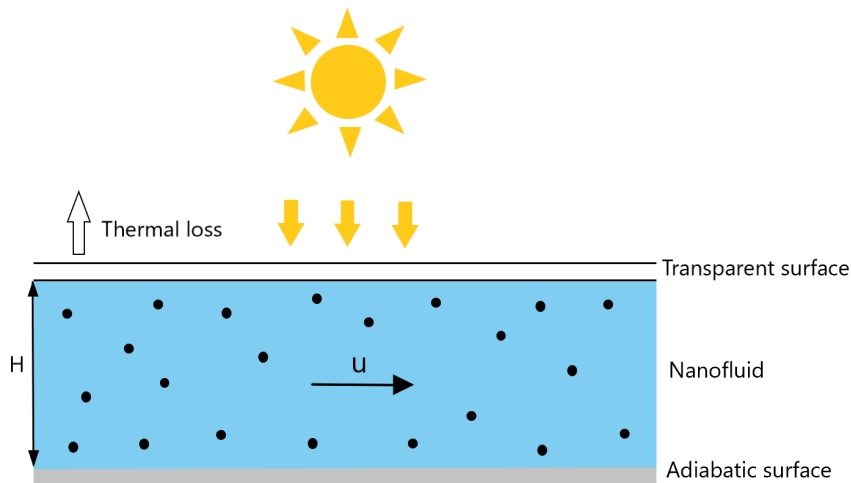
According to Beer-Lambert's law, the solar heat flux

Fig. 1: Schematic description of the model.

3

in nanofluid reads as:

$$q = \int\limits_{0}^{\infty} I(\lambda)\exp\left[-x\sigma_{nf}\right]dx. \qquad (11)$$

Eq. (11) is hardly applicable for use in CFD simulation due to the high computational costs associated with integration of the function. To realise the calculation of solar heat flux in CFD simulation, the equivalent depth of optical penetration l_{eq} was computed for 30-nm carbon nanoparticles at different particle concentrations. The equivalent depth of optical penetration is defined as a distance from the light entrance to the nanofluid, towards the place at which the total heat flux becomes e times smaller. Thus, the equivalent depth of optical penetration is computed when the numerically-solved Eq. (11) becomes equivalent $q_0 e^{-1}$. The reciprocal of the equivalent depth of optical penetration, $\overline{\sigma_{nf}} = l_{eq}^{-1}$, is considered as the equivalent extinction coefficient.

Equation 11 was solved numerically outside the CFD model for a variety of nanoparticle concentrations. The integral in equation 11 was computed using the trapezoidal rule with 1 nm wavelength steps. Further, we fitted the equivalent extinction coefficient as a function of particle volume fraction with a simplified expression of the type using the conjugate gradient method [14]:

$$\overline{\sigma_{nf}} = \frac{2}{\pi}(A + B\alpha_p)\arctan\left(\kappa\alpha_p\right) + \overline{\sigma_f}. \qquad (12)$$

Fitting the equivalent extinction coefficient $\overline{\sigma_{nf}}$ with the expression from Eq. (12) resulted in the following values of fitting coefficients: $A = 2020.07\mathrm{m}^{-1}$, $B = 9.53094 \cdot 10^6 \mathrm{m}^{-1}$ and $\kappa = 8031.63$. In this equation, $\overline{\sigma_f}$ is an equivalent extinction coefficient of the base fluid. The approximation result is presented in Fig. 2, where the extinction coefficient is resolved numerically (line) and compared to Eq. (12) (boxes) for different particle concentrations.

The solar heat flux in nanofluid can be therefore written as $q = q_0\exp\left[-x\overline{\sigma_{nf}}\right]$, where q_0=1 sun is the incident solar radiation. The volumetric heat generation then becomes:

$$q_v = -dq/dx = q_0\overline{\sigma_{nf}}\exp\left(-\overline{\sigma_{nf}}l\right), \qquad (13)$$

where l is the optical path in the direction of thermal radiation and $\overline{\sigma_p} = \overline{\sigma_{nf}} - \overline{\sigma_f}$.

2.4 Boundary conditions

The boundary conditions include two symmetry planes at the frontal surfaces of the model, and a velocity inlet on the left of the section studied. The inlet boundary condition sets the uniform distribution of velocity, volume fraction and temperature (25 °C). The equivalent flow parameters were set for the initial condition. The outlet boundary defines the zero field of relative pressure, uniform distribution of volume fraction and zero gradient of temperature are at the exit of the model.

The bottom and the top boundary are the no-slip walls. The top wall of the DASC is exposed to solar radiation, and the distribution of volumetric heat generation is set accordingly in Eq. (13). Following Otanicar et al. [21], the top boundary was identified as the only source of thermal loss with an equivalent heat transfer coefficient in the range $h \in [23, 34]$ W/m^{2}K for NP volume fractions $\in [0, 1]\%$. This coefficient accounts for thermal leaks due to convection of air around the collector at the ambient temperature of 25 °C.

There are two alternatives for the bottom boundary thermal condition. An adiabatic boundary is prescribed there for the base-case simulations. Further, to understand the influence of a black-body bottom of the collector we prescribed a constant heat flux at the boundary. The absolute value of the boundary heat flux was set proportionally to the radiate heat flux absorbed by the bottom of the collector.

3 Results and discussion

3.1 Model validation

The model was validated against the experimental results from Otanicar et al. [21]. We focused on the thermal efficiency of the collector. The thermal efficiency of the DASC is defined as the ratio of the thermal energy consumed to the incident solar energy [21]:

$$\eta_T = \frac{\int_{y=0}^{y=H}\left(v_o C_{nf,o}\rho_{nf,o}T_{f,o} - v_i C_{nf,i}\rho_{nf,i}T_{f,i}\right)dy}{q_0 \cdot H}, \qquad (14)$$

where H is the thickness of the collector in the direction normal to flow and solar radiation, $C_{nf} = \alpha_p C_{p,p} + \alpha_l C_{p,l}$ and $\rho_{nf} = \alpha_p\rho_p + \alpha_l\rho_l$ are the equivalent specific heat and the density of the nanofluid, and indices o and i denote inlet and outlet boundaries.

Validating our model in Fig.3, we note a qualitatively similar evolution of the thermal efficiency at different particle concentrations. The DASC does not entirely absorb the radiant heat at a dilute particle concentration so the efficiency is low there. Furthermore, on increasing the amount of nanoparticles the efficiency goes up to 62% at 0.3 wt%. For even higher NP concentration, most of the radiant heat absorbs at the top surface of the collector, increasing the temperature of the top boundary. This enhances the thermal leak to the surroundings and the thermal efficiency of the collector is reduced again. The maximum discrepancy of the experiments is 12% and the greatest deviation from the experiment is observed close to the maximum of the function. This inaccuracy is addressed to the approximation that we made for the extinction coefficient and the experimental uncertainty in the determination of thermal leaks.
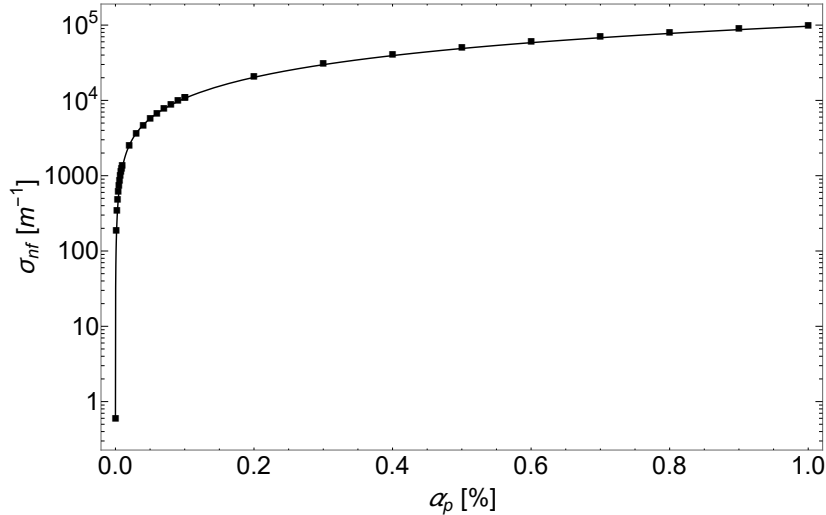
Fig. 2: Equivalent extinction coefficient as a function of particle concentration.

3.2 Flow asymmetry

Fig. 4a demonstrates profiles of the nanoparticle concentration at different axial positions of the collector. It follows from the figure that the nanoparticles are not uniformly distributed in the cross-section; the profiles are asymmetrical. This is explained by the mutual action of gravity and thermophoresis drifting the particles towards the bottom boundary. The asymmetry increases closer to the outlet from the collector. The deposition of particles influences the optical properties of the nanofluid. Our model results presented in Fig. 4b confirm the simulation results given in [24] which first demonstrated reduction of the extinction coefficient at the surfaces of the collector.

Due to the low concentration and size of the particles, the phases are weakly coupled and the concentration profiles do not affect the symmetry of the velocity and the temperature patterns. Thus, the temperature increases linearly from the inlet towards the outlet of the collector.

In order to investigate how the nanoparticles deposit in the solar collector, we considered another parameter, termed the deposition efficiency, which is given as:

$$\eta_{dep} = \frac{\alpha_{p,in} - \alpha_{p,out}}{\alpha_{p,in}} \times 100\%, \quad (15)$$

where $\alpha_{p,in}$ and $\alpha_{p,out}$ are the volume fraction of particles at inlet and outlet.

Fig. 5a shows the results from these simulations for different collector sizes and types of boundary condition. As the figure shows, the greatest deposition efficiency was 11% for the lowest size of the gap. Furthermore, increas-
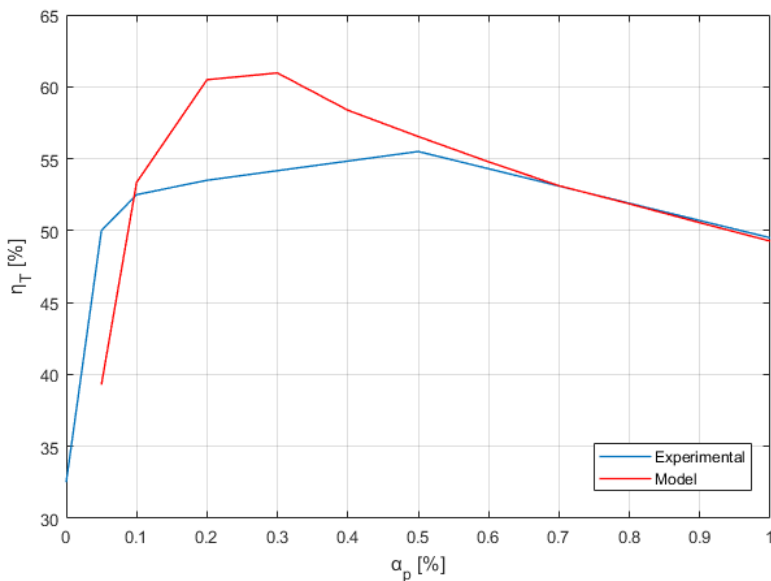

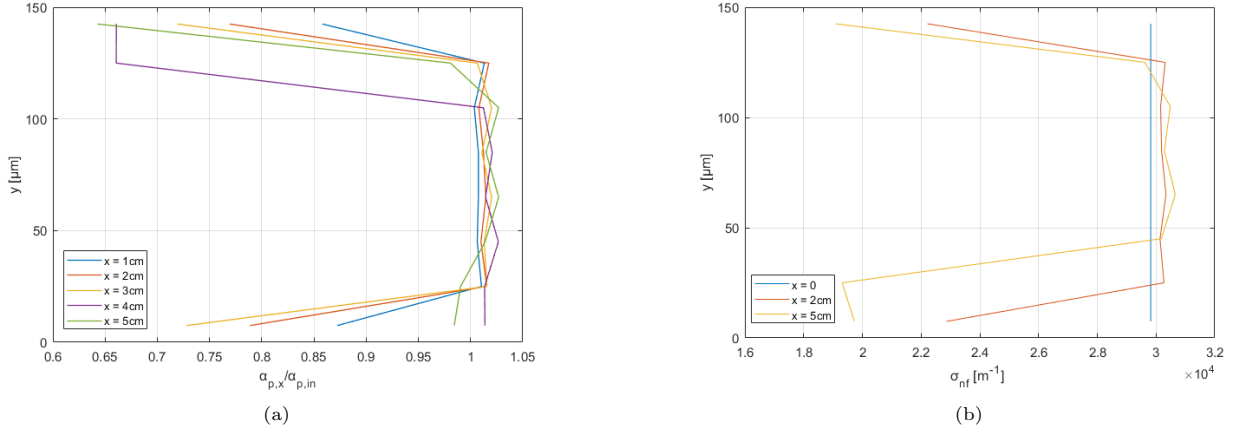Fig. 3: Thermal efficiency as a function of particle concentration.

Fig. 4: a) Transverse distribution of particle concentration, scaled by the inlet value and b) the nanofluid extinction coefficient at different axial coordinates of the collector.
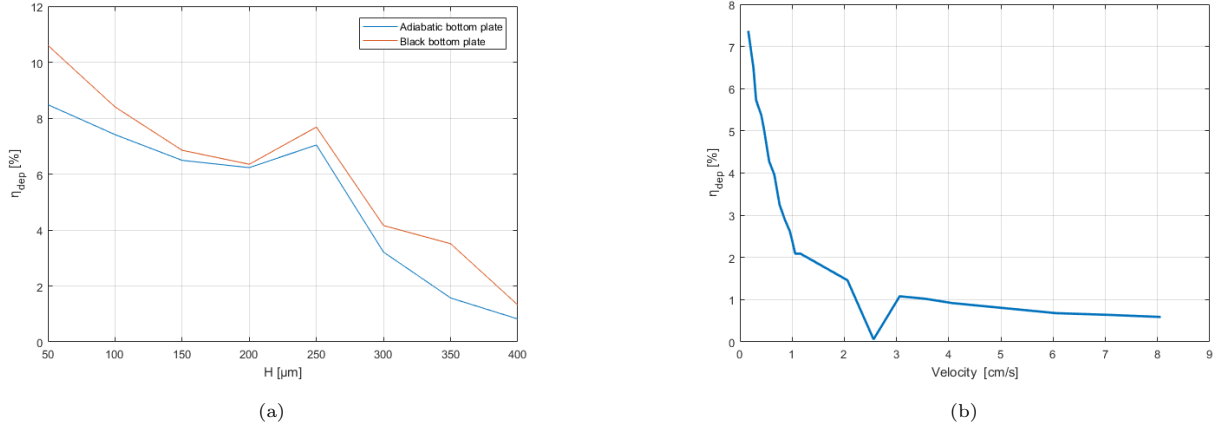

Fig. 5: Deposition efficiency as a function of a) collector height and b) inlet velocity.

ing the size reduces the deposition efficiency. This is explained by the destabilising action of the thermophoretic force, which deposits more particles in a narrow gap, while the dispersive action of drag becomes stronger for a wider collector. Moreover, the temperature decreases with the height of the collector, weakening the thermophoresis. For the model with a black absorptive surface, the deposition efficiency is higher. Fig. 5b shows that the deposition efficiency reduces asymptotically to 0.8% with the mean flow velocity, due to better agitation of the dispersed phase.

3.3 Parametric analysis

The height of the solar collector has vital influence on the amount of heat absorbed and transferred by the nanofluid. There is an optimum height/length ratio associated with the best thermal performance of the collector [8]. The results of the model-based optimisation are presented in Fig. 6, where the thermal efficiency and the outlet temperature are shown for different heights of the collector and types of the bottom boundary. As the figure shows, by increasing the thickness less heat is taken by the nanofluid flow and the temperature decreases. The outlet temper-

ature decreases almost linearly with the collector height. This limits the thermal losses and the collector efficiency increases. The observed dependence of the thermal efficiency on the height of the volumetric receiver is consistent with the results obtained by [25]. However, at a thickness of 300 μm, the efficiency begins to reduce as the volumetric absorption is no longer active across the entire volume of nanofluid. The consumed heat therefore leaks to internal fluid layers with the incipient volumetric absorption, which reduces the thermal efficiency.

Fig. 6 shows that for collector heights lower than 200μm, the efficiency is higher for the model with the black absorbing bottom plate. In this case, a warmer bottom surface returns absorbed heat back into the process, boosts the thermal efficiency, and increases the outlet temperature. At the point of maximum difference, the efficiency is 12% higher for the black bottom plate, than for the transmissible adiabatic plate. This occurs at the lowest collector height tested, 50μm. For collector heights above 200μm, the thermal efficiency decays towards the values for the case with the adiabatic bottom. This can be explained by the fact that on increasing the gap, the
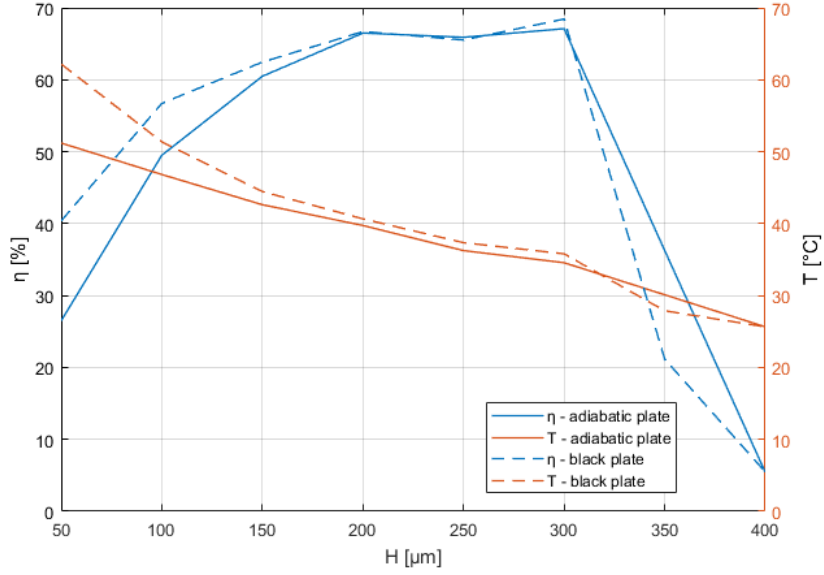
6

Fig. 6: Thermal efficiency and outlet temperature as a function of collector height for different types of boundary conditions at 0.3 wt% NPs and 0.26 cm/s fluid velocity.

nanofluid consumes most of the thermal radiation in the bulk and the bottom does not receive sufficient heat.

Otanicar et al. [21] conducted a test whereby the bottom copper plate was painted black, to imitate an absorbing blackbody, which resulted in increased collector efficiency. The blackbody absorbs the rest of the transmitted radiation and heats up the fluid, so that the thermal convection develops from the bottom surface of the collector. The supplementary mixing in the direction transverse to the main flow boosts the thermal efficiency. We reproduced this experiment for the case where only the continuous phase (water) was present in the collector. In addition, we performed another simulation whereby the perfect absorption is assumed at the top boundary, so that the heat flux equivalent to q_0 was prescribed there. The volumetric absorption results were obtained from the model with volume fraction of particles at 0.3 wt% and a collector height of 300 μm. Fig. 7 shows the difference in efficiency for the different collectors. As the figure shows, the vol-

umetric absorption system outperforms the surface-based collector by at least 20%. This result is consistent with our previous studies [1].

3.4 Total efficiency

Studying the influence of flow rate on the thermal efficiency of the process, we note the pumping cost penalty growing with the flow velocity. To account for this effect, we define a total efficiency of the process:

$$\eta = \eta_T - \frac{Q\Delta P}{q_0 A}, \tag{16}$$

where Q is the volumetric flow, ΔP is the friction pressure drop in the collector, and A is the irradiated area of the collector. Another factor that needs to be accounted for is the turbulence that occurs when $v > 4.6$ cm/s. To calculate the turbulent stress in Eq.2, the CFD-model was updated with RANS and the $k - \epsilon$ model. Fig. 8 demon-
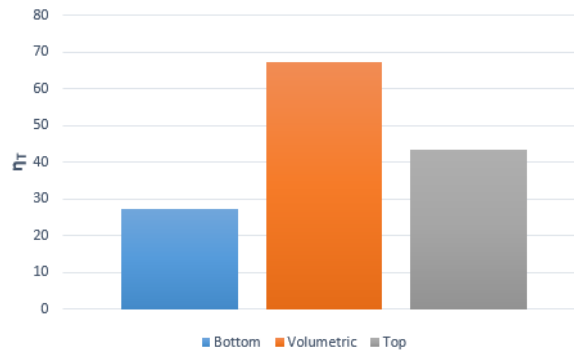

Fig. 7: Thermal efficiency for different types of boundary conditions.
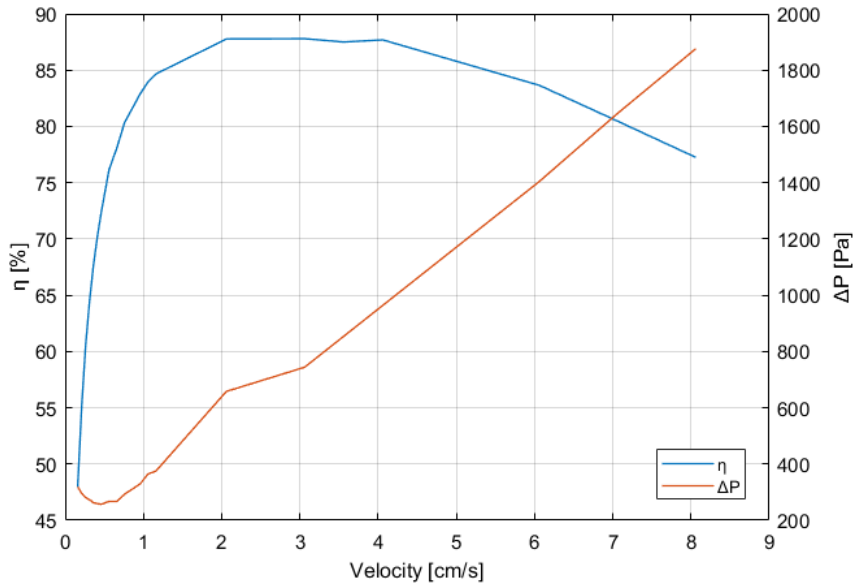
7

Fig. 8: Total efficiency and pressure loss as a function of nanofluid velocity.

strates how the total efficiency and the pressure drop depend on the mean flow velocity.

The results from Fig. 8 show that a peak efficiency of 87% is obtained at u=3 cm/s. This efficiency is 42% higher than for the base case, and 30% higher than the maximum efficiency obtained when optimising the collector height. We also note that the pumping cost penalty in Fig. 8 increases continuously with the mean flow velocity, so that the total efficiency decreases for velocities > 4 cm/s.

4   Conclusion

An Eulerian-Eulerian two-phase model was developed to simulate the flow of carbon-based aqueous nanofluid in the direct absorption solar collector. The model is capable of simulating thermophoresis and reproduces optics of the sunlight absorption in the nanofluid. The model was validated against the experimental data and furthermore used for the parametric optimisation of the collector. The parameters considered were the concentration of the nanoparticles, the geometry of the collector, the flow rate and the optical properties of the boundaries.

The results of the CFD-analysis demonstrate an asymmetry in the particulate phase concentration profile and the respective non-uniformity of the optical properties of the nanofluid. The deposition of the particles takes place in the collector so that maximum 10% of the particles are captured in the DASC.

The model-based optimisation resulted in 0.3 wt% optimum concentration of 30-nm nanoparticles and 300 μm thickness of the collector. The nanofluid velocity through the collector also has a significant impact on the thermal efficiency. The maximum total efficiency of 87% is

obtained when the flow velocity is 3 cm/s, and decreases with higher velocities. The deposition efficiency and outlet temperature decrease for higher velocities.

The effect of the absorbing bottom surface of the collector was tested. The collector with a black bottom containing only water proved to be effective although outperformed by 40% for the case with the volumetric absorption of the nanofluid. A top surface black absorber was also tested, and was not shown to be efficient. This technology resembles a conventional flat-plate collector, as mentioned in the introduction. The light-absorbing bottom boundary, when used together with the nanofluid, improves the thermal performance of the collector by a maximum of 12%.

References

[1]   Boris V. Balakin, Oleg V. Zhdaneev, Anna Kosinska, and Kirill V. Kutsenko. "Direct absorption solar collector with magnetic nanofluid: CFD model and parametric analysis". In: *Elsevier Ltd* 136 (2018), pp. 23–32.

[2]   R.E. Bird, R.L. Hulstrom, and L.J. Lewis. "Terrestrial solar spectral data sets". In: *Solar Energy* 30.6 (1983), pp. 563–573. ISSN: 0038-092X. DOI: https://doi.org/10.1016/0038-092X(83)90068-3. URL: http://www.sciencedirect.com/science/article/pii/0038092X83900683.

[3]   Craig F. Bohren and Donald R. Huffman. *Absorption and scattering of light by small particles*. Wiley, New York, 1983.

[4]   James R. Brock. "On the theory of thermal forces acting on aerosol particles". In: *Journal of Colloid Science* 17 (1962), pp. 768–780.

[5]   Jerome Burelbach, Mykolas Zupkauskas, robin Lamboll, Yang Lan, and Erika Eiser. "Colloidal motion under the action of a thermophoretic force". In: *The Journal of Chemical Physics* 147 (2017).

[6] Clayton T. Crowe, John D. Schwartzkopf, Martin Sommerfeld, and Yutaka Tsuji. *Multiphase flows with droplets and particles*. CRC press, 2012.

[7] Hadi Ghasemi, George Ni, Amy Marie Marconnet annd James Loomis, Selcuk Yerci, Nenad Milijkovic, and Gang Chen. "Solar Steam Generation by Heat Localization". In: *Nature Communications* (2014).

[8] Tahereh B. Gorji and A. A. Ranjbar. "Geometry optimization of a nanofluid-based direct absorption solar collector using response surface methodology". In: *Solar Energy* 122 (2015), pp. 314–325.

[9] Christian A. Gueymard. "The sun's total and spectral irradiance for solar energy applications and solar radiation models". In: *Solar Energy* 76.4 (2004), pp. 423–453. ISSN: 0038-092X. DOI: https://doi.org/10.1016/j.solener.2003.08.039. URL: http://www.sciencedirect.com/science/article/pii/S0038092X03003967.

[10] Christian A. Gueymard, D. Myers, and K. Emery. "Proposed reference irradiance spectra for solar energy systems testing". In: *Solar Energy* 73.6 (2002), pp. 443–467. ISSN: 0038-092X. DOI: https://doi.org/10.1016/S0038-092X(03)00005-7. URL: http://www.sciencedirect.com/science/article/pii/S0038092X03000057.

[11] Zoubida Haddad, Eiyad Abu-Nada, Hakan F. Oztop, and Amina Mataoui. "Natural convection in nanofluids: Are the thermophoresis and Brownian motion effects significant in nanofluid heat transfer enhancement?" In: *International Journal of Thermal Sciences* 57 (2012), pp. 152–162.

[12] Dejene Assefa Hagos, Alemayehu Gebremedhin, and Bjorn Zethraeus. "Solar Water Heating as a Potential Source for Inland Norway Energy Mix". In: *Journal of Renewable Energy* 2014 (2014), p. 968320.

[13] George M. Hale and Marvin R. Querry. "Optical Constants of Water in the 200-nm to 200-μm Wavelength Region". In: *Applied Optics* 12.3 (Mar. 1973), pp. 555–563. DOI: 10.1364/AO.12.000555.

[14] Magnus R. Hestenes and Eduard Stiefel. "Methods of conjugate Gradients for Solving Liner Systems". In: *Journal of Research fo the National Bureau of Standards* 49.6 (1952), pp. 409–436. DOI: 10.6028/jres.049.044.

[15] Mohammad Kalteh, Abbas Abbassi, Majid Saffar-Avval, and Jens Harting. "Eulerian-Eulerian two-phase numerical simulation of nanofluid laminar forced convection in a microchannel". In: *Elsevier Ltd* 32 (2011), pp. 107–116.

[16] Sal Kiran and Gerardo Diaz. "Activated carbondispersion as absorber for solar water evaporation: A parametric analysis". In: *Solar Energy* 184 (2019), pp. 40–51.

[17] Zhongyang Luo, Cheng Wang, Wei Wei, Gang Xiao, and Mingjiang Ni. "Performance improvement of a nanofluid solar collector based on direct absorption collection (DAC) concepts". In: *International Journal of Heat and Mass Transfer* 75 (2014), pp. 262–271.

[18] Mohsen Mirzaei, Seyed Mohammad Sadegh Hosseini, and Amir Mansour Moradi Kashkooli. "Assessment of Al_2O_3 nanoparticles for the optimal operation of the flat plate solar collector". In: *Applied Thermal Engineering* 134 (2018), pp. 68–77.

[19] Oara Neumann, Alexander S. Urban, Jared Day, Surbhi Lal, Peter Nordlander, and Naomi J. Halas. "Solar Vapor Generation Enabled by Nanoparticles". In: *American Chemical Society* 7 (2013), pp. 42–49.

[20] George Ni, Nenad Miljkovic, Hadi Ghasemi, Xiaopeng Huang, Svetlana V. Borinska, Cheng-Te Lin, Jianjian Wang, Yanfei Xu, Md. Mahfuzur Rahman, TieJun Zhang, and Gang Chen. "Volumetric solar heating of nanofluids for direct vapor generation". In: *Nano Energy* 17 (2015), pp. 290–301.

[21] Todd P. Otanicar, Patrick E. Phelan, Ravi S. Phrasher, Gary Rosengarten, and Robert A. Taylor. "Nanofluid-based direct absorption collector". In: *Journal of Renewable and Sustainable Energy* 2 (2010).

[22] H. R. Phillip and E. A. Taft. "Kramers-Kronig Analysis of Reflectance Data for Diamond". In: *Phys. Rev.* 136 (5A Nov. 1964), A1445–A1448. DOI: 10.1103/PhysRev.136.A1445. URL: https://link.aps.org/doi/10.1103/PhysRev.136.A1445.

[23] R. Saidur, K.Y Leong, and H.A. Mohammed. "A review on applications and challenges of nanofluids". In: *Renewable and Sustainable Energy Reviews* 15 (2011), pp. 1646–1668.

[24] Omar Z. Sharaf, Ashraf N. Al-Khateeb, Dimitrios C. Kyritsis, and Eiyad Abu-Nada. "Direct absorption solar collector (DASC) modelling and simulation usind a novel Eulerian-Lagrangian hybrid approach: Optical, thermal and hydrodynamic interactions". In: *Applied Energy* 231 (2018), pp. 1132–1145.

[25] Omar Z. Sharaf, Dimitrios C. Kyritsis, Ashraf N. Al-Khateeb, and Eiyad Abu-Nada. "Effect of bottom surface optical boundary conditions on nanofluid-based DASC:Parametric study and optimization". In: *Solar Energy* 164 (2018), pp. 210–223.

[26] Robert A Taylor, Patrick E Phelan, Todd P Ottanicar, Ronald Adrian, and Ravi Prasher. "Nanofluid optical property characterization: towards efficient direct absorption solar collectors". In: *Nanoscale Research Letters* 6 (2011), p. 225.

[27] Edda T. Ulset, Pawel Kosinski, Yulia Zabednova, Oleg V. Zhdaneev, Pavel G. Struchalin, and Boris V. Balakin. "Photothermal boiling in aqueous nanofluids". In: *Nano Energy* 50 (2018), pp. 339–346.

[28] Ziba Valizadeh and Mehrzad Shams. "Numerical investigation of water-based nanofluid subcooled flow boiling by three-phase Euler-Euler, Euler-Lagrange approach". In: *Heat Mass Transfer* 52 (2015), pp. 1501–1514.

[29] W. Wagner and A. Pruß. "The IAPWS Formulation 1995 for the Thermodynamic Properties of Ordinary Water Substance for General and Scientific Use". In: *Journal of Physical and Chemical Reference Data* 31.2 (2002), pp. 387–535. DOI: 10.1063/1.1461829.

[30] Zhao-Qin Yin, Xian-Feng Li, Fu-Bing Bao, Cheng-Xu Tu, and Xiao.Yan Gao. "Thermophoresis and Brownian Motion Effects on Nanoparticle Deposition Inside a 90 degree Square Bend Tube". In: *Aerosol and Air Quality Research* 18 (2018), pp. 1746–1755.